Reconstruction of the Stand-Level Disturbance History of a Temperate Coniferous Forest using LiDAR data and Geographic Object-Based Image Analysis (GEOBIA)

A Dissertation
Presented in Partial Fulfillment of the Requirements for the
Degree of Doctor of Philosophy
with a
Major in Natural Resources
in the
College of Graduate Studies
University of Idaho
by

Nuria Sánchez López

Major Professor: Luigi Boschetti, Ph.D.
Committee Members: Andrew T. Hudak, Ph.D.; Tara Hudiburg, Ph.D.; Alistair M.S. Smith, Ph.D.
Department Administrator: Lee Vierling, Ph.D.

August 2019

Authorization to Submit Dissertation

This dissertation of Nuria Sánchez López, submitted for the degree of Doctor of Philosophy with a Major in Natural Resources and titled "Reconstruction of the Stand-Level Disturbance History of a Temperate Coniferous Forest using LiDAR data and Geographic Object-Based Image Analysis (GEOBIA)," has been reviewed in final form. Permission, as indicated by the signatures and dates below, is now granted to submit final copies to the College of Graduate Studies for approval.

Major Professor: _____ Date: _____
Luigi Boschetti, Ph.D.

Committee Members: _____ Date: _____
Andrew T. Hudak, Ph.D.

_____ Date: _____
Tara Hudiburg, Ph.D.

_____ Date: _____
Alistair M.S. Smith, Ph.D.

Department Administrator: _____ Date: _____
Lee Vierling, Ph.D.

Abstract

Spatially explicit information on forest stand disturbance history is fundamental to understanding the global carbon cycle and enhancing the modelling of forest ecosystem processes. Forest disturbance records, defined in terms of Time Since Disturbance (TSD), are often incomplete for most forested areas, rarely extending before the Earth Observation satellite record. Although the spectral response of forest vegetation saturates under canopy closure, distinct horizontal and vertical forest structure features remain on the landscape for decades to centuries following a disturbance event. A stand-replacing disturbance is a mortality event (e.g., clearcut, fire, insect outbreak) that, in a short period of time, leads to complete replacement of the trees of an entire forest stand. Past stand-replacing disturbances thus result in even-aged stands, featuring only small age differences in their dominant cohort. They generally have homogenous forest canopies whose current structural development relates to TSD, as well as to the type of disturbance. In the several decades following a stand replacing disturbance, before maturity of the stand is reached and the age distribution becomes uneven, there is a strong linkage between forest structure and stand age which provides a pathway to characterize TSD from remotely sensed data.

This dissertation, divided in three chapters, proposes a novel approach to reconstruct the long-term disturbance history of a temperate coniferous forest from active remotely sensed data, that can potentially complement the more established methods based on time series analysis of passive optical remotely sensed data. The methodology uses Geographic Object-Based Image Analysis (GEOBIA) and remotely sensed data from LiDAR (Light Detection and Ranging) instruments to estimate the stand level TSD. GEOBIA enables the delineation of structurally homogenous forest stands, which are used as representative units of analysis; and LiDAR data, sensitive to the three-dimensional structure of the forest canopy, are used to estimate TSD. The study area is in the Nez-Perce Clearwater National Forest (Idaho, USA), where TSD reference maps for a period of more than 140 years, and airborne LiDAR data are available.

Chapter 1 proposes a two-stage evaluation strategy to semi-automatically delineate even-aged forest stands using GEOBIA on airborne LiDAR-derived data. GEOBIA has replaced traditional visual photo interpretation for forest stand delineation, but user-defined evaluation protocols are still required to identify objectively optimal delineation outputs. The study demonstrates the ability of LiDAR to discriminate stands harvested more than 50 years ago and proposes an objective and straightforward workflow that can be adapted to other study needs.

In chapter 2, airborne LiDAR canopy and topographic metrics are used to estimate TSD at the stand-level using Random Forest (RF) analysis. Results demonstrate that airborne LiDAR data have

enough explanatory power to categorize disturbance patterns through time. These data can be used to map disturbances that pre-date the beginning of the Earth Observation data record (up to 100 years). The integration of stand perimeters (derived from the workflow proposed in chapter 1) provides contextual information that reduces the amount of reference data required to train the RF and reduces the inherent variability of traditional cell-based analyses.

Chapter 3 presents a feasibility study for the estimation of TSD from data acquired by the newly launched spaceborne LiDAR Global Ecosystem Dynamics Investigation (GEDI) instrument. GEDI is a sampling instrument, acquiring footprints of approximately 22 m diameter, each separated by ~600 m across-track and ~60 m along-track. While GEDI will soon provide billions of forest canopy measurements for tropical and temperate forests around the globe, opening a new era in the use of LiDAR for forest mapping at large spatial scales, the sampling configuration imposes some challenges for continuous spatial analysis compared to the common discrete-return airborne LiDAR. The proposed approach overcomes these challenges through data fusion between optical (Landsat) and GEDI data. The approach is tested on the same study area of chapters 1 and 2, with simulated GEDI data generated from airborne LiDAR data. Landsat data are used to generate a wall-to-wall segmentation of the study area, identifying image-objects related to forest stands, and the GEDI footprints are used to generate single point estimates of TSD. The point estimates are subsequently upscaled at the Landsat image-object scale, resulting in a wall-to-wall TSD map of the study area. The results show the potential of GEDI data for TSD estimation on even-aged forests, particularly on disturbed stands within the last 100 years.

Acknowledgements

I would like to thank my major advisor, Dr. Luigi Boschetti, for the support of my study and research, his patience, insightful comments and guidance; to Dr. Andrew Hudak for his helpful comments, encouragement, and help during the past four years; and to the rest of my committee members, Dr. Tara Hudiburg and Dr. Alistair Smith, for their advice and support.

I would like to thank my friends and fellow graduate students for their feedback, cooperation and patience. The completion of this dissertation would not have been possible without their encouragement.

¡Gracias!

Table of Contents

Authorization to Submit Dissertation ii

Abstract iii

Acknowledgements v

Table of Contents vi

List of Tables viii

List of Figures xi

Statement of Contribution xvii

Introduction 1

References 5

Chapter 1: Semi-automated delineation of stands in an even-age dominated forest: a LiDAR-GEOBIA two-stage evaluation strategy. 12

Abstract 12

Introduction 12

Materials 15

Methods 17

Results 24

Discussion 26

Conclusions 28

Acknowledgements 29

References 29

Chapter 2: Reconstruction of the disturbance history of a temperate coniferous forest through stand-level analysis of airborne LiDAR data. 52

Abstract 52

Introduction 52

Materials 55

Methods 58
Results 63
Discussion 65
Conclusions 67
Acknowledgements 68
References 68
Chapter 3: Estimating Time Since the last stand-replacing Disturbance (TSD) from spaceborne GEDI data: a feasibility study. 94
Abstract 94
Introduction 94
Materials 97
Methods 99
Results 103
Discussion and Conclusions 105
Acknowledgements 107
References 108
Conclusion 130
References 132

List of Tables

Table 1.1. Light Detection and Ranging (LiDAR) summary metrics gridded at 30 m resolution from LiDAR point clouds. Twenty-five metrics are related to vegetation canopy height, and eleven are related to canopy density. 36

Table 1.2. LiDAR metrics considered in the analysis. The 'H95′ and 'Stratum above 30 m' metrics were selected based on literature review. From the remaining 34 metrics, the five metrics with absolute average value of the Pearson's correlation coefficient of the two LiDAR datasets (i.e., Clear Creek and Selway) lower than 0.5 (i.e., $|R| < 0.5$) with both 'H95′ and 'Stratum above 30 m' were selected..... 37

Table 1.3. Optimal segmentation of the seven considered LiDAR metrics. For each metric, the optimal set of multiresolution segmentation (MRS) algorithm parameters (scale, shape, compactness), the number of resulting image objects, and the unsupervised measures of spatial autocorrelation (normalized Moran's I, normalized weighted Variance, modified Global score) are presented. The two LiDAR datasets were processed independently. 38

Table 1.4. Supervised selection of the optimal LiDAR metric. Area-based dissimilarity metrics of oversegmentation (OS), undersegmentation (US), and summary score (D) are presented for the optimal segmentation of the seven considered LiDAR metrics; the number of reference objects with no corresponding image objects is also reported (Nnull). Four scenarios, based on the age of clearcut of the Forest Service Activity Track System (FACTs) harvest reference polygons, are considered: All clearcuts (1956–1996), clearcuts performed before the start of the Landsat MSS record (1956–1972), clearcuts performed before the start of the Landsat TM record (1956–1984), and clearcuts performed after the start of the Landsat TM/ETM+ record (1984–1996). For each scenario, the D score value of the optimal metric is marked (bold and underlined)..... 39

Table 1.5. Area-based dissimilarity metrics calculated from the validation dataset presented in Figure 1.10: Oversegmentation (OS), undersegmentation (US), summary score (D), modified oversegmentation ($OS*$), modified undersegmentation ($US*$), and summary score ($D*$)..... 40

Table 2.1. LiDAR acquisition parameters. 77

Table 2.2. LiDAR-derived summary metrics related to canopy structure (height & complexity, and density) and topography, computed as predictor variables for TSD modelling. All metrics are defined in 30m x 30m raster cells. On the equations, α is the topographic aspect in radians. 78

Table 2.3. Disturbed area reported on the ancillary reference dataset (Figure 2.1) and on the selected forest stands with known TSD (Figure 2.4) summarized by decade. Area is reported in number of disturbed hectares, and in percentage relative to the extent of the entire study area (52,257 ha). ND: forest stands non-disturbed since 1870..... 79

Table 2.4. Number and percentage of stands with known TSD within the study area summarized by decade; and number and percentage of sampled forest stands following the LiDAR-assisted stratification strategy (Figure 2.6). ND: forest stands non-disturbed since 1870. 80

Table 2.5. Confusion matrix of the TSD stand-level estimates of the 725 forest stands with known TSD not used to train the RF (Table 2.4) summarized by decade. ND: forest stands non-disturbed since 1870. 81

Table 2.6. Percentage and number (in brackets) of times that a predictor variable included in uncorrelated variable combinations ranked 1st, 2nd, or 3rd in order of importance based on the Mean Decrease in Gini (MDG) index of the RF. Pearson correlation threshold |R| = 0.5 for uncorrelated variable combination. 82

Table 2.7. Relative predictor variable importance summarized by group of metrics (Table 2.2), showing the percentage (and number) of uncorrelated variable combinations (out 210) that a variable from a group ranked 1st, 2nd, or 3rd (rank one is the most important) according to the Mean Decrease in Gini (MDG) index of the RF. 83

Table 3.1. Fifty-seven summary metrics calculated from the simulated GEDI waveforms (Hancock et al., 2019). 115

Table 3.2. Disturbed area reported on the ancillary reference dataset (Figure 3.2) and on the selected image objects of known TSD summarized by decade. The image objects overlapped 75% of their area with the ancillary reference dataset and enclosed at least one GEDI footprint. The area is reported in number of disturbed hectares, and in percentage relative to the extent of the entire study area. ND: forest stands non-disturbed since 1870..... 116

Table 3.3. Number of image objects sampled following the stratification strategy for one of the instances that extracted five image objects per stratum (Figure 3.4) summarized by decade; and number of GEDI footprints enclosed within their perimeters. ND: forest stands non-disturbed since 1870. . 117

Table 3.4. Confusion matrix of the TSD estimates of the 674 image objects of known TSD not used to train the RF summarized by decade. ND: forest stands non-disturbed since 1870. 118

List of Figures

Figure 1.1. Location of the study area in the Nez-Perce & Clearwater National Forest (Idaho-USA); boundaries of the 2009 and 2012 Light Detection and Ranging (LiDAR) acquisitions; and reference polygons of historical stand clearcuts (>2 ha) from the Forest Service Activity Track System (FACTs) harvest dataset. The FACTs polygons are displayed with a rainbow color scale indicating the year of harvest, from 1956 to 1996. No data are available for clearcuts performed before 1956; no clearcuts (>2 ha) were reported from 1996 to the LiDAR acquisition dates. On the bottom right, a 4 × 4 km subset of the Clear Creek watershed. 41

Figure 1.2. Example of pre-processing of the FACTs harvest polygons. Adjacent polygons harvested within a time interval ≤5 years (left) are merged into aggregated polygons (right) that are used as reference objects in all the subsequent steps of the analysis. 42

Figure 1.3. The seven LiDAR metrics considered in the analysis (Table 1.2), displayed with a linear black to white grayscale color table (1% linear stretch), on a 4 × 4 km subset of the Clear Creek watershed (location on Figure 1.1). The FACTs harvest reference dataset is presented for comparison in the upper left, to highlight the different response of each metric to even-aged forest stands. 43

Figure 1.4. Flowchart of the proposed methodology for forest stand delineation based on a two-stage evaluation strategy. 44

Figure 1.5. Illustration of the area-based dissimilarity metrics (OSi, USi, Di), and of the modified metrics ($OSi*$, $USi*$, $Di*$). A reference object xi, (black vectors) is displayed together with its corresponding set of image objects (gray vectors): The top row shows an example where the reference object is oversegmented, but not undersegmented (i.e., it is closely matched by the union area $yj \in Yi * yj$); the bottom row shows an example where the reference object is both oversegmented, and undersegmented. The center column illustrates the traditional oversegmentation (OSi), undersegmentation (USi) and summary score Di for that single reference object, metrics that consider

each individual corresponding image object. The right column illustrates the modified $OSi*$, $USi*$, and $Di*$ metrics, that consider instead the union area of all corresponding image objects. The summary score *D* does not report a significant difference between the two classifications (top: Di= 0.59, bottom: Di= 0.61), whereas the modified summary score *D** indicates that through post-processing the top row segmentation could result in a near-perfect match with the reference object ($Di*$= 0.04), whereas significant errors will remain in the bottom row segmentation ($Di*$= 0.29). 45

Figure 1.6. Segmentations of the 'H95′ LiDAR metric generated by the multiresolution segmentation (MRS) algorithm with different combinations of the scale and shape parameters, and the same compactness parameter (Comp. = 0.1). In all cases, the segmentation is displayed as orange vectors overlaid on the 'H95′ metric raster, shown in grayscale. The same 4 × 4 km area of Figure 1.1 is presented. 46

Figure 1.7. Scatter-plot of the normalized weighted variance ($wVarnorm$) and normalized Moran's Index ($MInorm$) of the segmentations of the 'H95′ metric for the Clear Creek dataset, generated by different sets of the MRS algorithm parameters. The two metrics are combined in a quadratic Global Score ($GSmod$) and the segmentation with the lowest $GSmod$ is selected as the optimal segmentation. 47

Figure 1.8. Optimal segmentation of the seven considered LiDAR metrics, shown for the same 4 × 4 km subset of Figure 1.1. The FACTS harvest reference dataset is shown at the upper left for comparison. 48

Figure 1.9. Optimal segmentation of the optimal 'H95′ metric (orange vector, overlaid on the 'H95′ shown in grayscale). Visual comparison with the FACTs dataset (Figure 1.2) indicates a good correspondence between even-aged forest stands and image objects. 49

Figure 1.10. Validation dataset: Reference objects delineated through visual interpretation of NAIP imagery and LiDAR point clouds (left); and corresponding image objects of the optimal segmentation

of the ‘H95′ LiDAR metric (right). Even-aged forest stand (EAF) reference objects and their corresponding image objects are shown in green, and uneven-aged forest stand (UAF) reference objects and their corresponding image objects are shown in gray. A total of 100 reference objects were generated through visual interpretation of NAIP imagery and LiDAR point clouds: 25 EAF (average area: ~23 ha) and 25 UAF (average area: ~158 ha) on each LiDAR dataset. 50

Figure 1.11. Illustrative examples of the spatial relationship between visually interpreted reference objects and corresponding image objects of the optimal segmentation of the ‘H95′ LiDAR metric. The two top rows present examples of uneven-aged forest stands (UAF), and the two bottom rows present examples of even-aged forest stands (EAF). Left column: Reference objects (red polygons) and set of the corresponding image objects (gray polygons). Center column: Reference objects overlaid on the ‘H95′ LiDAR metric shown in grayscale. Right column: Reference object and all image objects (orange polygons) overlaid on 1 m spatial resolution NAIP imagery used to generate the validation dataset, shown in true color. 51

Figure 2.1. Location of the study area in the Nez Perce-Clearwater National Forest (Idaho, USA); boundaries of the 2009 and 2012 LiDAR acquisitions; ancillary reference dataset of stand-replacing disturbances compiled from historic burns digitized from aerial photos (Morgan et al., 2017), and the perimeters of the stand and patch clearcut management units reported in the Forest Service Activity Track System (FACTs) harvest dataset (USDA, Forest Service, 2016). The color scale indicates the disturbance year (ranging between 2005 and 1870) and Time Since Disturbance (TSD, in parentheses), calculated with reference to 2012, i.e. the year of the more recent LiDAR data acquisition. 84

Figure 2.2. Forest stand map (orange vector) overlaid on the ‘H95’ LiDAR summary metric shown in grayscale. Top-right, histogram showing the percentage distribution of the size of the stands. 85

Figure 2.3. Pre-processing of the FACTs harvest management units (top row) and selection of forest stands with known TSD (bottom row). The top row shows an example of adjacent polygons harvested within a time interval ≤5 years (left) that are merged into aggregated polygons (right) that are used as

ancillary reference polygons. Bottom row shows the corresponding forest stand with known TSD selected from the forest stand map (Figure 2.2) according to the 50% overlap area criterion. The 'H95' LiDAR summary metric is shown in grayscale in the bottom left figure..... 86

Figure 2.4. Forest stands with known TSD. Colour ramp indicates the disturbance year (ranging between 2005 and 1870) and Time Since Disturbance (TSD). Top-right, histogram showing the percentage distribution of the overlapping area (in %) between the forest stands with known TSD and the ancillary reference dataset (Figure 2.1). 87

Figure 2.5. Workflow of the proposed methodology to generate a map of estimated Time Since the last stand-replacing Disturbance (TSD) at the forest stand-level..... 88

Figure 2.6. Scheme of the LiDAR-assisted stratification of the forest stands with known TSD. The mean topographic solar-radiation aspect index ('SRAI') and the mean 95th percentile of height above 1.37 m ('H95') are used as stratification variables. The 56 stands used as training dataset are reported as red triangles..... 89

Figure 2.7. TSD imputations at the cell level using RF analysis and 21 LiDAR predictor variables related to canopy structure and topography (Table 2.2). 90

Figure 2.8. Stand-replacing disturbance history map. TSD stand-level calculated as the median value of the imputed TSD (Figure 2.7) cell estimates enclosed within the perimeters of the forest stands (Figure 2.2). 91

Figure 2.9. Partial dependence plots with probability distribution of TSD for the four variables with the highest importance (Table 2.6). Each curve represents the conditional TSD probability as a function of the LiDAR metrics (TSD is aggregated in 10-year bins). 92

Figure 2.10. Boxplots of RMSD, BIAS, and Perct.10 obtained for TSD predictions when 1 to 10 forest stands were selected per stratum (Figure 2.6). The random selection of forest stands was replicated 10 times. Central line represents the median, edges of the box are the first (i.e., the 25th percentile) and the

third (i.e., 75th percentile) quartiles, and the whiskers are 1.5 times the range of the upper and lower quartiles. 93

Figure 3.1. Study area in the Nez-Perce & Clearwater National Forest (Idaho-USA), and distribution of the simulated GEDI footprints (not drawn to scale for visualization). 119

Figure 3.2. Historical stand-replacing disturbances reported in the study area between 1870 and 2005. The dataset was compiled from records of historical burns digitized from aerial photographs (Morgan et al., 2017), and digitized perimeters of clearcut management units reported in the FACTs (Forest Service Activity Track System) harvest dataset (USDA, Forest Service, 2016). Twenty additional forest stands non-disturbed since 1870 were delineated through visual photo-interpretation and added to the dataset. 120

Figure 3.3. Flowchart of the proposed methodology. 121

Figure 3.4. Scheme of the stratified random sampling to extract training image objects of known TSD. The mean topographic solar-radiation aspect index ('SRAI') and the mean GEDI 98% relative of height (from inflection points) ('rhInfl98') were used as stratification variables. In this example, 50 image objects (reported as red triangles) are sampled. 122

Figure 3.5. Optimal Landsat segmentation (grey vector) of the Tasseled Cap indices of Brightness (TCB), Greenness (TCG) and Wetness (TCW), that are displayed as background in an RGB combination (R= TCW, G= TCG, B= TCB). 123

Figure 3.6. Percentage of image objects of the Landsat segmentation (Figure 3.5) that enclosed, at least, the number of GEDI footprints specified on the x axis; and percentage of the study area that they represent. 124

Figure 3.7. Boxplots of RMSD, BIAS, and Perct.10 obtained for TSD predictions when 1 to 10 image objects are selected per stratum (Figure 3.4) to train the RF. The random selection of image objects was replicated 100 times per sample size. Central line represents the median, edges of the box are the first

(i.e., the 25th percentile) and the third (i.e., 75th percentile) quartiles, and the whiskers are 1.5 times the range of the upper and lower quartiles. 125

Figure 3.8. Illustrative example of the TSD predictions at the GEDI footprint level (~22 m diameter) and the resulting estimates at the image object level..... 126

Figure 3.9. TSD predictions at the image object level. 127

Figure 3.10. Boxplots of the number of validation objects, RMSD, BIAS, and Perct.10 for TSD predictions according to disturbance decade (as observed in the ancillary reference dataset). The boxplots display the results of the 100 imputations obtained by sampling five image objects per stratum to train the RF (Figure 3.4). Central line represents the median, edges of the box are the first (i.e., the 25th percentile) and the third (i.e., 75th percentile) quartiles, and the whiskers are 1.5 times the range of the upper and lower quartiles 128

Figure 3.11. Boxplots of number of validation objects, RMSD, BIAS, and Perct.10 obtained for TSD predictions of the validation image objects matching from 1 to 10 GEDI footprints. The boxplots display the results of the 100 imputations obtained by sampling five image objects per stratum to train the RF (Figure 3.4). Central line represents the median, edges of the box are the first (i.e., the 25th percentile) and the third (i.e., 75th percentile) quartiles, and the whiskers are 1.5 times the range of the upper and lower quartiles. 129

Statement of Contribution

Chapter 1: Published in *Remote Sensing* as:

Sanchez-Lopez, N., Boschetti, L. and Hudak, A., 2018. Semi-Automated Delineation of Stands in an Even-Age Dominated Forest: A LiDAR-GEOBIA Two-Stage Evaluation Strategy. Remote Sensing, 10(10), p.1622.

N.S-L., L.B. and A.H. conceived the overall approach of the paper. N.S-L. refined the methods, performed the analysis, structured and wrote the paper with assistance from L.B. A.H. provided technical assistance, and comments while drafting and finalizing the manuscript.

Chapter 2: Under review in *Forestry An international journal of forest research*:

N.S-L., L.B. and A.H. conceived the overall approach of the paper. N.S-L. performed the analysis, processed the data, structured and wrote the paper with assistance from L.B. A.H. provided feedback and comments while drafting and finalizing the manuscript.

Introduction

Forest disturbances shift forest age, altering the global carbon balance of the Earth. Forest regrowth, relating to both forest age and the Time Since the last Disturbance (TSD), is one of the main drivers of the terrestrial carbon sink that removes ~3 billion tons of anthropogenic CO_2 each year (Canadell et al., 2007; Canadell and Raupach, 2008). Since carbon stocks and fluxes of old forests (>100 years) remain mostly constant (Bradford et al., 2008), spatially explicit information on the TSD of young and mature forests is critical to understanding the historic, current, and potential of forest carbon sequestration.

Forest disturbances shape the forest landscape, altering forest structure, function, and composition (Dale et al., 2011; Franklin et al., 2002). Following a disturbance, especially after a stand-replacing disturbance, forest stand development at specific geographic locations follows a predictable pattern, as distinct species compositions, and structural changes through time appear (Oliver, 1980; Oliver and Larson, 1996). The stand is a continuous community of trees uniform enough in class distribution, composition, and structure that also grows on a site of sufficiently uniform quality to be distinguishable from adjacent units (Helms, 1998). Stands recovering from past stand-replacing disturbances (i.e., even-aged stands) feature only small age differences in their dominant cohort. They tend to have homogenous forest canopies, which current development relates to the type of disturbance and TSD. A stand-replacing (major) disturbance is a mortality event (e.g., clearcut, fire, insect outbreak) that in a short period of time leads to complete replacement of the trees of an entire forest stand. Following a stand-replacing disturbance, regeneration is characterized by competition between a cohort of new trees (Oliver, 1980; Oliver and Larson, 1996). Examples of stand-replacing disturbances include those caused by anthropogenic agents, such as clearcuts, and natural agents, such as crown fires and high severity outbreaks. Wildfires and clearcuts are both major disturbance agents, and in Canada and the United States alone, they affect more than 50,000 km^2 each year (Masek et al., 2013; White et al., 2017). In such areas under a high disturbance pressure, the result is a landscape dominated by a patchy and heterogeneous mosaic of stands. These stands feature small age differences and structural differences in their dominant cohort, and have large differences between neighboring stands under different successional stages.

Current techniques to map forest stand-replacing disturbances and stand age are based on field inventory and/or remote sensing datasets. Stand age in regenerated forests can be assessed, for instance, using inventory records of management activities (if available) and photo interpretation of forest stands with high-resolution imagery (Anttila, 2002); inferred from inventory data (e.g., using height-age, volume-age, biomass-age curves) (He et al., 2012; Poorter et al., 2016); or from tree cores of

representative trees (Speer, 2010). Data records of harvests and plantations are rare, and, where available, their use is extremely undependable for continuous spatial analysis at relatively large scales. Moreover, while dendrochronological analyses of tree rings and inventory data are suitable for estimating stand age and identifying past disturbances, they are time-consuming, expensive, and spatially constrained to sampled locations (Racine et al., 2014; Speer, 2010). Earth observation satellite data, on the other hand, have the spatial and temporal properties needed to track recent disturbances in a systematic way at a variety of spatial scales. This is done through change detection and temporal segmentation analysis, that automate the temporal comparison of image time series (Kennedy et al., 2010). These approaches, often performed on widely available multispectral and moderate resolution data, such as those provided by Landsat, have shown notable results in the detection of recent disturbances. However, there are limitations (a) in the extension of the analysis to the past, before the start of the Earth Observation (EO) satellite record and (b) in the aggregation of pixel-level detections into stand-level results.

Early approaches to mapping disturbances using optical remotely sensed data relied on the comparison of a pre- and post-change image to detect abrupt changes in the land cover, which progressively evolved into multiple two-date comparisons in sequences (Cohen et al., 2002; Lu et al., 2004). More recently, improvements in computing power and availability of data, thanks to the opening of the Landsat archive in 2008 (Woodcock et al., 2008), have resulted in the onset of new approaches. These recent methods automate the analysis of historical image time series to detect discontinuities on the land cover caused by abrupt disturbances; and to detect changes in trends caused by slower change processes (Kennedy et al., 2010). Thus, the multi-temporal change detection field provides a wide range of methodologies and applications that can be applied to a variety of situations. However, these methods can only track disturbances that have happened since the beginning of the EO data record, which began in 1972 when Landsat-1 was placed in orbit. In theory, this would guarantee the availability of moderate-resolution global disturbance datasets of almost 50 years, but in practice, the EO repository is incomplete in most areas outside the U.S. before the launch of Landsat-7 in 1999. Before that, Landsat data were downlinked to specific international ground stations without duplication in the main archive of the U.S. Geological Survey, and many of these scenes were irrecoverable (Wulder et al., 2016). On the other hand, single image analyses and predictive modelling strategies using optical data have little potential to temporally complement TSD datasets obtained from time series analysis. These methods prove inadequate for two main reasons: first, because the spectral response of vegetation in optical wavelengths saturates in closed canopy forests (Spanner et al., 1990; Turner et al., 1999), and second, because the persistence of disturbance spectral signatures on the landscape is short (Healey et al., 2005; Lunetta et al., 2004).

However, the structure of mature and young stands remains distinct until the uneven-aged distribution of the forest canopy is reached, which might take 80+ years depending on the forest type. Active remotely sensed systems, specifically Light Detection and Ranging (LiDAR), have emerged in recent decades as one of the most powerful remote sensing methods to describe the structure of the forest canopy (Goetz and Dubayah, 2011). Dominated by airborne platforms, LiDAR systems acquire direct measurements of the canopy at high resolution, which is optimal to characterize forest attributes such as height, basal area, density, biomass, or leaf area index (LAI) (Andersen et al., 2005; Boudreau et al., 2008; Coops et al., 2007; Hudak et al., 2006; Lefsky et al., 1999; Naesset, 1997; Nelson et al., 1988; Zhao and Popescu, 2009). Recent studies have also shown a strong relationship between LiDAR-derived data and stand age (Racine et al., 2014; Zhang et al., 2014), and therefore, LiDAR may also be optimal for deriving outputs that complement stand-replacing disturbance datasets, expanding its temporal contextualization beyond the beginning of the EO satellite record.

On the second limitation, traditional remote sensing approaches for mapping disturbances have conventionally relied on the pixel as the basic and independent spatial unit of analysis. The pixel by itself doesn't represent a true geographical feature (Fisher, 1997), and its use as an independent mapping unit to characterize stand-replacing disturbances often results in noisy outputs caused by frequent commission and omission classification errors (Radke et al., 2005). While pixel-based techniques are computationally faster, they neglect the spatial relationship that pixels belonging to the same feature share (Blaschke et al., 2014). Geographic-Object Based Image Analysis (GEOBIA) techniques, alternatively, attempt to mimic the way humans interpret images by identifying the image object, instead of the pixel, as the basic spatial unit of analysis. The image object is a discrete region composed by a group of pixels that is internally coherent and different from the surroundings, and ideally, the image object represents a true geographic feature on the landscape (e.g., a tree or a forest stand). The linkage between the image object and the geographic feature of interest is the ultimate goal of GEOBIA, and it is achieved semi-automatically through a workflow that incorporates both image segmentation and classification procedures (Blaschke et al., 2014, 2008).

GEOBIA's ability to enhance stand-level research is demonstrated by recent studies designed to characterize forest stands (Chen et al., 2011; Hay and Castilla, 2008; Kim et al., 2009; Mallinis et al., 2008), to classify forest type and species (Förster and Kleinschmit, 2008; Ke et al., 2010), or to obtain forest inventory parameters (Chubey et al., 2006). GEOBIA strategies to delineate forest stands are often focused on stand definitions based on species composition rather than structure; they are sometimes local (over study areas smaller than 1000 ha); or they lack evaluation protocols (e.g., Dechesne et al., 2017; Koch et al., 2009; Leppänen et al., 2008; Sullivan et al., 2009; Tiede et al., 2004;

Varo-Martínez et al., 2017; Wu et al., 2014; Wulder et al., 2008). The semi-automatic delineation of forest stands is not a standardized and straightforward technique, requiring a user-defined evaluation to identify, inter alia the adequate input data, segmentation algorithm, and algorithm parameters (Costa et al., 2018). It is required, therefore, to establish and develop objective object-based approaches specifically designed to delineate and categorize forest stands under different ecological and management considerations. Such protocols could be easily replicated on other study sites. In this sense, a quantitative assessment of the performance of LiDAR-derived data to delineate stands in even-aged dominated forest is still required.

Airborne LiDAR has the potential to complement current datasets of stand-replacing disturbances, being optimal for both image segmentation and TSD characterization. However, the deployment of airborne LiDAR for systematic monitoring of forest stand attributes doesn´t enable analyses at large spatial scales due to restrictions of data availability and high cost compared to satellite remote sensing instruments. A recent spaceborne LiDAR mission, the Global Ecosystem Dynamics Investigation (GEDI), has been designed to monitoring the forest structure of temperate and tropical forests (Dubayah et al., 2014). The GEDI instrument, a waveform large-footprint LiDAR, was successfully deployed in the International Space Station (ISS) in December 2018. Over its two-year programmed mission, it will record billions of waveform observations between 51.6° N to 51.6° S latitudes, from which ground elevation, canopy height, foliage profiles, density, and above-ground biomass datasets will be derived (Dubayah et al., 2014; Hancock et al., 2019; Stysley et al., 2015). These data products will offer higher resolution and accuracy measuring the structural parameters of forests than what has been possible with optical satellite data (Hancock et al., 2019). However, GEDI is a sampling instrument: it is composed of three laser transmitters that produce eight parallel ground tracks. GEDI acquires waveform data on footprints of approximately 22 m diameter that are separated about 600 m across each track, an about 60 m along each track (Qi et al., 2019). This sampling configuration makes it necessary to design methodologies that extend the discrete measurements collected at the footprint level across larger spatial scales to wall-to-wall mapping forest attributes such as TSD. A promising approach would consist on upscaling the GEDI spaceborne footprint observations to an image object that represents a forest patch (Lefsky, 2010; Montesano et al., 2013), for which data fusion strategies with data sources that have a complete horizontal coverage, as Landsat, should be prototyped. Landsat data have been used for image segmentation in studies related to the estimation of forest structural attributes such as biomass and TSD (Montesano et al., 2013; Wulder et al., 2004); and have an adequate resolution (30 m) for forest stand-level analysis. Therefore, the combination of GEDI data and Landsat data is promising to mapping TSD at the stand level. However, the feasibility of the

data fusion approach should be evaluated since it would depend on the combined effect of the GEDI sampling grid and the quality of the segmentation.

This research proposes a new approach for historical stand-replacing disturbance mapping, integrating both GEOBIA and LiDAR data. This novel methodology could eventually complement available data records of the disturbance history of forests by reducing the temporal and spatial limitations of current, conventionally used mapping techniques. The dissertation is divided into three main chapters that further develop the three main goals of the research: (1) to develop an objective, straightforward and reproducible workflow to delineate even-aged forest stands using image segmentation and object-based evaluation techniques on LiDAR data; (2) to assess the predictive power of LiDAR-derived data to estimate stand-level TSD at the long-term (~100 years); and (3) to assess the feasibility of using GEDI data to estimate stand-level TSD through a data fusion strategy that applies object-based analysis on Landsat data.

References

Andersen, H.-E., McGaughey, R.J., Reutebuch, S.E., 2005. Estimating forest canopy fuel parameters using LIDAR data. Remote Sens. Environ. 94, 441–449. https://doi.org/10.1016/j.rse.2004.10.013

Anttila, P., 2002. Updating stand level inventory data applying growth models and visual interpretation of aerial photographs. Silva Fenn. 36, 549–560.

Blaschke, T., Hay, G.J., Kelly, M., Lang, S., Hofmann, P., Addink, E., Queiroz Feitosa, R., van der Meer, F., van der Werff, H., van Coillie, F., Tiede, D., 2014. Geographic Object-Based Image Analysis – Towards a new paradigm. ISPRS J. Photogramm. Remote Sens. 87, 180–191. https://doi.org/10.1016/j.isprsjprs.2013.09.014

Blaschke, T., Lang, S., Hay, G., 2008. Object-Based Image Analysis: Spatial Concepts for Knowledge-Driven Remote Sensing Applications. Springer Science & Business Media.

Boudreau, J., Nelson, R.F., Margolis, H.A., Beaudoin, A., Guindon, L., Kimes, D.S., 2008. Regional aboveground forest biomass using airborne and spaceborne LiDAR in Québec. Remote Sens. Environ. 112, 3876–3890. https://doi.org/10.1016/j.rse.2008.06.003

Bradford, J.B., Birdsey, R.A., Joyce, L.A., Ryan, M.G., 2008. Tree age, disturbance history, and carbon stocks and fluxes in subalpine Rocky Mountain forests. Glob. Change Biol. 14, 2882–2897. https://doi.org/10.1111/j.1365-2486.2008.01686.x

Canadell, J.G., Quéré, C.L., Raupach, M.R., Field, C.B., Buitenhuis, E.T., Ciais, P., Conway, T.J., Gillett, N.P., Houghton, R.A., Marland, G., 2007. Contributions to accelerating atmospheric CO2 growth from economic activity, carbon intensity, and efficiency of natural sinks. Proc. Natl. Acad. Sci. 104, 18866–18870. https://doi.org/10.1073/pnas.0702737104

Canadell, J.G., Raupach, M.R., 2008. Managing Forests for Climate Change Mitigation. Science 320, 1456–1457. https://doi.org/10.1126/science.1155458

Chen, G., Hay, G.J., Castilla, G., St-Onge, B., Powers, R., 2011. A multiscale geographic object-based image analysis to estimate lidar-measured forest canopy height using Quickbird imagery. Int. J. Geogr. Inf. Sci. 25, 877–893. https://doi.org/10.1080/13658816.2010.496729

Chubey, M.S., Franklin, S.E., Wulder, M.A., 2006. Object-based Analysis of Ikonos-2 Imagery for Extraction of Forest Inventory Parameters. Photogramm. Eng. Remote Sens. 72, 383–394. https://doi.org/10.14358/PERS.72.4.383

Cohen, W.B., Spies, T.A., Alig, R.J., Oetter, D.R., Maiersperger, T.K., Fiorella, M., 2002. Characterizing 23 years (1972–95) of stand replacement disturbance in western Oregon forests with Landsat imagery. Ecosystems 5, 122–137.

Coops, N.C., Hilker, T., Wulder, M.A., St-Onge, B., Newnham, G., Siggins, A., Trofymow, J.A. (Tony), 2007. Estimating canopy structure of Douglas-fir forest stands from discrete-return LiDAR. Trees 21, 295–310. https://doi.org/10.1007/s00468-006-0119-6

Costa, H., Foody, G.M., Boyd, D.S., 2018. Supervised methods of image segmentation accuracy assessment in land cover mapping. Remote Sens. Environ. 205, 338–351. https://doi.org/10.1016/j.rse.2017.11.024

Dale, V.H., Efroymson, R.A., Kline, K.L., 2011. The land use–climate change–energy nexus. Landsc. Ecol. 26, 755–773. https://doi.org/10.1007/s10980-011-9606-2

Dechesne, C., Mallet, C., Le Bris, A., Gouet-Brunet, V., 2017. Semantic segmentation of forest stands of pure species combining airborne lidar data and very high resolution multispectral imagery. ISPRS J. Photogramm. Remote Sens. 126, 129–145. https://doi.org/10.1016/j.isprsjprs.2017.02.011

Dubayah, R., Goetz, S.J., Blair, J.B., Fatoyinbo, T.E., Hansen, M., Healey, S.P., Hofton, M.A., Hurtt, G.C., Kellner, J., Luthcke, S.B., Swatantran, A., 2014. The Global Ecosystem Dynamics Investigation. AGU Fall Meet. Abstr. 14.

Fisher, P., 1997. The pixel: A snare and a delusion. Int. J. Remote Sens. 18, 679–685. https://doi.org/10.1080/014311697219015

Förster, M., Kleinschmit, B., 2008. Object-based classification of QuickBird data using ancillary information for the detection of forest types and NATURA 2000 habitats, in: Blaschke, T., Lang, S., Hay, G.J. (Eds.), Object-Based Image Analysis, Lecture Notes in Geoinformation and Cartography. Springer Berlin Heidelberg, pp. 275–290. https://doi.org/10.1007/978-3-540-77058-9_15

Franklin, J.F., Spies, T.A., Pelt, R.V., Carey, A.B., Thornburgh, D.A., Berg, D.R., Lindenmayer, D.B., Harmon, M.E., Keeton, W.S., Shaw, D.C., Bible, K., Chen, J., 2002. Disturbances and structural development of natural forest ecosystems with silvicultural implications, using Douglas-fir forests as an example. For. Ecol. Manag., Forest Ecology in the next Millennium : Putting the long view into Practice 155, 399–423. https://doi.org/10.1016/S0378-1127(01)00575-8

Goetz, S., Dubayah, R., 2011. Advances in remote sensing technology and implications for measuring and monitoring forest carbon stocks and change. Carbon Manag. 2, 231–244. https://doi.org/10.4155/cmt.11.18

Hancock, S., Armston, J., Hofton, M., Sun, X., Tang, H., Duncanson, L.I., Kellner, J.R., Dubayah, R., 2019. The GEDI simulator: A large-footprint waveform lidar simulator for calibration and validation of spaceborne missions. Earth Space Sci. 0. https://doi.org/10.1029/2018EA000506

Hay, G. J., Castilla, G., 2008. Geographic Object-Based Image Analysis (GEOBIA): A new name for a new discipline, in: Blaschke, T., Lang, S., Hay, Geoffrey J. (Eds.), Object-Based Image Analysis, Lecture Notes in Geoinformation and Cartography. Springer Berlin Heidelberg, pp. 75–89. https://doi.org/10.1007/978-3-540-77058-9_4

He, L., Chen, J.M., Pan, Y., Birdsey, R., Kattge, J., 2012. Relationships between net primary productivity and forest stand age in US forests. Glob. Biogeochem. Cycles 26.

Healey, S.P., Cohen, W.B., Zhiqiang, Y., Krankina, O.N., 2005. Comparison of Tasseled Cap-based Landsat data structures for use in forest disturbance detection. Remote Sens. Environ. 97, 301–310. https://doi.org/10.1016/j.rse.2005.05.009

Helms, J., 1998. The Dictionary of Forestry. Western Heritage Co.

Hudak, A.T., Crookston, N.L., Evans, J.S., Falkowski, M.J., Smith, A.M., Gessler, P.E., Morgan, P., 2006. Regression modeling and mapping of coniferous forest basal area and tree density from discrete-return lidar and multispectral satellite data. Can. J. Remote Sens. 32, 126–138.

Ke, Y., Quackenbush, L.J., Im, J., 2010. Synergistic use of QuickBird multispectral imagery and LIDAR data for object-based forest species classification. Remote Sens. Environ. 114, 1141–1154. https://doi.org/10.1016/j.rse.2010.01.002

Kennedy, R.E., Yang, Z., Cohen, W.B., 2010. Detecting trends in forest disturbance and recovery using yearly Landsat time series: 1. LandTrendr — Temporal segmentation algorithms. Remote Sens. Environ. 114, 2897–2910. https://doi.org/10.1016/j.rse.2010.07.008

Kim, M., Madden, M., Warner, T.A., 2009. Forest Type Mapping using Object-specific Texture Measures from Multispectral Ikonos Imagery. Photogramm. Eng. Remote Sens. 75, 819–829. https://doi.org/10.14358/PERS.75.7.819

Koch, B., Straub, C., Dees, M., Wang, Y., Weinacker, H., 2009. Airborne laser data for stand delineation and information extraction. Int. J. Remote Sens. 30, 935–963.

Lefsky, M.A., 2010. A global forest canopy height map from the Moderate Resolution Imaging Spectroradiometer and the Geoscience Laser Altimeter System. Geophys. Res. Lett. 37. https://doi.org/10.1029/2010GL043622

Lefsky, M.A., Cohen, W.B., Acker, S.A., Parker, G.G., Spies, T.A., Harding, D., 1999. Lidar Remote Sensing of the Canopy Structure and Biophysical Properties of Douglas-Fir Western Hemlock Forests. Remote Sens. Environ. 70, 339–361. https://doi.org/10.1016/S0034-4257(99)00052-8

Leppänen, V.J., Tokola, T., Maltamo, M., Mehtätalo, L., Pusa, T., Mustonen, J., 2008. Automatic delineation of forest stands from LiDAR data, in: GEOBIA, 2008 – Pixels, Objects, Intelligence: GEOgraphic Object Based Image Analysis for the 21st Century. Presented at the GEOBIA, 2008 – Pixels, Objects, Intelligence: GEOgraphic Object Based Image Analysis for the 21st Century, University of Calgary, Calgary, Alberta, Canada., pp. 271–277.

Lu, D., Mausel, P., Brondízio, E., Moran, E., 2004. Change detection techniques. Int. J. Remote Sens. 25, 2365–2401.

Lunetta, R.S., Johnson, D.M., Lyon, J.G., Crotwell, J., 2004. Impacts of imagery temporal frequency on land-cover change detection monitoring. Remote Sens. Environ. 89, 444–454. https://doi.org/10.1016/j.rse.2003.10.022

Mallinis, G., Koutsias, N., Tsakiri-Strati, M., Karteris, M., 2008. Object-based classification using Quickbird imagery for delineating forest vegetation polygons in a Mediterranean test site. ISPRS J. Photogramm. Remote Sens. 63, 237–250. https://doi.org/10.1016/j.isprsjprs.2007.08.007

Masek, J.G., Goward, S.N., Kennedy, R.E., Cohen, W.B., Moisen, G.G., Schleeweis, K., Huang, C., 2013. United States Forest Disturbance Trends Observed Using Landsat Time Series. Ecosystems 16, 1087–1104. https://doi.org/10.1007/s10021-013-9669-9

Montesano, P.M., Cook, B.D., Sun, G., Simard, M., Nelson, R.F., Ranson, K.J., Zhang, Z., Luthcke, S., 2013. Achieving accuracy requirements for forest biomass mapping: A spaceborne data fusion method for estimating forest biomass and LiDAR sampling error. Remote Sens. Environ. 130, 153–170. https://doi.org/10.1016/j.rse.2012.11.016

Naesset, E., 1997. Determination of mean tree height of forest stands using airborne laser scanner data. ISPRS J. Photogramm. Remote Sens. 52, 49–56.

Nelson, R., Krabill, W., Tonelli, J., 1988. Estimating forest biomass and volume using airborne laser data. Remote Sens. Environ. 24, 247–267. https://doi.org/10.1016/0034-4257(88)90028-4

Oliver, C.D., 1980. Forest development in North America following major disturbances. For. Ecol. Manag. 3, 153–168.

Oliver, C.D., Larson, B.C., 1996. Forest stand dynamics: updated edition. John Wiley and sons.

Poorter, L., Bongers, F., Aide, T.M., Almeyda Zambrano, A.M., Balvanera, P., Becknell, J.M., Boukili, V., Brancalion, P.H.S., Broadbent, E.N., Chazdon, R.L., Craven, D., de Almeida-Cortez, J.S., Cabral, G.A.L., de Jong, B.H.J., Denslow, J.S., Dent, D.H., DeWalt, S.J., Dupuy, J.M., Durán, S.M., Espírito-Santo, M.M., Fandino, M.C., César, R.G., Hall, J.S., Hernandez-Stefanoni, J.L., Jakovac, C.C., Junqueira, A.B., Kennard, D., Letcher, S.G., Licona, J.-C., Lohbeck, M., Marín-Spiotta, E., Martínez-Ramos, M., Massoca, P., Meave, J.A., Mesquita, R., Mora, F., Muñoz, R., Muscarella, R., Nunes, Y.R.F., Ochoa-Gaona, S., de Oliveira, A.A., Orihuela-Belmonte, E., Peña-Claros, M., Pérez-García, E.A., Piotto, D., Powers, J.S., Rodríguez-Velázquez, J., Romero-Pérez, I.E., Ruíz, J., Saldarriaga, J.G., Sanchez-Azofeifa, A., Schwartz, N.B., Steininger, M.K., Swenson, N.G., Toledo, M., Uriarte, M., van Breugel, M., van der Wal, H., Veloso, M.D.M., Vester, H.F.M., Vicentini, A., Vieira, I.C.G., Bentos, T.V., Williamson, G.B., Rozendaal, D.M.A., 2016. Biomass resilience of Neotropical secondary forests. Nature 530, 211–214. https://doi.org/10.1038/nature16512

Qi, W., Lee, S.-K., Hancock, S., Luthcke, S., Tang, H., Armston, J., Dubayah, R., 2019. Improved forest height estimation by fusion of simulated GEDI Lidar data and TanDEM-X InSAR data. Remote Sens. Environ. 221, 621–634. https://doi.org/10.1016/j.rse.2018.11.035

Racine, E.B., Coops, N.C., St-Onge, B., Bégin, J., 2014. Estimating Forest Stand Age from LiDAR-Derived Predictors and Nearest Neighbor Imputation. For. Sci. 60, 128–136. https://doi.org/10.5849/forsci.12-088

Radke, R.J., Andra, S., Al-Kofahi, O., Roysam, B., 2005. Image change detection algorithms: a systematic survey. IEEE Trans. Image Process. 14, 294–307. https://doi.org/10.1109/TIP.2004.838698

Spanner, M.A., Pierce, L.L., Peterson, D.L., Running, S.W., 1990. Remote sensing of temperate coniferous forest leaf area index The influence of canopy closure, understory vegetation and background reflectance. Int. J. Remote Sens. 11, 95–111.

Speer, J.H., 2010. Fundamentals of Tree-ring Research. University of Arizona Press.

Stysley, P.R., Coyle, D.B., Kay, R.B., Frederickson, R., Poulios, D., Cory, K., Clarke, G., 2015. Long term performance of the High Output Maximum Efficiency Resonator (HOMER) laser for NASA′s Global Ecosystem Dynamics Investigation (GEDI) lidar. Opt. Laser Technol. 68, 67–72. https://doi.org/10.1016/j.optlastec.2014.11.001

Sullivan, A.A., McGaughey, R.J., Andersen, H.-E., Schiess, P., 2009. Object-oriented classification of forest structure from light detection and ranging data for stand mapping. West. J. Appl. For. 24, 198–204.

Tiede, D., Blaschke, T., Heurich, M., 2004. Object-based semi automatic mapping of forest stands with Laser scanner and Multi-spectral data. Int. Arch. Photogramm. Remote Sens. Spat. Inf. Sci. 36, 328–333.

Turner, D.P., Cohen, W.B., Kennedy, R.E., Fassnacht, K.S., Briggs, J.M., 1999. Relationships between Leaf Area Index and Landsat TM Spectral Vegetation Indices across Three Temperate Zone Sites. Remote Sens. Environ. 70, 52–68. https://doi.org/10.1016/S0034-4257(99)00057-7

Varo-Martínez, M.Á., Navarro-Cerrillo, R.M., Hernández-Clemente, R., Duque-Lazo, J., 2017. Semi-automated stand delineation in Mediterranean Pinus sylvestris plantations through segmentation of LiDAR data: The influence of pulse density. Int. J. Appl. Earth Obs. Geoinformation 56, 54–64. https://doi.org/10.1016/j.jag.2016.12.002

White, J.C., Wulder, M.A., Hermosilla, T., Coops, N.C., Hobart, G.W., 2017. A nationwide annual characterization of 25 years of forest disturbance and recovery for Canada using Landsat time series. Remote Sens. Environ. 194, 303–321. https://doi.org/10.1016/j.rse.2017.03.035

Woodcock, C.E., Allen, R., Anderson, M., Belward, A., Bindschadler, R., Cohen, W., Gao, F., Goward, S.N., Helder, D., Helmer, E., 2008. Free access to Landsat imagery. Science 320, 1011–1011.

Wu, Z., Heikkinen, V., Hauta-Kasari, M., Parkkinen, J., Tokola, T., 2014. ALS data based forest stand delineation with a coarse-to-fine segmentation approach. IEEE, pp. 547–552. https://doi.org/10.1109/CISP.2014.7003840

Wulder, M.A., Skakun, R.S., Kurz, W.A., White, J.C., 2004. Estimating time since forest harvest using segmented Landsat ETM+ imagery. Remote Sens. Environ. 93, 179–187. https://doi.org/10.1016/j.rse.2004.07.009

Wulder, M.A., White, J.C., Hay, G.J., Castilla, G., 2008. Towards automated segmentation of forest inventory polygons on high spatial resolution satellite imagery. For. Chron. 84, 221–230.

Wulder, M.A., White, J.C., Loveland, T.R., Woodcock, C.E., Belward, A.S., Cohen, W.B., Fosnight, E.A., Shaw, J., Masek, J.G., Roy, D.P., 2016. The global Landsat archive: Status, consolidation, and direction. Remote Sens. Environ., Landsat 8 Science Results 185, 271–283. https://doi.org/10.1016/j.rse.2015.11.032

Zhang, C., Ju, W., Chen, J.M., Li, D., Wang, X., Fan, W., Li, M., Zan, M., 2014. Mapping forest stand age in China using remotely sensed forest height and observation data. J. Geophys. Res. Biogeosciences 119, 1163–1179. https://doi.org/10.1002/2013JG002515

Zhao, K., Popescu, S., 2009. Lidar-based mapping of leaf area index and its use for validating GLOBCARBON satellite LAI product in a temperate forest of the southern USA. Remote Sens. Environ. 113, 1628–1645. https://doi.org/10.1016/j.rse.2009.03.006

Chapter 1: Semi-automated delineation of stands in an even-age dominated forest: a LiDAR-GEOBIA two-stage evaluation strategy.

Published in *Remote Sensing* as:

Sanchez-Lopez, N., Boschetti, L. and Hudak, A., 2018. Semi-Automated Delineation of Stands in an Even-Age Dominated Forest: A LiDAR-GEOBIA Two-Stage Evaluation Strategy. Remote Sensing, 10(10), p.1622.

Abstract

Regional scale maps of homogeneous forest stands are valued by forest managers and are of interest for landscape and ecological modelling. Research focused on stand delineation has substantially increased in the last decade thanks to the development of Geographic Object-Based Image Analysis (GEOBIA). Nevertheless, studies focused on even-age dominated forests are still few and the proposed approaches are often heuristic, local, or lacking objective evaluation protocols. In this study, we present a two-stage evaluation strategy combining both unsupervised and supervised evaluation methods for semi-automatic delineation of forest stands at regional scales using Light Detection and Ranging (LiDAR) raster summary metrics. The methodology is demonstrated on two contiguous LiDAR datasets covering more than 54,000 ha in central Idaho, where clearcuts were a common harvesting method during the twentieth century. Results show good delineation of even-aged forests and demonstrate the ability of LiDAR to discriminate stands harvested more than 50 years ago, that are generally challenging to discriminate with optical data. The two-stage strategy reduces the reference data required within the supervised evaluation and increases the scope of a reliable semi-automatic delineation to larger areas. This is an objective and straightforward approach that could potentially be replicated and adapted to address other study needs.

Introduction

Forest stands maps are valued for traditional forest inventory, to take silvicultural decisions, and develop forest managements plans (Leckie et al., 2003; Sullivan et al., 2009). The "stand" has traditionally been and largely remains the basic unit in forest management. It is often defined as a continuous community of trees uniform enough in class distribution, composition and structure, growing on a site of sufficiently uniform quality to be distinguishable from adjacent units (Helms, 1998). In the United States Pacific Northwest region, forests are dominated by coniferous species and structure (i.e., the horizontal and vertical distribution of components within the forest), rather than composition, is the main characteristic distinguishing stands with a history of silvicultural activities (e.g., clearcuts or thinnings) or natural disturbances (e.g., wildfires or insect outbreaks). On average, more than 50,000 km^2 are disturbed each year by harvest and wildfires in Canada and the United States

(Masek et al., 2013; White et al., 2017). The legacy of these disturbances is a patchwork of largely even-aged stands characterized by small age differences in their dominant cohort that is obvious to a skilled photo interpreter. Explicit spatial information of the boundaries of these stands available at regional scales are needed by forest managers (Leckie et al., 2003; Leckie and Gillis, 1995; Sullivan et al., 2009), and by ecologists and landscape modelers, as a source of information to locate past stand-replacing disturbances (Fisher et al., 2018).

Forest stand delineation is a task traditionally performed by visual photo interpretation of aerial photographs (Burnett and Blaschke, 2003; Leckie and Gillis, 1995) and, more recently, by applying semi-automated Geographic Object-based Image analysis (GEOBIA) on remotely sensed data (Dechesne et al., 2017; Koch et al., 2009; Leckie et al., 2003; Pascual et al., 2008; Sullivan et al., 2009; Tiede et al., 2004; Wulder et al., 2008). GEOBIA automatically generates image objects and links them to geographic features (e.g., forest stands) through a processing chain that incorporates, in a simple or iterative workflow, segmentation, evaluation, and classification techniques (Blaschke et al., 2014, 2008). The object-based strategy for semi-automatic delineation of geographic features is not a straightforward process, mainly because the selection of a suitable segmentation is not a standardized process. A user-defined evaluation is required to select among the vast number of possible outputs, considering the different set of input data, segmentation algorithms or algorithm parameters that can be selected within the GEOBIA process (Costa et al., 2018), and it should be carefully considered as the classification accuracy is highly influenced by segmentation quality (Liu and Xia, 2010; Walter, 2004).

Object-based segmentation evaluation strategies are divided into supervised and unsupervised methods (Zhang, 1996). Supervised methods compare segmentation outputs with a reference set of digitized objects, by computing dissimilarity metrics that are mainly based on location, size, shape, or color differences (Belgiu and Drăguţ, 2014; Clinton et al., 2010; Costa et al., 2018; Neubert et al., 2008; Zhang, 1997). These methods can be used to compare segmentation outputs obtained with different input datasets, but they rely on reference data that are not always available. In those cases, evaluation becomes an extremely time-consuming task, especially for large datasets. Additionally, the digitation of polygons as reference objects has some degree of subjectivity depending on how the samples are selected and who does the delineation (Johnson et al., 2015). Unsupervised methods, on the other hand, rank multiple image segmentations obtained from the same input dataset using a quality criterion that is usually related to some human perception of what a good segmentation should be (Espindola et al., 2006; Johnson and Xie, 2011). They rely only on the input data statistics and are gaining attention to objectively and automatically calibrate the segmentation algorithm parameters (Drăguţ et al., 2014; Espindola et al., 2006; Gao et al., 2017; Georganos et al., 2018; Gonzalez et al., 2018; Johnson and Xie,

2011; Johnson et al., 2015), but they are limited to compared segmentation outputs obtained with the same input data. Therefore, a more complex user-defined evaluation workflow is required to address other choices within the processing workflow having an influence in the segmentation quality (e.g., the input data).

Forest stand delineation using GEOBIA has been approached with different strategies and data sources depending often on the adopted definition of a forest stand that is generally based on species composition and age. In the last decades, Light Detection and Ranging (LiDAR) has been introduced for stand delineation as the main data source (e.g., Dechesne et al., 2016; Koch et al., 2009; Pascual et al., 2008; Sullivan et al., 2009; Varo-Martínez et al., 2017), or combined with optical remotely sensed data (e.g., Dechesne et al., 2017, 2016; Ke et al., 2010), especially when a structural component was considered to define the concept of the stand. Despite this effort, the number of publications focused on mapping forest stands mainly defined by different structural (e.g., canopy height and density) or age-related types is still relatively small, and the described strategies are often heuristic (e.g., Koch et al., 2009), local (covering areas smaller than 1000 ha) (e.g., Koch et al., 2009; Leppänen et al., 2008; Pascual et al., 2008; Sullivan et al., 2009; Varo-Martínez et al., 2017; Wu et al., 2014) or lacking objective evaluation protocols (e.g., Pascual et al., 2008; Sullivan et al., 2009). While these previous studies set the baseline to semi-automatically delineate forest stands of uniform age structure by coupling both GEOBIA and LiDAR-derived data, a generalized workflow to automate the delineation at larger scales is still not fully developed. Neither has a quantitative assessment on the performance of single LiDAR metrics (i.e., statistics summarizing the LiDAR point cloud) to delineate forest regardless of the time since the last disturbance yet been addressed, and it is of interest to understand if single-date remotely sensed data could eventually be used to locate historical stand-replacing events.

In this paper, we present a semi-automated and straightforward strategy for forest stand delineation using GEOBIA applied to single LiDAR-derived raster summary metrics in a study area covering more than 54,000 ha. Accordingly, the aim of this paper is twofold: (1) To integrate within the GEOBIA workflow a two-stage evaluation strategy to select objectively a suitable delineation of forest stands, defined in terms of structural and age homogeneity, when different segmentation algorithm parameters and input data layers are considered; and (2) to assess individually the performance of several LiDAR metrics to identify the boundaries of relatively old even-aged forest stands using ancillary reference data of historical stand-replacing disturbances.

Materials

Study area

The study area encompasses the Clear Creek, Selway River, and Elk Creek watersheds (~54,000 ha; Figure 1.1), located within the Nez Perce-Clearwater National Forest (46°48′N, 115°41′W) in north-central Idaho, USA. The study area covers mostly mountainous terrain, with slopes commonly higher than 50%; elevation is highly variable ranging from 415 to 2077 m. Average annual precipitation is around 740 mm; monthly mean temperature is −3.6 °C in winter and 14.2 °C in summer (Hijmans et al., 2005). The area is covered by a temperate mixed-conifer forest. Dominant tree species are Douglas-fir (Pseudotsuga menziesii (Mirb.) Franco.) and grand fir (Abies grandis (Douglas ex D. Don) Lindl.), commonly accompanied by western redcedar (Thuja plicata Donn ex D. Don) and ponderosa pine (Pinus ponderosa C. Lawson). Other species are only sporadically present.

Timber management in the study area initiated early in the twentieth century, but the total amount of timber harvested was relatively small until the 1940s (Cochrell, 1960); the area subsequently was intensively logged during the 1960s and 1970s, followed by a phased reduction in logging activity until present. Clearcuts and shelterwoods were the preferred management actions, resulting in a patchy landscape of even-aged forest stands (Space, 1964; USDA, Forest Service, 2016).

Ancillary Reference Data and Pre-Processing

The Forest Service ACtivity Tracking System (FACTs) harvest dataset was used as an independent source of information for the location and extent of timber harvest areas (USDA, Forest Service, 2016). The dataset is maintained by the U.S. Forest Service and consists of vector data (polygons) of the area treated as a part of the timber harvest program work, with an indication of the year in which the harvest was performed. The activities are self-reported by the Forest Service Units and consequently, reporting varies by National Forest administrative districts, and different information on planned management activities, historical records and other available data sources such as available cartography, aerial orthophotos, or remotely sensed data are used for its compilation. We selected clearcut harvest units larger than 2 ha present within the boundaries of our study area, resulting in a total of 360 polygons with 17.75 ha average size, logged between 1956 and 1996 (Figure 1.1).

Figure 1.1 shows that in many cases adjacent polygons were harvested in consecutive years. Because of the relatively low growth rate of the vegetation in the study area, these stands would have a substantially similar structure. Consequently, adjacent polygons harvested within a short time interval (≤5 years) were merged as exemplified in Figure 1.2.

LiDAR Datasets and Data Pre-Processing

Airborne LiDAR data were acquired in 2009 on the Clear Creek watershed (henceforth referred as the Clear Creek area) and in 2012 on the Selway River and Elk Creek watersheds (henceforth referred as the Selway area) (Figure 1.1). Both datasets were acquired using a Leica ALS60 sensor in multi-pulse mode up to 4 returns per pulse, with a 69,400 Hz pulse rate in the Clear Creek area and at 88,000 Hz in the Selway area. In both cases, the average point density was at least 4 points/m^2. The LiDAR data were delivered by the provider in a standard binary format (.las) with points labeled as ground or non-ground returns.

Because of the 3-year time difference between the two LiDAR collections, the two datasets were processed separately. The point cloud was normalized to obtain the height above ground of each LiDAR return using a digital terrain model (DTM) interpolated from the ground returns at 1-m spatial resolution. The FUSION toolkit (McGaughey, 2009) was used to compute gridded, summary LiDAR metrics at 30 m spatial resolution. The pixel size was selected at 30 m considering the extent of the study area and the average size of the reference forest stands. A total of 36 metrics was computed: 25 measures of vegetation canopy height and 11 measures of canopy density (Table 1.1). Density strata metrics were computed based on all returns so as not to discard useful information related to canopy complexity contained in the higher order returns (non-first returns). Cover metrics generated from both first returns and all returns were tested, because of some evidence that the former can produce more stable height metrics (Bater et al., 2011; Næsset, 2009), which may be more appropriate when combining datasets.

The number of metrics considered for further analysis was reduced based on their field significance and a user defined correlation threshold as many of them were spatially correlated. The 95th percentile of height (thereafter ‘H95′) was selected as it is highly correlated to stand height and biomass (González-Ferreiro et al., 2012; Heurich and Thoma, 2008; Hudak et al., 2008; Næsset, 2002), and it is less sensitive to outliers compared to other distributional metrics as the maximum height (MaxH) (Kane et al., 2010). On the other hand, the dominant cohort of trees to regenerate after a stand-replacing disturbance will grow tall only after a few decades (Bartels et al., 2016). A canopy density metric above a relatively high height would be sensitive to both younger stand regeneration patterns (showing clusters of low density of points) and older stands (showing clusters of high density of points). Accordingly, the percentage of points above 30 m (thereafter ‘Stratum above 30 m’) was also selected for analysis. Pairwise Pearson correlation coefficients (R) between these two metrics and all other 34 metrics were computed; and only the metrics with average absolute value of R lower than 0.5 (i.e., $|R| < 0.5$) both with ‘H95′ and ‘Stratum above 30 m’ were retained for the following steps of the analysis. All selected metrics were normalized between 0 and 100.

Table 1.2 shows the selected metrics for segmentation (seven in total) and the obtained pairwise Pearson′s correlation coefficients; Figure 1.3 displays an example of each of these metrics for a 4 × 4 km subset within the Clear Creek watershed.

Methods

The overall workflow of the proposed methodology is presented in Figure 1.4. The methodology involves: (1) The single-layer segmentation of several LiDAR metrics; (2) an object-based unsupervised evaluation to calibrate the segmentation algorithm parameters of each LiDAR metric; and (3) a supervised evaluation to select the optimal input LiDAR metric for the delineation of forest stands. An independent validation is performed to assess the accuracy of the optimal forest stand delineation.

Segmentation

Image segmentation of the seven LiDAR metrics was carried out using the multiresolution segmentation (MRS) algorithm (Baatz and Schape, 2000) implemented in eCognition 9.1 software.

The MRS is a bottom-up segmentation algorithm which starts with a single selected pixel, and merges neighboring pixels into bigger objects in a step-wise iterative process. A detailed description of the algorithm, which is one of the most commonly used algorithms in image segmentation of remotely sensed data within the GEOBIA domain, is provided by Baatz and Schape (2000); the eCognition implementation requires three user-defined parameters: Scale, shape, and compactness. The scale parameter (unitless, unbounded, and defined positive) controls the maximum heterogeneity within the objects; higher scale parameter values hence result in bigger objects. The shape and compactness parameters (unitless, with values defined between 0 and 1) control the border smoothness and compactness of the objects. For each selected LiDAR metric, we generated a set of segmentations by systematically varying the values of the three parameters. The range of variation of the three parameters established to ensure a full range of outputs ranging from undersegmentation to oversegmentation: 91 values of the scale parameter were used, ranging from 5 to 275 in increments of 3 units; three values (0.1, 0.5, and 0.9) were used for shape and compactness.

All the possible combinations of the three sets of values were tested, thus for each LiDAR metric and LiDAR dataset, a total of 819 segmentations was obtained.

Selection of the Optimal Segmentation of each LiDAR Metric

An unsupervised evaluation method based on spatial autocorrelation statistics was used for selecting the optimal segmentation for each LiDAR metric, out of the 819 generated with the sets of parameters defined above. The method is an adaptation of the one introduced by Espindola et al. (2006)

and subsequently used for object-based image segmentation evaluation of land cover and stand mapping (Johnson and Xie, 2011; Kim et al., 2009; Varo-Martínez et al., 2017).

Given a set of segmentations of the same image, the optimal segmentation is defined as the one that maximizes intra-segment homogeneity (i.e., the pixels belonging to the same segment are similar to each other) and inter-segment heterogeneity (i.e., neighboring segments are different from each other).

The intra-segment homogeneity is measured by the weighted variance ($wVar$):

$$wVar = \frac{\sum_{i=1}^{n} a_i \times v_i}{\sum_{i=1}^{n} a_i}, \quad (1)$$

where v_i and a_i are respectively the variance and the area of segment *i*, and *n* is the total number of segments. The upper bound of $wVar$ is equal to the variance of the image when only one image object is part of the segmentation; conversely, the lower bound of $wVar$ is be equal to 0 when each pixel in the image constitutes one image object.

The inter-segment heterogeneity is measured by Moran's I (MI) index:

$$MI = \frac{n \sum_{i=1}^{n} \sum_{j=1}^{n} w_{ij}(y_i - \bar{y})(y_j - \bar{y})}{(\sum_{i=1}^{n}(y_i - \bar{y})^2)(\sum_{i \neq j} \sum w_{ij})}, \quad (2)$$

where y_i is the mean value of segment *i*, y_j is the mean value of segment *j*, $\bar{y}$ is the mean of the pixel values of the entire image, and w_{ij} is a neighbor-based matrix assuming value $w_{ij} = 1$ if objects *i* and *j* are adjacent otherwise $w_{ij} = 0$. MI can assume values between −1 and 1: Values close to 1 represent clumped patterns with high spatial autocorrelation; values close to 0 represent random patterns; and values close to −1 represent dispersed patterns lacking spatial autocorrelation. MI was retrieved using the moran function on the R spdep package (Bivand et al., 2011).

Once $wVar$ and MI are calculated for all the segmentations of the same LiDAR metric, the scores are normalized as proposed by Böck et al. (2017). The weighted variance $wVar$ was normalized respective to the variance y' of the entire LiDAR metric image used as segmentation input:

$$wVar_{norm} = \frac{wVar}{y'}, \quad (3)$$

where $wVar$ is the weighted variance for the segmentation, and y' is the variance of the entire image used as segmentation input. Because $wVar$ may vary between 0 and y', $wVar_{norm}$ assumes values between 0 and 1.

MI was rescaled to the same 0–1 interval as follows:

$$MI_{norm} = \frac{MI+1}{2}, \quad (4)$$

The two normalized measures are then combined in a single measure, termed Global Score (GS) by Johnson and Xie (2011), and proposed as an objective function to rank the set of segmentation outputs and select the one resulting in the lowest GS. The original formulation of GS is a simple linear combination of $wVAr_{norm}$ and MI_{norm}; in order to avoid cases where the lowest GS is attained by a segmentation that is clearly undersegmenting (high $wVAr_{norm}$ but very low MI_{norm}) or oversegmenting (high MI_{norm} but very low $wVAr_{norm}$), we propose the use of a quadratic cost function, that privileges segmentations with balanced intra-segment homogeneity and inter-segment heterogeneity:

$$GS_{mod} = \sqrt{\frac{wVarnorm^2 + MInorm^2}{2}}, \quad (5)$$

GS_{mod} assumes values in the 0 to 1 range: values close to 0 being indicative of high intra-segment homogeneity and inter-segment heterogeneity; and values close to 1 being indicative of low intra-segment homogeneity and inter-segment heterogeneity.

For each of the seven LiDAR metrics considered, the segmentation with the lowest GS_{mod} was selected as optimal.

Selection of the Optimal LiDAR Metric

The second stage of the proposed methodology is to identify, among the set of seven optimal segmentations, the one that most closely matches even-aged stands as they are in reality, i.e., selecting which LiDAR metric is mostly suitable for forest stand delineation. A supervised evaluation method was used, based on measures of area dissimilarity between the segments (henceforth, image objects) and the FACTs harvest dataset, used as a reference map of even-aged forest stands (henceforth, reference objects).

Several metrics have been proposed in the literature as measures of area correspondence between image objects and reference objects (Clinton et al., 2010; Costa et al., 2018; Levine and Nazif, 1985; Liu et al., 2012; Lucieer and Stein, 2002; Möller et al., 2007; Monteiro and Campilho, 2006; Weidner, 2008; Zhan et al., 2005); these methods generally quantify oversegmentation and undersegmentation of the image objects. Oversegmentation happens when an identified reference object results in too many smaller image objects after the segmentation process. Conversely, undersegmentation occurs when the image object spatially matches with more than one of the reference objects, the image object being larger in size compared to the target feature of interest. An ideal, error-free segmentation would have no oversegmentation and no undersegmentation. In reality, each classification have some

oversegmentation and some undersegmentation: The selection of the optimal segmentation is therefore based on a ranking strategy that balances the two types of error (Clinton et al., 2010).

The adopted supervised evaluation method is based on measures of area dissimilarity proposed by Clinton et al. (2010). We define as $Y = \{y_j : j = 1 \ldots . m\}$ the set of all the image objects, and as $X = \{x_i : i = 1 \ldots . n\}$ the set of all the reference objects. For each reference object x_i, Y_i^* is the set of corresponding image objects, defined as all image objects of Y whose area overlaps by more than 50% with the reference object (i.e., $y_j : \frac{\text{area}(x_i \cap y_j)}{\text{area}(y_j)} > 0.5$); or conversely if the reference object overlaps more than half of the segmented object (i.e., $y_j : \frac{\text{area}(x_i \cap y_j)}{\text{area}(x_i)} > 0.5$) (Zhan et al., 2005). This 50% overlapping area criterion has been consistently used as an appropriate threshold for object-based quality assessment (Clinton et al., 2010; Drăguţ et al., 2014; Liu et al., 2012).

The measures of oversegmentation (OS) and undersegmentation (US) (Clinton et al., 2010) are calculated by starting with pair-wise comparisons between image objects and corresponding reference objects, which are then summarized for the entire image.

For each image object y_j, $\left(y_j \in Y_i^*\right)$ and corresponding reference object x_i the oversegmentation (OS_{ij}) is calculated as the fraction of overlapping area relative to the area of the reference object:

$$OS_{ij} = 1 - \frac{\text{area}(x_i \cap y_j)}{\text{area}(x_i)}, \tag{6}$$

Conversely, undersegmentation (US_{ij}) is calculated as the fraction of overlapping area, relative to the area of the image object:

$$US_{ij} = 1 - \frac{\text{area}(x_i \cap y_j)}{\text{area}(y_j)}, \tag{7}$$

OS_{ij} is then aggregated into the overall oversegmentation of object x_i:

$$OS_i = \frac{\sum_{y_j \in Y_i^*} OS_{ij}}{\#y_j \in Y_i^*}, \tag{8}$$

and OS_i is aggregated as the total oversegmentation of the n reference objects:

$$OS = \frac{\sum_i^n OS_i}{n}, \tag{9}$$

Likewise, US_{ij} is aggregated into the overall undersegmentation of object x_i:

$$US_i = \frac{\sum_{y_j \in Y_i^*} US_{ij}}{\#y_j \in Y_i^*}, \tag{10}$$

and US_i is aggregated as the total undersegmentation of the n reference objects:

$$US = \frac{\sum_i^n US_i}{n}, \tag{11}$$

To select the optimal metrics, OS and US were combined into a summary score (D):

$$D = \sqrt{\frac{OS^2 + US^2}{2}}, \tag{12}$$

In the cases where no corresponding objects for a specific reference object were found according to the defined 50% overlapping area criterion (i.e., $\#y_j \in Y_i^* = 0$), OS_i and US_i were given a value of 1.

Once the optimal segmentations of each LiDAR metric were evaluated, the LiDAR metric whose segmentation results in the lowest D score was selected as optimal.

In order to investigate whether the same metric results in the optimal segmentation regardless of time since disturbance, the metrics of area agreement were computed using as reference objects different subsets of the FACTS harvest polygons, resulting in four scenarios:

1. All clearcuts (years from 1956 to 1996);
2. clearcuts performed before the start of the Landsat MSS record (years from 1956 to 1972);
3. clearcuts performed before the start of the Landsat TM record (years from 1956 to 1984);
4. clearcuts performed after the start of the Landsat TM record (years from 1984 to 1996).

The four scenarios are driven by the Landsat data archive since it is the longest available Earth Observation record, starting with the launch of Landsat-1 in 1972.

Validation

The segmentation selected through the two-stage semi-automatic procedure was validated by comparing it to a randomly selected set of reference objects, derived from visual interpretation. The accuracy of the segmentation was assessed using area-based dissimilarity measures.

Reference dataset

The FACTS dataset is a valuable record of historical disturbances, but it is not intended to be a wall-to-wall map of stand boundaries. While the presence of a polygon indicates a documented, historical clearcut, the absence of a polygon might indicate the absence of historical data, rather than an undisturbed stand. For this reason, an independent reference dataset encompassing both even-aged (EAF) and undisturbed uneven-aged (UAF) forest stands was developed. Reference objects were

delineated through visual interpretation of the 1-m spatial resolution digital orthophotos acquired from the National Agricultural Imagery Program (NAIP). Tri-dimensional renderings of the normalized LiDAR point clouds, as well as the raster LiDAR metrics, were used as additional data sources in the interpretation. NAIP imagery acquired in 2009 was used for the Clear Creek dataset, and 2011 imagery (closer in time to the LiDAR flight) was used for the Selway dataset.

The reference objects were generated as follows:

1. Random selection of an image object of the optimal segmentation, to account for the large disparity in stand area, followed by random selection of a point within the object (Radoux and Bogaert, 2017);
2. visual interpretation of the NAIP imagery to trace the forest stand that includes the point. Any physical barriers such as roads or watersheds were used to delineate the border of the stands when no other natural discontinuity related to vegetation type or structure was found;
3. classification of the reference object as EAF or uneven-aged forest by the photo-interpreter.

A total of 100 reference objects were generated: 25 EAF and 25 UAF objects for each of the two study areas.

Validation Metrics

The validation metrics used to characterize the agreement and disagreement between image objects and reference objects are:

- Oversegmentation (OS), undersegmentation (US) and summary score (D), obtained with the procedure described in "Selection of the Optimal LiDAR Metric" section;
- modified oversegmentation (OS^*), undersegmentation (US^*), and summary score (D^*), defined as follows.

The modified area-based dissimilarity metrics (OS^*, US^*, D^*) are defined as the benchmark value of (*OS, US, D*), that could be achieved in the best case scenario when the image objects identified by the segmentation are post-processed and merged through object-based classification. The issue is illustrated in Figure 1.5, where two significantly different segmentations are compared to the same reference object. The top row shows a case of oversegmentation, where an almost perfect match could be achieved through classification, if all the corresponding image objects are merged. Conversely, the bottom row shows a case of where significant discrepancies could not be resolved through classification

of the image objects. This is reflected by the modified metrics (Figure 1.5, right column) where (OS^*, US^*, D^*) represent the areal disagreement between the reference object and the best possible aggregation of the image objects. The modified metrics are significant for the specific application of forest stand mapping, where the segmentation should not be seen as an end-product per se, but as an input dataset for further classification of forest characteristics. We expect the difference between (*OS*, *US*, *D*) and *(OS*, US*, D**) to be particularly significant on UAF stands, that due to their larger size and heterogeneity compared to EAF are expected to show a high degree of oversegmentation, that might be however resolved through post-processing.

The modified metrics are computed by considering, instead of the single image objects y_j corresponding to a reference object x_i, their union y_i^* defined as:

$$y_i^* = \cup_{y_j \in Y_i^*} y_i, \tag{13}$$

being Y_i^* the subset set of corresponding image objects defined considering the 50% overlapping area criterion (see "Selection of the Optimal LiDAR Metric" section); by definition y* the best possible result of a post-processing of the segmentation.

For each reference object x_i the modified oversegmentation OS_i^* is calculated as the fraction of overlapping area with y_i^* relative to the area of the reference object:

$$OS_i^* = 1 - \frac{area\left(x_i \cap y_i^*\right)}{area\left(x_i\right)}, \tag{14}$$

OS_i^* (14) is then aggregated into an overall oversegmentation metric for the entire set of n reference objects:

$$OS^* = \frac{\sum_i^n OS_i^*}{n}, \tag{15}$$

Similarly, the modified undersegmentation US_i^* is calculated for each reference object as:

$$US_i^* = 1 - \frac{area\left(x_i \cap y_i^*\right)}{area\left(y_i^*\right)}, \tag{16}$$

and US_i^* (16) is aggregated into an overall undsersegmentation metric:

$$US^* = \frac{\sum_i^n US_i^*}{n}, \tag{17}$$

Finally, the modified summary D^* score is calculated as the quadratic cost function of OS^* and US^*:

$$D^* = \sqrt{\frac{OS^{*2} + US^{*2}}{2}}, \quad (18)$$

Results

Selection of the Optimal Segmentation of each LiDAR Metric

The procedure described in "Selection of the Optimal Segmentation of each LiDAR Metric" section, was used for the evaluation of the 819 segmentations obtained for each LiDAR metric using different sets of MRS algorithm parameters (scale, shape, and compactness). Figure 1.6 illustrates, using the 'H95′ metric as an example, that different scale and shape parameters influence the number, shape, and size of the segments, as discussed in (Baatz and Schape, 2000).

The measures of spatial autocorrelation ($wVAr_{norm}$, MI_{norm}) were computed for each segmentation, and the summary score (GS_{mod}) was used for ranking them. Figure 1.7 exemplifies the procedure for the selection of the optimal segmentation, showing the scatter-plot of the $wVAr_{norm}$ and MI_{norm} value of each segmentation of the 'H95′ LiDAR metric of the Clear Creek dataset, as well as the isoline $GS_{mod} = 0.37$ corresponding to the optimal segmentation.

In general, for each LiDAR metric, the parameters that generate the optimal segmentation on both datasets are very similar (Table 1.3). For instance, the shape is always 0.1, and the scale parameter between both datasets never differ more than a scale increment of 3 units. A notable exception is the 'Stratum above 30 m' metric, where the optimal scale parameter is 59 on the Clear Creek dataset and 23 on the Selway dataset. This difference can be explained considering the low sensitivity of this metric to vegetation recovery: the percentage of returns above 30 m will remain negligible until the top of the trees is higher than 30 m, which might take several decades after a stand-replacing disturbance. In the Clear Creek area many clearcuts are adjacent or spatially close to each other (Figure 1.1); because of the low sensitivity of the metric, there is no clear distinction in the "Stratum above 30 m" metric between neighboring disturbed stands, and the optimal segmentation is the one identifying these very large image objects. Figure 1.1 shows that the clearcuts of the Selway area are instead surrounded by undisturbed stands, generating a more heterogenous patchy landscape that create recognizable stand boundaries despite the low sensitivity of the 'Stratum above 30 m' metric.

Figure 1.8 illustrates that the optimal segmentation of different LiDAR metrics might show very different vegetation-related structural objects. While in general the image objects that can visually recognized in each of the LiDAR metrics are delineated by the optimal segmentation, not all metrics return image objects that match the historic disturbances reported by the FACTS dataset. Figure 1.8

shows that the ‘H95′ and ‘Stratum above 30 m’ visually match closely the FACT dataset, whereas the other metrics define image objects that do not immediately relate to the record of past clearcuts.

Selection of the Optimal LiDAR Metric

The optimal segmentation of each LiDAR metric was compared against the reference objects from the FACTs harvest dataset following the procedure described in “Selection of the Optimal LiDAR Metric” section; the results of the analysis, for the two study areas and for the four scenarios of time since disturbances, are summarized in Table 1.4. The ‘H95′ metric results in the lowest D value for both datasets in all but one case (Table 1.4), namely when considering only the most recent disturbances (1984–1996) on the Clear Creek dataset. In this case, the ‘Stratum 20–30 m’ metric results in the lowest score (D = 22), with the ‘H95′ metric having the second lowest score (D = 0.25). Conversely, the ‘Stratum 20–30 m’ metric is the second-best metric of the remaining three scenarios in the Clear Creek area, and the ‘Stratum above 30 m’ is always the second-best metric in the Selway area. Additionally, the optimal segmentation of the ‘H95′ metric is the only one where all the reference objects have a non-null set of matching image objects (i.e., $Y_i^* \neq \emptyset \; \forall \; x_i$) (Table 1.4).

The ‘H95′ LiDAR metric was therefore selected as the optimal metric. Figure 1.9 shows the segmentation of the ‘H95′ LiDAR metric as the optimal delineation for even-aged forest stand mapping in the study area.

Validation

One hundred reference objects were manually delineated (Figures 1.10 and 1.11) to validate the optimal segmentation results, as described in “Validation” section. This sample size corresponds to 8% of the total number of image objects identified by the optimal segmentation (1182 objects in total, as reported in Table 1.3), and the resulting reference dataset covers 16% of the surface of the study area. The reference sample size is comparable with previous GEOBIA-based studies (Drăguţ et al., 2014; Heenkenda et al., 2015; Liu et al., 2012).

The independent validation performed with the visually interpreted polygons representing both EAF and UAF stands confirmed the good match between image objects and forest stands. On EAF stands, in particular, in most cases there was a 1-to-1 correspondence between the EAF reference objects and the set of corresponding image objects; whereas UAF reference objects were generally undersegmented, and corresponded to several image objects (Figure 1.10). The validation also showed that, in a few isolated cases, the ‘H95′ metric has an abnormal behavior on very recent clearcuts, as in the example of Figure 1.11, third row, where a recently harvested stand is not visible in the LiDAR raster. This is due to the specific definition of the ‘H95′ metric (Table 1.1): In the absence of vegetation

regrowth the majority of returns are classified as 'ground', and the 95th percentile of the non-ground returns corresponds to the height of isolated trees left standing for seedling after the clearcut.

The area based dissimilarity metrics, reported in Table 1.5, indicate that the overall performance (summarized by the D score) is very similar across the two datasets ($D_{Clear\ Creek}$= 0.26 and $D_{Selway} = 0.27$ when considering all objects), with consistently higher accuracy on EAF stands ($D_{Clear\ Creek}$= 0.15 and D_{Selway}= 0.16) than on UAF stands ($D_{Clear\ Creek} = 0.37$ and $D_{Selway} = 0.39$). This difference is largely due to the high rates of oversegmentation on UAF stands in both datasets ($OS_{Clear\ Creek,UAF} = 0.39$ vs $OS_{Clear\ Creek,EAF} = 0.12$; and $OS_{Selway,UAF} = 0.50$ vs $OS_{Selway,EAF} = 0.22$).

As discussed in "Validation" section, the modified metrics (OS^*, US^*, D^*) represent the benchmark level of error that could be achieve through the best possible post-processing of the segmentation. The modified metrics indicate that post-processing has the potential to significantly reduce the areal disagreements due to oversegmentation, especially over UAF stands ($D^*_{Clear\ Creek,UAF} = 0.31$ vs $D_{Clear\ Creek,UAF} = 0.37, D^*_{Selway,UAF} = 0.21$ vs $D_{Selway,UAF} = 0.39$).

Discussion

In the present paper we propose the integration in the same workflow of an object-based unsupervised evaluation (which allows for the selection of the optimal parameters to automatically segment an image) and an object-based supervised evaluation (which allows for the selection of the best match between a segmentation and independently derived reference objects) to identify objectively an optimal delineation output. Unsupervised methods favor automatic ranking of multiple segmentations obtained by changing the parameters of an algorithm on the same input data, without requiring any contribution from the operator, or any external datasets. They do not, however, allow for ranking segmentations obtained on the same area from different input data, as in the case of the LiDAR raster metrics examined in this paper, which reflect different structural characteristics of the vegetation, as evident in Figure 1.3. Supervised evaluation methods instead allow for ranking any segmentation—whether it is generated from the same image or not—but rely entirely on reference data, whose generation is generally an expensive and time-consuming task (Zhang et al., 2008). As a consequence, supervised evaluation methods are generally employed only on relatively small datasets (Johnson and Xie, 2011). The combination of these two standard object-based evaluation strategies, as proposed in this paper, reduces considerably the amount of required reference data and increases the scope of a reliable semi-automatic delineation to larger areas.

The application of the proposed methodology to LiDAR data demonstrates that a single LiDAR raster metric, the 'H95′ metric, can be used to delineate even-aged forest stands in a semi-automatic way. In particular, the results show that forest stands harvested in the 1950s and 1960s can still be accurately delineated (Table 1.4). This result is particularly significant, because it implies that LiDAR data can be potentially used to reconstruct the disturbance history of a forest extending beyond the optical satellite data record.

The optimal segmentation was validated against a randomly selected reference dataset. The reference objects were manually delineated by a skilled photo-interpreter, based on imagery of higher resolution (1 m NAIP data) and richer thematic content (3D LiDAR point clouds) than the 30 m LiDAR raster. While there is a degree of subjectivity, visually interpreted reference data are commonly used for the validation of land cover and land cover disturbance satellite products (e.g., Boschetti et al., 2016; Strahler et al., 2006), and for the validation of GEOBIA outputs (e.g., Drăguţ et al., 2014; Heenkenda et al., 2015; Johnson and Xie, 2011; Leppänen et al., 2008; Liu et al., 2012; Varo-Martínez et al., 2017).

The independent validation confirmed the good overall match between image objects and visually interpreted polygons, albeit with higher accuracy on EAF than on UAF forest stands. At least in part, the low accuracy on UAF stands might be attributed to the lack of objective UAF stand definition, and to the difficulty for the interpreter to consistently identify natural breaks between contiguous, mature, uneven-aged forest stands. The validation also highlighted some limitations of the 'H95′ metric. The optimal segmentation showed undersegmentation errors (e.g., Figure 1.11, third row) on small stands recently (<10 year) harvested, where mature trees are left standing at regular intervals to spread seeds (e.g., shelterwood cutting). At time of the LiDAR acquisition the majority of the young regenerating seedlings have a height below 1.37 m (the cutoff used for the raster height metrics), and the 'H95′ metric therefore reflects the height of the mature trees left standing. We hypothesize that the combined use of multiple LiDAR metrics (such as the 'Stratum 20–30 m' which ranked second in the supervised evaluation) might overcome this particular issue.

Previous research to delineate structural or age-related forest stand types using object-based techniques and LiDAR data (e.g., Koch et al., 2009; Leppänen et al., 2008; Pascual et al., 2008; Sullivan et al., 2009; Varo-Martínez et al., 2017; Wu et al., 2014) did not propose methodologies that could be easily applied outside the original study areas, due to the complexity of the workflow (e.g., Koch et al., 2009), to the exploitation of site-specific forest characteristics and to the small extent of the study areas (e.g., Leppänen et al., 2008; Pascual et al., 2008; Sullivan et al., 2009; Wu et al., 2014), and to the lack of objective evaluation protocols (e.g., Pascual et al., 2008; Sullivan et al., 2009). The proposed two-stage evaluation strategy is a general objective workflow, that could be easily replicated and adapted to

other study sites, to other data sources, and to delineate different features of the landscape. Overall, we expect that the same 'H95′ metric could be optimal, at the working resolution, in other areas with similar species composition and with similar disturbance dynamics (such as most of the Pacific Northwest of the United States), and that the optimal set of parameters of the MRS algorithm for each area could be identified through an unsupervised selection procedure, hence without the need for additional independent reference data. Additional validation would be required to verify whether the same LiDAR metric could be also used for delineating forest stands resulting from disturbances and management practices other than clearcuts. Future research will (1) evaluate a different set of single or combined LiDAR metrics for segmentation (e.g., texture metrics, rumple index, local maxima derived from the CHM); and (2) develop a rule-based fusion between segmentations generated from complementary metrics and different harvest treatments, as some limitations in the detection of recent disturbances has been observed after the independent validation was addressed.

Conclusions

This paper proposes a two-stage, semi-automatic evaluation strategy for object-based forest stand delineation and implements it on two contiguous LiDAR datasets covering more than 54,000 ha in the Clear Creek and Selway watersheds in Central Idaho. The paper was designed to address two main objectives: (1) To integrate a straightforward and objective workflow for forest stand delineation that can be easily replicated and adapted at regional scales; and (2) to evaluate the performance of commonly used rasterized LiDAR metrics, such as 'H95′ in this study, to identify in a semi-automatic way the boundaries of relatively old even-aged forest stands.

With regards to the first objective, the proposed strategy allows the user to automatically select the optimal set of MRS algorithm segmentation parameters to delineate image objects for each tested LiDAR metric, and to identify the LiDAR metric that ensures the best match between image objects (i.e., the segmentation) and a set of reference objects (i.e., the forest stands as independently delineated). With regards to the second objective, the application of the methodology to LiDAR data demonstrates that commonly used LiDAR raster metrics, namely distributional metrics of canopy height, can be used to accurately delineate even-aged forest stands (>2 ha) in a semi-automatic way and that forest stands older than 50 years can be identified at working resolution of 30 m. This is a particularly significant result, considering that stand maps conventionally generated from change detection using optical satellite data can only extend, in the best case, to the beginning of the Landsat MSS record in 1972.

GEOBIA strategies to delineate forest stands at regional scales are promising to generate forest stands maps ready to use, but generalized protocols are still required. The most effective way to approach the delineation would depend on the adopted definition of a forest stand (e.g., based on species

composition, structure, etc.). In any case, robust evaluation strategies would be required to assure a minimum quality on the final selected output. We proposed here a straightforward and objective two-stage evaluation workflow to delineate forest stands defined in terms of age and structural homogeneity. Our study shows that relatively old stands are accurately discriminated using one single-date LiDAR raster metric, which is promising result not only to produce even-aged forest stand maps but also to eventually characterize forest stands in terms of time since the last disturbance. Additionally, this methodology can be adapted to address future study needs, such as to improve stand delineation methods, or to map other geographic features of the landscape.

Acknowledgements

The project is supported by NASA award number NHX14AD92G and by USDA NIFA grant number 2011-32100-06016. Publication of this article was funded by the University of Idaho Open Access Publishing Fund

References

Baatz, M., Schape, A., 2000. Multiresolution Segmentation–an optimization approach for high quality multi-scale image segmentation. AGIT-Symposium Salzburg 2000, 12–23.

Bartels, S.F., Chen, H.Y.H., Wulder, M.A., White, J.C., 2016. Trends in post-disturbance recovery rates of Canada's forests following wildfire and harvest. For. Ecol. Manag. 361, 194–207. https://doi.org/10.1016/j.foreco.2015.11.015

Bater, C.W., Wulder, M.A., Coops, N.C., Nelson, R.F., Hilker, T., Nasset, E., 2011. Stability of Sample-Based Scanning-LiDAR-Derived Vegetation Metrics for Forest Monitoring. IEEE Trans. Geosci. Remote Sens. 49, 2385–2392. https://doi.org/10.1109/TGRS.2010.2099232

Belgiu, M., Drăguț, L., 2014. Comparing supervised and unsupervised multiresolution segmentation approaches for extracting buildings from very high resolution imagery. ISPRS J. Photogramm. Remote Sens. 96, 67–75. https://doi.org/10.1016/j.isprsjprs.2014.07.002

Bivand, R., Anselin, L., Berke, O., Bernat, A., Carvalho, M., Chun, Y., Dormann, C.F., Dray, S., Halbersma, R., Lewin-Koh, N., others, 2011. spdep: Spatial dependence: weighting schemes, statistics and models. R package version 0.5-31, URL http://CRAN. R-project. org/package= spdep.

Blaschke, T., Hay, G.J., Kelly, M., Lang, S., Hofmann, P., Addink, E., Queiroz Feitosa, R., van der Meer, F., van der Werff, H., van Coillie, F., Tiede, D., 2014. Geographic Object-Based Image

Analysis – Towards a new paradigm. ISPRS J. Photogramm. Remote Sens. 87, 180–191. https://doi.org/10.1016/j.isprsjprs.2013.09.014

Blaschke, T., Lang, S., Hay, G., 2008. Object-Based Image Analysis: Spatial Concepts for Knowledge-Driven Remote Sensing Applications. Springer Science & Business Media.

Böck, S., Immitzer, M., Atzberger, C., 2017. On the Objectivity of the Objective Function—Problems with Unsupervised Segmentation Evaluation Based on Global Score and a Possible Remedy. Remote Sens. 9, 769. https://doi.org/10.3390/rs9080769

Boschetti, L., Stehman, S.V., Roy, D.P., 2016. A stratified random sampling design in space and time for regional to global scale burned area product validation. Remote Sens. Environ. 186, 465–478. https://doi.org/10.1016/j.rse.2016.09.016

Burnett, C., Blaschke, T., 2003. A multi-scale segmentation/object relationship modelling methodology for landscape analysis. Ecol. Model., Landscape Theory and Landscape Modelling 168, 233–249. https://doi.org/10.1016/S0304-3800(03)00139-X

Clinton, N., Holt, A., Scarborough, J., Yan, L.I., Gong, P., 2010. Accuracy assessment measures for object-based image segmentation goodness. Photogramm. Eng. Remote Sens. 76, 289–299.

Cochrell, A.N., 1960. The Nezperce Story: A History of the Nezperce National Forest.

Costa, H., Foody, G.M., Boyd, D.S., 2018. Supervised methods of image segmentation accuracy assessment in land cover mapping. Remote Sens. Environ. 205, 338–351. https://doi.org/10.1016/j.rse.2017.11.024

Dechesne, C., Mallet, C., Le Bris, A., Gouet, V., Hervieu, A., 2016. Forest stand segmentation using airborne lidar data and very high resolution multispectral imagery. ISPRS Arch. Photagrammetry Remote Sens.

Dechesne, C., Mallet, C., Le Bris, A., Gouet-Brunet, V., 2017. Semantic segmentation of forest stands of pure species combining airborne lidar data and very high resolution multispectral imagery. ISPRS J. Photogramm. Remote Sens. 126, 129–145. https://doi.org/10.1016/j.isprsjprs.2017.02.011

Drăguţ, L., Csillik, O., Eisank, C., Tiede, D., 2014. Automated parameterisation for multi-scale image segmentation on multiple layers. ISPRS J. Photogramm. Remote Sens. 88, 119–127. https://doi.org/10.1016/j.isprsjprs.2013.11.018

Espindola, G.M., Camara, G., Reis, I.A., Bins, L.S., Monteiro, A.M., 2006. Parameter selection for region-growing image segmentation algorithms using spatial autocorrelation. Int. J. Remote Sens. 27, 3035–3040. https://doi.org/10.1080/01431160600617194

Fisher, R.A., Koven, C.D., Anderegg, W.R., Christoffersen, B.O., Dietze, M.C., Farrior, C.E., Holm, J.A., Hurtt, G.C., Knox, R.G., Lawrence, P.J., 2018. Vegetation demographics in Earth System Models: A review of progress and priorities. Glob. Change Biol. 24, 35–54.

Gao, H., Tang, Y., Jing, L., Li, H., Ding, H., 2017. A Novel Unsupervised Segmentation Quality Evaluation Method for Remote Sensing Images. Sensors 17, 2427. https://doi.org/10.3390/s17102427

Georganos, S., Lennert, M., Grippa, T., Vanhuysse, S., Johnson, B., Wolff, E., 2018. Normalization in Unsupervised Segmentation Parameter Optimization: A Solution Based on Local Regression Trend Analysis. Remote Sens. 10, 222. https://doi.org/10.3390/rs10020222

Gonzalez, R.S., Latifi, H., Weinacker, H., Dees, M., Koch, B., Heurich, M., 2018. Integrating LiDAR and high-resolution imagery for object-based mapping of forest habitats in a heterogeneous temperate forest landscape. Int. J. Remote Sens. 0, 1–26. https://doi.org/10.1080/01431161.2018.1500071

González-Ferreiro, E., Diéguez-Aranda, U., Miranda, D., 2012. Estimation of stand variables in Pinus radiata D. Don plantations using different LiDAR pulse densities. Forestry 85, 281–292. https://doi.org/10.1093/forestry/cps002

Heenkenda, M.K., Joyce, K.E., Maier, S.W., 2015. Mangrove tree crown delineation from high-resolution imagery. Photogramm. Eng. Remote Sens. 81, 471–479.

Helms, J., 1998. The Dictionary of Forestry. Western Heritage Co.

Heurich, M., Thoma, F., 2008. Estimation of forestry stand parameters using laser scanning data in temperate, structurally rich natural European beech (Fagus sylvatica) and Norway spruce (Picea abies) forests. Forestry 81, 645–661.

Hijmans, R.J., Cameron, S.E., Parra, J.L., Jones, P.G., Jarvis, A., 2005. Very high resolution interpolated climate surfaces for global land areas. Int. J. Climatol. 25, 1965–1978. https://doi.org/10.1002/joc.1276

Hudak, A.T., Crookston, N.L., Evans, J.S., Hall, D.E., Falkowski, M.J., 2008. Nearest neighbor imputation of species-level, plot-scale forest structure attributes from LiDAR data. Remote

Sens. Environ., Earth Observations for Terrestrial Biodiversity and Ecosystems Special Issue 112, 2232–2245. https://doi.org/10.1016/j.rse.2007.10.009

Johnson, B., Xie, Z., 2011. Unsupervised image segmentation evaluation and refinement using a multi-scale approach. ISPRS J. Photogramm. Remote Sens. 66, 473–483. https://doi.org/10.1016/j.isprsjprs.2011.02.006

Johnson, B.A., Bragais, M., Endo, I., Magcale-Macandog, D.B., Macandog, P.B.M., 2015. Image Segmentation Parameter Optimization Considering Within- and Between-Segment Heterogeneity at Multiple Scale Levels: Test Case for Mapping Residential Areas Using Landsat Imagery. ISPRS Int. J. Geo-Inf. 4, 2292–2305. https://doi.org/10.3390/ijgi4042292

Kane, V.R., McGaughey, R.J., Bakker, J.D., Gersonde, R.F., Lutz, J.A., Franklin, J.F., 2010. Comparisons between field- and LiDAR-based measures of stand structural complexity. Can. J. For. Res. 40, 761–773. https://doi.org/10.1139/X10-024

Ke, Y., Quackenbush, L.J., Im, J., 2010. Synergistic use of QuickBird multispectral imagery and LIDAR data for object-based forest species classification. Remote Sens. Environ. 114, 1141–1154. https://doi.org/10.1016/j.rse.2010.01.002

Kim, M., Madden, M., Warner, T.A., 2009. Forest Type Mapping using Object-specific Texture Measures from Multispectral Ikonos Imagery. Photogramm. Eng. Remote Sens. 75, 819–829. https://doi.org/10.14358/PERS.75.7.819

Koch, B., Straub, C., Dees, M., Wang, Y., Weinacker, H., 2009. Airborne laser data for stand delineation and information extraction. Int. J. Remote Sens. 30, 935–963.

Leckie, D.G., Gillis, M.D., 1995. Forest inventory in Canada with emphasis on map production. For. Chron. 71, 74–88. https://doi.org/10.5558/tfc71074-1

Leckie, D.G., Gougeon, F.A., Walsworth, N., Paradine, D., 2003. Stand delineation and composition estimation using semi-automated individual tree crown analysis. Remote Sens. Environ. 85, 355–369. https://doi.org/10.1016/S0034-4257(03)00013-0

Leppänen, V.J., Tokola, T., Maltamo, M., Mehtätalo, L., Pusa, T., Mustonen, J., 2008. Automatic delineation of forest stands from LiDAR data, in: GEOBIA, 2008 – Pixels, Objects, Intelligence: GEOgraphic Object Based Image Analysis for the 21st Century. Presented at the GEOBIA, 2008 – Pixels, Objects, Intelligence: GEOgraphic Object Based Image Analysis for the 21st Century, University of Calgary, Calgary, Alberta, Canada., pp. 271–277.

Levine, M.D., Nazif, A.M., 1985. Dynamic Measurement of Computer Generated Image Segmentations. IEEE Trans. Pattern Anal. Mach. Intell. PAMI-7, 155–164. https://doi.org/10.1109/TPAMI.1985.4767640

Liu, D., Xia, F., 2010. Assessing object-based classification: advantages and limitations. Remote Sens. Lett. 1, 187–194. https://doi.org/10.1080/01431161003743173

Liu, Y., Bian, L., Meng, Y., Wang, H., Zhang, S., Yang, Y., Shao, X., Wang, B., 2012. Discrepancy measures for selecting optimal combination of parameter values in object-based image analysis. ISPRS J. Photogramm. Remote Sens. 68, 144–156. https://doi.org/10.1016/j.isprsjprs.2012.01.007

Lucieer, A., Stein, A., 2002. Existential uncertainty of spatial objects segmented from satellite sensor imagery. IEEE Trans. Geosci. Remote Sens. 40, 2518–2521. https://doi.org/10.1109/TGRS.2002.805072

Masek, J.G., Goward, S.N., Kennedy, R.E., Cohen, W.B., Moisen, G.G., Schleeweis, K., Huang, C., 2013. United States Forest Disturbance Trends Observed Using Landsat Time Series. Ecosystems 16, 1087–1104. https://doi.org/10.1007/s10021-013-9669-9

McGaughey, R.J., 2009. FUSION/LDV: Software for LIDAR data analysis and visualization. US Dep. Agric. For. Serv. Pac. Northwest Res. Stn. Seattle WA USA 123.

Möller, M., Lymburner, L., Volk, M., 2007. The comparison index: A tool for assessing the accuracy of image segmentation. Int. J. Appl. Earth Obs. Geoinformation 9, 311–321. https://doi.org/10.1016/j.jag.2006.10.002

Monteiro, F.C., Campilho, A.C., 2006. Performance Evaluation of Image Segmentation, in: Campilho, A., Kamel, M.S. (Eds.), Image Analysis and Recognition. Springer Berlin Heidelberg, Berlin, Heidelberg, pp. 248–259. https://doi.org/10.1007/11867586_24

Næsset, E., 2009. Effects of different sensors, flying altitudes, and pulse repetition frequencies on forest canopy metrics and biophysical stand properties derived from small-footprint airborne laser data. Remote Sens. Environ. 113, 148–159.

Næsset, E., 2002. Predicting forest stand characteristics with airborne scanning laser using a practical two-stage procedure and field data. Remote Sens. Environ. 80, 88–99. https://doi.org/10.1016/S0034-4257(01)00290-5

Neubert, M., Herold, H., Meinel, G., 2008. Assessing image segmentation quality – concepts, methods and application, in: Blaschke, T., Lang, S., Hay, G.J. (Eds.), Object-Based Image Analysis, Lecture Notes in Geoinformation and Cartography. Springer Berlin Heidelberg, pp. 769–784. https://doi.org/10.1007/978-3-540-77058-9_42

Pascual, C., García-Abril, A., García-Montero, L.G., Martín-Fernández, S., Cohen, W.B., 2008. Object-based semi-automatic approach for forest structure characterization using lidar data in heterogeneous Pinus sylvestris stands. For. Ecol. Manag. 255, 3677–3685. https://doi.org/10.1016/j.foreco.2008.02.055

Radoux, J., Bogaert, P., 2017. Good Practices for Object-Based Accuracy Assessment. Remote Sens. 9, 646.

Space, R.S., 1964. Clearwater story: a history of the Clearwater National Forest.

Strahler, A.H., Boschetti, L., Foody, G.M., Friedl, M.A., Hansen, M.C., Herold, M., Mayaux, P., Morisette, J.T., Stehman, S.V., Woodcock, C.E., 2006. Global Land Cover Validation: Recommendations for Evaluation and Accuracy Assessment of Global Land Cover Maps. European Communities, Luxembourg 51(4).

Sullivan, A.A., McGaughey, R.J., Andersen, H.-E., Schiess, P., 2009. Object-oriented classification of forest structure from light detection and ranging data for stand mapping. West. J. Appl. For. 24, 198–204.

Tiede, D., Blaschke, T., Heurich, M., 2004. Object-based semi automatic mapping of forest stands with Laser scanner and Multi-spectral data. Int. Arch. Photogramm. Remote Sens. Spat. Inf. Sci. 36, 328–333.

USDA, Forest Service, 2016. Forest Service Activity Tracking System (FACTs) harvest database. URL http://data.fs.usda.gov/geodata/edw/datasets.php

Varo-Martínez, M.Á., Navarro-Cerrillo, R.M., Hernández-Clemente, R., Duque-Lazo, J., 2017. Semi-automated stand delineation in Mediterranean Pinus sylvestris plantations through segmentation of LiDAR data: The influence of pulse density. Int. J. Appl. Earth Obs. Geoinformation 56, 54–64. https://doi.org/10.1016/j.jag.2016.12.002

Walter, V., 2004. Object-based classification of remote sensing data for change detection. ISPRS J. Photogramm. Remote Sens., Integration of Geodata and Imagery for Automated Refinement and Update of Spatial Databases 58, 225–238. https://doi.org/10.1016/j.isprsjprs.2003.09.007

Weidner, U., 2008. Contribution to the assessment of segmentation quality for remote sensing applications. Int. Arch. Photogramm. Remote Sens. Spat. Inf. Sci. 37, 479–484.

White, J.C., Wulder, M.A., Hermosilla, T., Coops, N.C., Hobart, G.W., 2017. A nationwide annual characterization of 25 years of forest disturbance and recovery for Canada using Landsat time series. Remote Sens. Environ. 194, 303–321. https://doi.org/10.1016/j.rse.2017.03.035

Wu, Z., Heikkinen, V., Hauta-Kasari, M., Parkkinen, J., Tokola, T., 2014. ALS data based forest stand delineation with a coarse-to-fine segmentation approach. IEEE, pp. 547–552. https://doi.org/10.1109/CISP.2014.7003840

Wulder, M.A., White, J.C., Hay, G.J., Castilla, G., 2008. Towards automated segmentation of forest inventory polygons on high spatial resolution satellite imagery. For. Chron. 84, 221–230.

Zhan, Q., Molenaar, M., Tempfli, K., Shi, W., 2005. Quality assessment for geo-spatial objects derived from remotely sensed data. Int. J. Remote Sens. 26, 2953–2974. https://doi.org/10.1080/01431160500057764

Zhang, H., Fritts, J.E., Goldman, S.A., 2008. Image segmentation evaluation: A survey of unsupervised methods. Comput. Vis. Image Underst. 110, 260–280. https://doi.org/10.1016/j.cviu.2007.08.003

Zhang, Y.J., 1997. Evaluation and comparison of different segmentation algorithms. Pattern Recognit. Lett. 18, 963–974. https://doi.org/10.1016/S0167-8655(97)00083-4

Zhang, Y.J., 1996. A survey on evaluation methods for image segmentation. Pattern Recognit. 29, 1335–1346. https://doi.org/10.1016/0031-3203(95)00169-7

Table 1.1. Light Detection and Ranging (LiDAR) summary metrics gridded at 30 m resolution from LiDAR point clouds. Twenty-five metrics are related to vegetation canopy height, and eleven are related to canopy density.

	LiDAR Metrics	Description
Canopy height	‘H01′	1th percentile of height above 1.37 m
	‘H05′	5th percentile of height above 1.37 m
	‘H10′	10th percentile of height above 1.37 m
	‘H20′	20th percentile of height above 1.37 m
	‘H25′	25th percentile of height above 1.37 m
	‘H30′	30th percentile of height above 1.37 m
	‘H40′	40th percentile of height above 1.37 m
	‘H50′	50th percentile of height above 1.37 m
	‘H60′	60th percentile of height above 1.37 m
	‘H70′	70th percentile of height above 1.37 m
	‘H75′	75th percentile of height above 1.37 m
	‘H80′	80th percentile of height above 1.37 m
	‘H90′	90th percentile of height above 1.37 m
	‘H95′	95th percentile of height above 1.37 m
	‘H99′	99th percentile of height above 1.37 m
	‘MaxH’	Maximum height value
	‘AveH’	Mean height value
	‘ModeH’	Modal height value
	‘VarH’	Variance of heights
	‘QMH’	Quadratic mean of heights
	‘SVH’	Standard deviation of heights
	‘CVH’	Coefficient of variation of heights
	‘Skew.H’	Height skewness
	‘IQH’	Interquartile coefficient of heights
	‘CRR’	Canopy relief ratio
Canopy density	‘First returns above mean’	Percentage of first returns above mean height over the total number of first returns
	‘First returns above 1.37 m’	Percentage of first returns above 1.37 m height (breast height) over the total number of first returns
	‘All returns above mean’	Percentage of all returns above the mean height over the total number of returns
	‘All returns above 1.37 m’	Percentage of all returns above 1.37 m (breast height) over the total number of returns
	‘Stratum below 0.15 m’	Percentage of returns below 0.15 m
	‘Stratum 0.15–1.37 m’	Percentage of returns between 0.15 and 1.37 m
	‘Stratum 1.37–5 m’	Percentage of returns between 1.37 and 5 m
	‘Stratum 5–10 m’	Percentage of returns between 5 and 10 m
	‘Stratum 10–20 m’	Percentage of returns between10 and 20 m
	‘Stratum 20–30 m’	Percentage of returns between 20 and 30 m
	‘Stratum above 30 m’	Percentage of returns above 30 m

Table 1.2. LiDAR metrics considered in the analysis. The ‘H95′ and ‘Stratum above 30 m’ metrics were selected based on literature review. From the remaining 34 metrics, the five metrics with absolute average value of the Pearson’s correlation coefficient of the two LiDAR datasets (i.e., Clear Creek and Selway) lower than 0.5 (i.e., |R| < 0.5) with both ‘H95′ and ‘Stratum above 30 m’ were selected.

	Pearson’s Correlation Coefficient (R)					
	Clear Creek		**Selway**		**Average**	
LiDAR Metric	**R(‘HP95′)**	**R(‘Stratum above 30 m’)**	**R(‘HP95′)**	**R(‘Stratum above 30 m’)**	**R(‘HP95′)**	**R(‘Stratum above 30 m’)**
‘HP95′	-	0.81	-	0.76	-	0.79
‘Stratum above 30 m’	0.81	-	0.76	-	0.79	-
‘CVH’	0.05	−0.37	−0.08	−0.54	−0.02	−0.45
‘Stratum below 0.15 m’	−0.26	−0.37	−0.36	−0.43	−0.31	−0.4
‘Stratum 0.15–1.37 m’	−0.28	−0.28	−0.27	−0.55	−0.28	−0.41
‘Stratum 1.37–5 m’	−0.20	−0.23	−0.28	−0.50	−0.24	−0.36
‘Stratum 20–30 m’	0.02	−0.02	−0.05	−0.06	−0.01	−0.04

Table 1.3. Optimal segmentation of the seven considered LiDAR metrics. For each metric, the optimal set of multiresolution segmentation (MRS) algorithm parameters (scale, shape, compactness), the number of resulting image objects, and the unsupervised measures of spatial autocorrelation (normalized Moran's I, normalized weighted Variance, modified Global score) are presented. The two LiDAR datasets were processed independently.

	LiDAR Metric	**Scale**	**Shape**	**Comp.**	**# Image Objects**	MI_{norm}	$wVAr_{norm}$	GS_{mod}
Clear Creek	'H95′	29	0.1	0.1	347	0.47	0.23	0.37
	'CVH'	5	0.1	0.1	11,119	0.55	0.14	0.41
	'Stratum below 0.15 m'	17	0.1	0.5	1295	0.56	0.24	0.43
	'Stratum 0.15–1.37 m'	14	0.1	0.1	1131	0.57	0.24	0.43
	'Stratum 1.37–5 m'	8	0.1	0.9	1495	0.58	0.24	0.44
	'Stratum 20–30 m'	14	0.1	0.1	1439	0.55	0.25	0.43
	'Stratum above 30 m'	59	0.1	0.1	151	0.39	0.35	0.37
Selway	'H95′	26	0.1	0.5	835	0.49	0.22	0.38
	'CVH'	5	0.1	0.1	16,592	0.57	0.14	0.42
	'Stratum below 0.15 m'	20	0.1	0.1	994	0.59	0.25	0.46
	'Stratum 0.15–1.37 m'	14	0.1	0.5	2112	0.55	0.26	0.43
	'Stratum 1.37–5 m'	11	0.1	0.9	2585	0.54	0.26	0.42
	'Stratum 20–30 m'	17	0.1	0.1	1915	0.54	0.28	0.43
	'Stratum above 30 m'	23	0.1	0.1	1511	0.52	0.22	0.40

Table 1.4. Supervised selection of the optimal LiDAR metric. Area-based dissimilarity metrics of oversegmentation (OS), undersegmentation (US), and summary score (D) are presented for the optimal segmentation of the seven considered LiDAR metrics; the number of reference objects with no corresponding image objects is also reported (Nnull). Four scenarios, based on the age of clearcut of the Forest Service Activity Track System (FACTs) harvest reference polygons, are considered: All clearcuts (1956–1996), clearcuts performed before the start of the Landsat MSS record (1956–1972), clearcuts performed before the start of the Landsat TM record (1956–1984), and clearcuts performed after the start of the Landsat TM/ETM+ record (1984–1996). For each scenario, the D score value of the optimal metric is marked (bold and underlined).

		All Clearcuts (1956–1996)				**Pre Landsat (1956- 1972)**				**Pre Landsat TM (1956–1984)**				**Landsat TM (1984–1996)**			
	LiDAR Metric	N_{null}	***OS***	***US***	***D***	N_{null}	***OS***	***US***	***D***	N_{null}	***OS***	***US***	***D***	N_{null}	***OS***	***US***	***D***
Clear Creek	‘H95′	0	0.21	0.37	**0.30**	0	0.15	0.55	**0.40**	0	0.15	0.52	**0.38**	0	0.28	0.20	0.25
	‘CVH’	0	0.86	0.16	0.62	0	0.81	0.19	0.59	0	0.82	0.18	0.60	0	0.90	0.14	0.64
	‘Stratum below 0.15 m’	12	0.53	0.47	0.50	4	0.55	0.52	0.53	5	0.55	0.51	0.53	7	0.52	0.43	0.48
	‘Stratum 0.15–1.37 m’	11	0.53	0.49	0.51	5	0.52	0.56	0.54	8	0.54	0.57	0.55	3	0.51	0.41	0.46
	‘Stratum 1.37–5 m’	8	0.44	0.52	0.48	4	0.46	0.56	0.51	6	0.47	0.56	0.52	2	0.40	0.47	0.43
	‘Stratum 20–30 m’	7	0.44	0.27	0.36	4	0.61	0.32	0.49	6	0.62	0.33	0.50	1	0.24	0.20	**0.22**
	‘Stratum above 30 m’	2	0.12	0.80	0.57	2	0.14	0.80	0.57	2	0.13	0.76	0.54	0	0.10	0.85	0.61
Selway	‘H95′	0	0.22	0.21	**0.22**	0	0.13	0.32	**0.24**	0	0.16	0.29	**0.24**	0	0.28	0.14	**0.22**
	‘CVH’	1	0.87	0.17	0.63	1	0.88	0.17	0.63	1	0.85	0.18	0.62	0	0.89	0.16	0.64
	‘Stratum below 0.15 m’	15	0.45	0.62	0.54	6	0.58	0.50	0.54	8	0.56	0.53	0.55	7	0.36	0.69	0.55
	‘Stratum 0.15–1.37 m’	9	0.44	0.46	0.45	1	0.54	0.45	0.50	4	0.52	0.49	0.51	5	0.37	0.43	0.40
	‘Stratum 1.37–5 m’	9	0.44	0.38	0.41	6	0.57	0.47	0.52	7	0.56	0.46	0.51	2	0.34	0.30	0.32
	‘Stratum 20–30 m’	4	0.39	0.28	0.34	0	0.62	0.19	0.46	4	0.56	0.28	0.45	0	0.23	0.28	0.26
	‘Stratum above 30 m’	1	0.19	0.31	0.26	1	0.17	0.35	0.28	1	0.19	0.33	0.27	0	0.19	0.29	0.24

Table 1.5. Area-based dissimilarity metrics calculated from the validation dataset presented in Figure 1.10: Oversegmentation (OS), undersegmentation (US), summary score (D), modified oversegmentation (OS^*), modified undersegmentation (US^*), and summary score (D^*).

Area	Stands	OS	US	D	OS^*	US^*	D^*
Clear Creek	All	0.25	0.26	0.26	0.18	0.27	0.23
	UAF	0.39	0.35	0.37	0.24	0.37	0.31
	EAF	0.12	0.18	0.15	0.12	0.18	0.15
Selway	All	0.36	0.15	0.27	0.21	0.14	0.18
	UAF	0.50	0.21	0.39	0.22	0.21	0.21
	EAF	0.22	0.08	0.16	0.20	0.08	0.15

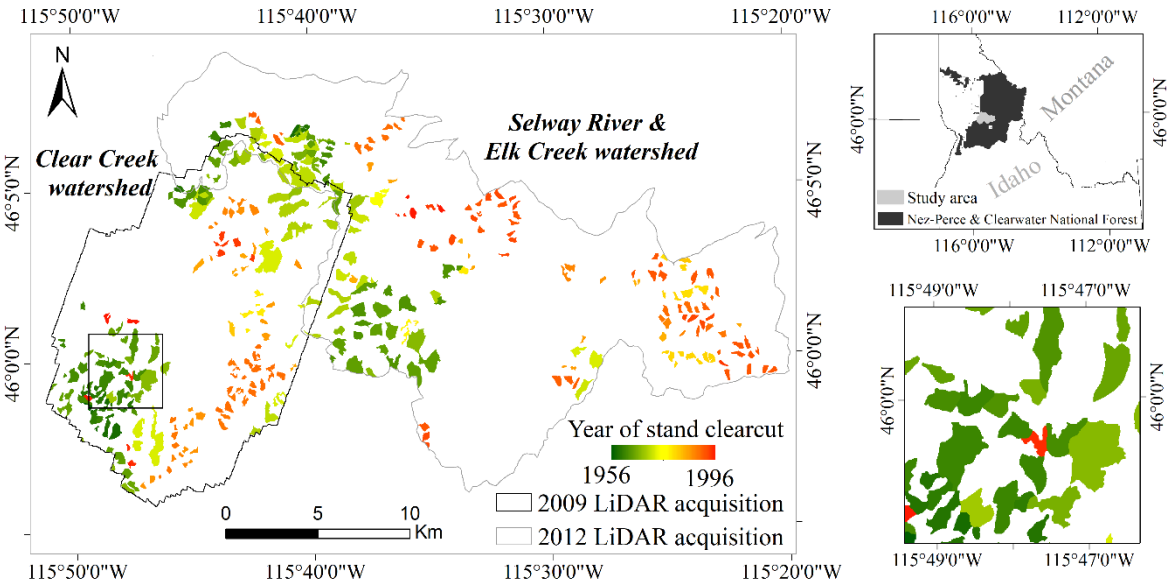

Figure 1.1. Location of the study area in the Nez-Perce & Clearwater National Forest (Idaho-USA); boundaries of the 2009 and 2012 Light Detection and Ranging (LiDAR) acquisitions; and reference polygons of historical stand clearcuts (>2 ha) from the Forest Service Activity Track System (FACTs) harvest dataset. The FACTs polygons are displayed with a rainbow color scale indicating the year of harvest, from 1956 to 1996. No data are available for clearcuts performed before 1956; no clearcuts (>2 ha) were reported from 1996 to the LiDAR acquisition dates. On the bottom right, a 4 × 4 km subset of the Clear Creek watershed.

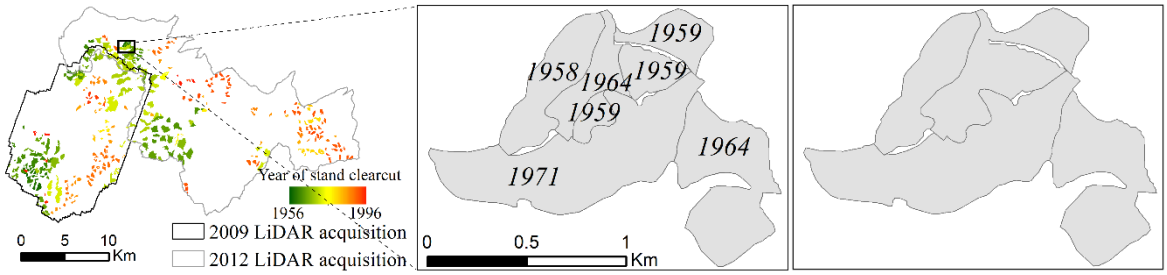

Figure 1.2. Example of pre-processing of the FACTs harvest polygons. Adjacent polygons harvested within a time interval ≤5 years (left) are merged into aggregated polygons (right) that are used as reference objects in all the subsequent steps of the analysis.

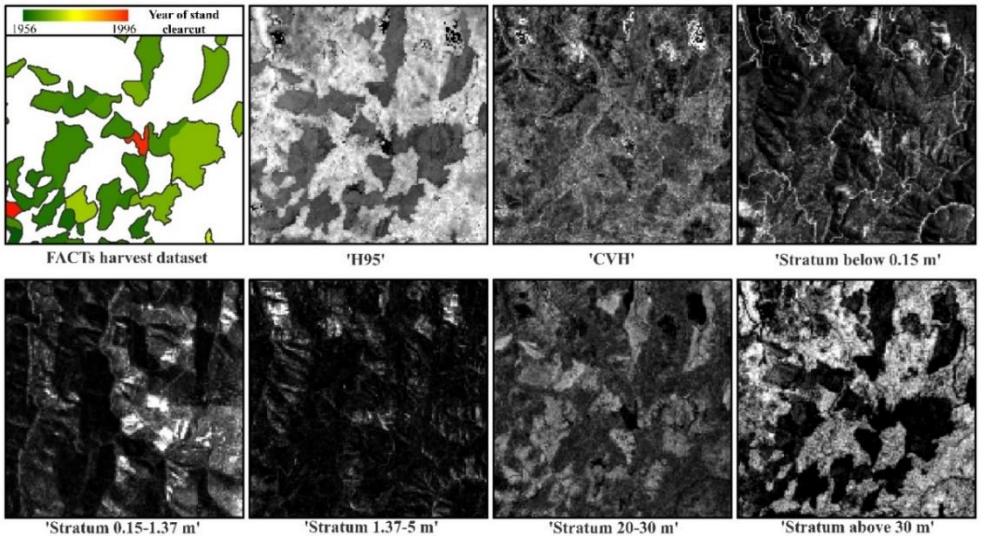

Figure 1.3. The seven LiDAR metrics considered in the analysis (Table 1.2), displayed with a linear black to white grayscale color table (1% linear stretch), on a 4 × 4 km subset of the Clear Creek watershed (location on Figure 1.1). The FACTs harvest reference dataset is presented for comparison in the upper left, to highlight the different response of each metric to even-aged forest stands.

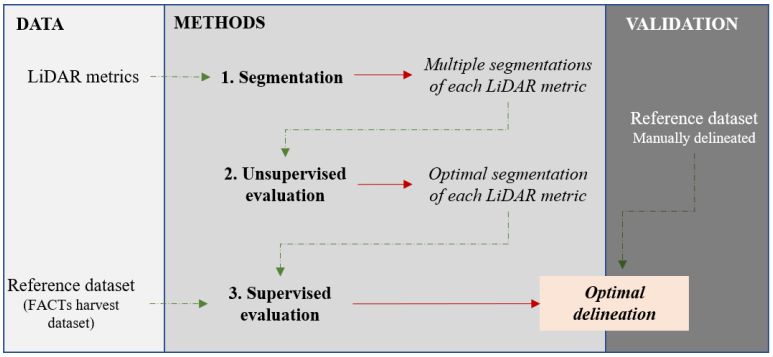

Figure 1.4. Flowchart of the proposed methodology for forest stand delineation based on a two-stage evaluation strategy.

Figure 1.5. Illustration of the area-based dissimilarity metrics (OS_i, US_i, D_i), and of the modified metrics (OS_i^*, US_i^*, D_i^*). A reference object x_i, (black vectors) is displayed together with its corresponding set of image objects (gray vectors): The top row shows an example where the reference object is oversegmented, but not undersegmented (i.e., it is closely matched by the union area $\bigcup_{y_j \in Y_i^*} y_j$); the bottom row shows an example where the reference object is both oversegmented, and undersegmented. The center column illustrates the traditional oversegmentation (OS_i), undersegmentation (US_i) and summary score D_i for that single reference object, metrics that consider each individual corresponding image object. The right column illustrates the modified OS_i^*, US_i^*, and D_i^* metrics, that consider instead the union area of all corresponding image objects. The summary score D does not report a significant difference between the two classifications (top: D_i= 0.59, bottom: D_i= 0.61), whereas the modified summary score D* indicates that through post-processing the top row segmentation could result in a near-perfect match with the reference object (D_i^*= 0.04), whereas significant errors will remain in the bottom row segmentation (D_i^*= 0.29).

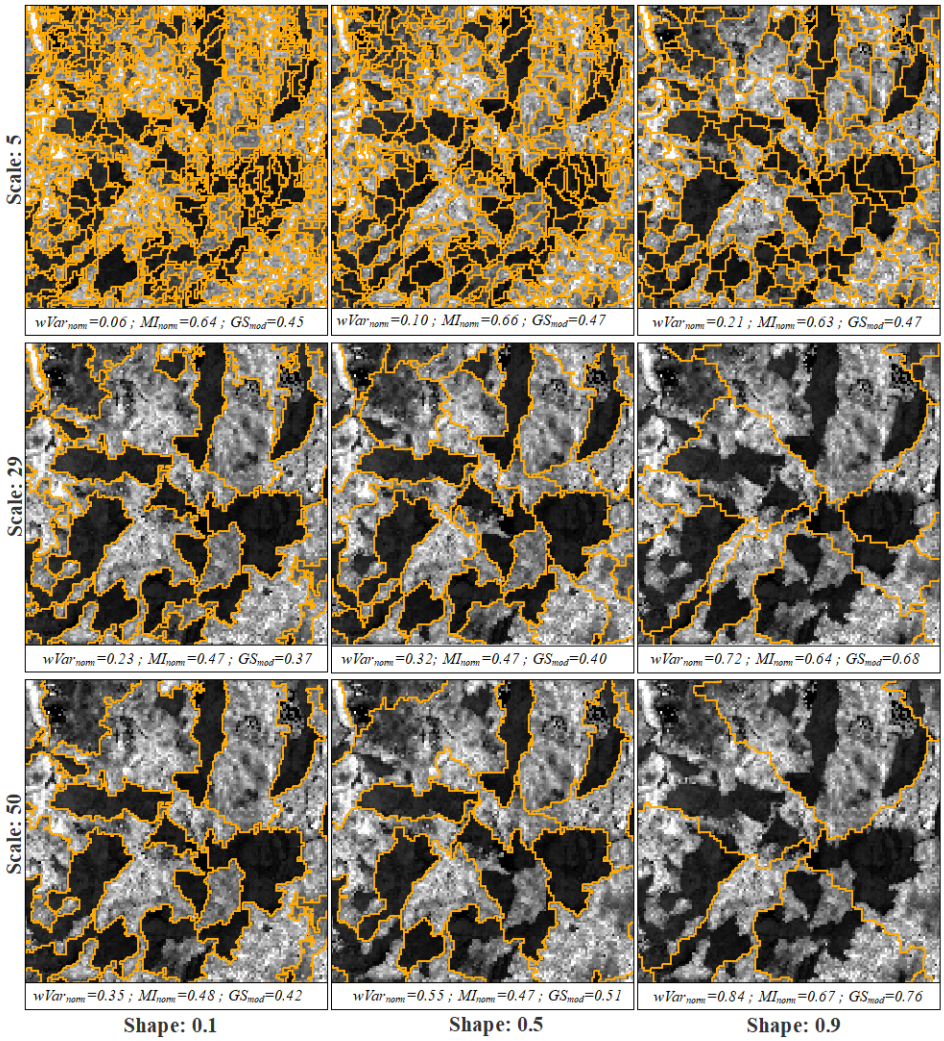

Figure 1.6. Segmentations of the 'H95′ LiDAR metric generated by the multiresolution segmentation (MRS) algorithm with different combinations of the scale and shape parameters, and the same compactness parameter (Comp. = 0.1). In all cases, the segmentation is displayed as orange vectors overlaid on the 'H95′ metric raster, shown in grayscale. The same 4 × 4 km area of Figure 1.1 is presented.

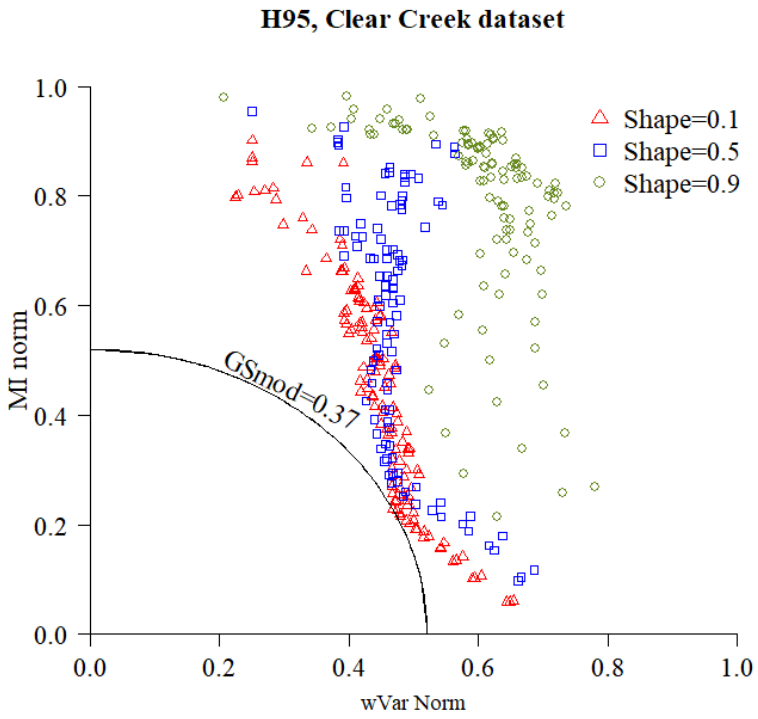

Figure 1.7. Scatter-plot of the normalized weighted variance ($wVar_{norm}$) and normalized Moran's Index (MI_{norm}) of the segmentations of the 'H95′ metric for the Clear Creek dataset, generated by different sets of the MRS algorithm parameters. The two metrics are combined in a quadratic Global Score (GS_{mod}) and the segmentation with the lowest GS_{mod} is selected as the optimal segmentation.

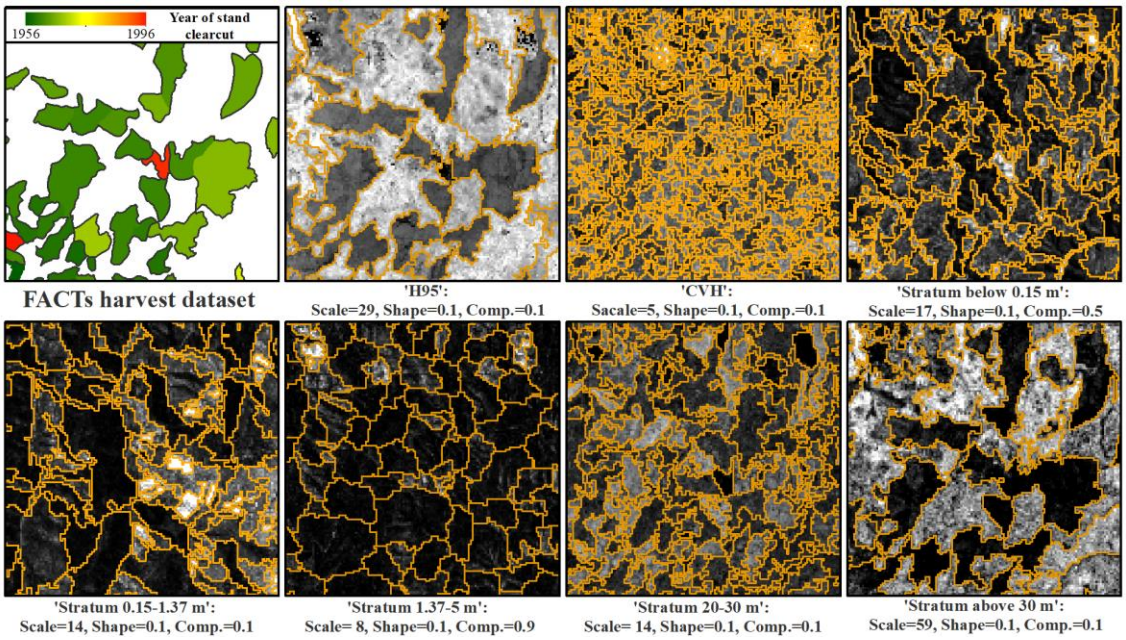

Figure 1.8. Optimal segmentation of the seven considered LiDAR metrics, shown for the same 4 × 4 km subset of Figure 1.1. The FACTS harvest reference dataset is shown at the upper left for comparison.

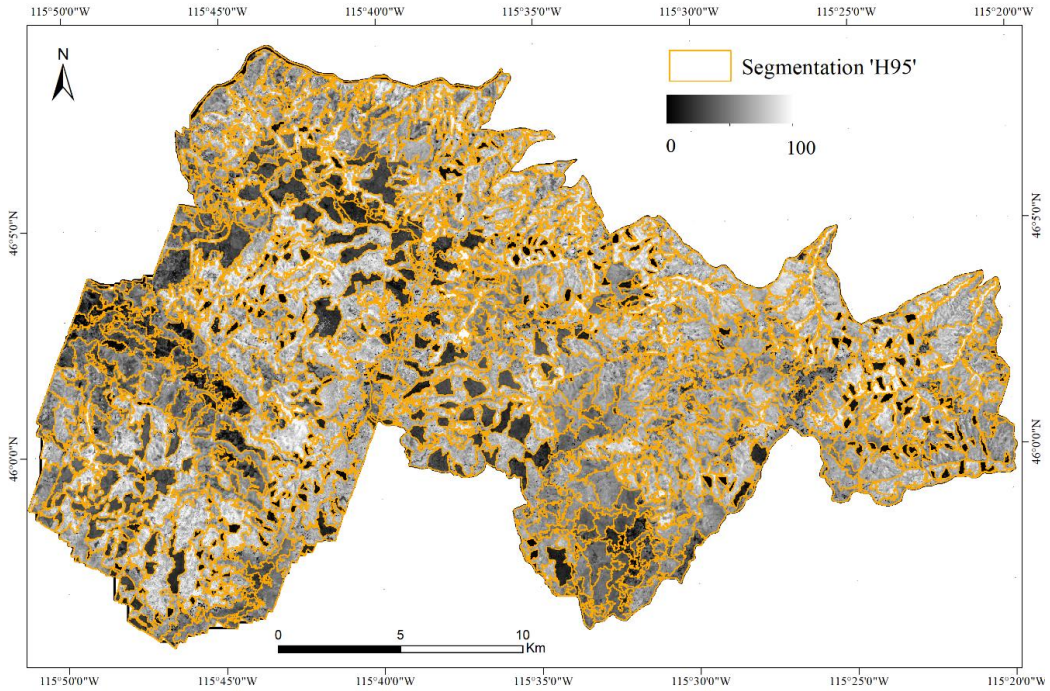

Figure 1.9. Optimal segmentation of the optimal ‘H95′ metric (orange vector, overlaid on the ‘H95′ shown in grayscale). Visual comparison with the FACTs dataset (Figure 1.2) indicates a good correspondence between even-aged forest stands and image objects.

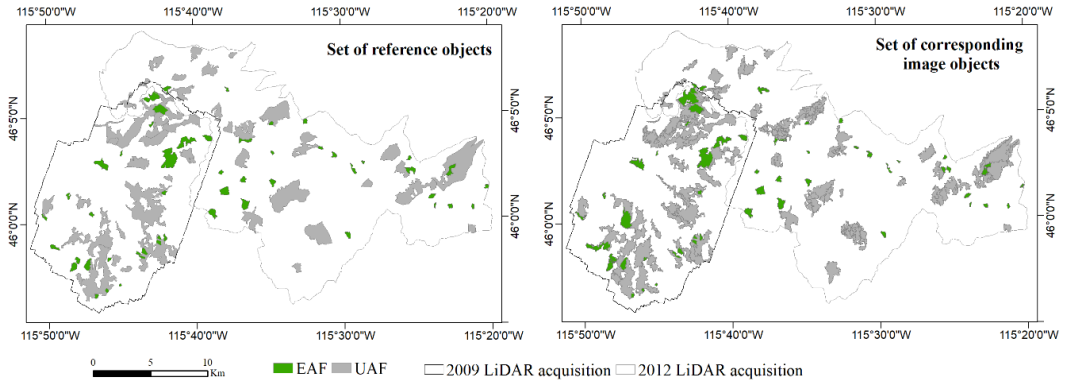

Figure 1.10. Validation dataset: Reference objects delineated through visual interpretation of NAIP imagery and LiDAR point clouds (left); and corresponding image objects of the optimal segmentation of the 'H95′ LiDAR metric (right). Even-aged forest stand (EAF) reference objects and their corresponding image objects are shown in green, and uneven-aged forest stand (UAF) reference objects and their corresponding image objects are shown in gray. A total of 100 reference objects were generated through visual interpretation of NAIP imagery and LiDAR point clouds: 25 EAF (average area: ~23 ha) and 25 UAF (average area: ~158 ha) on each LiDAR dataset.

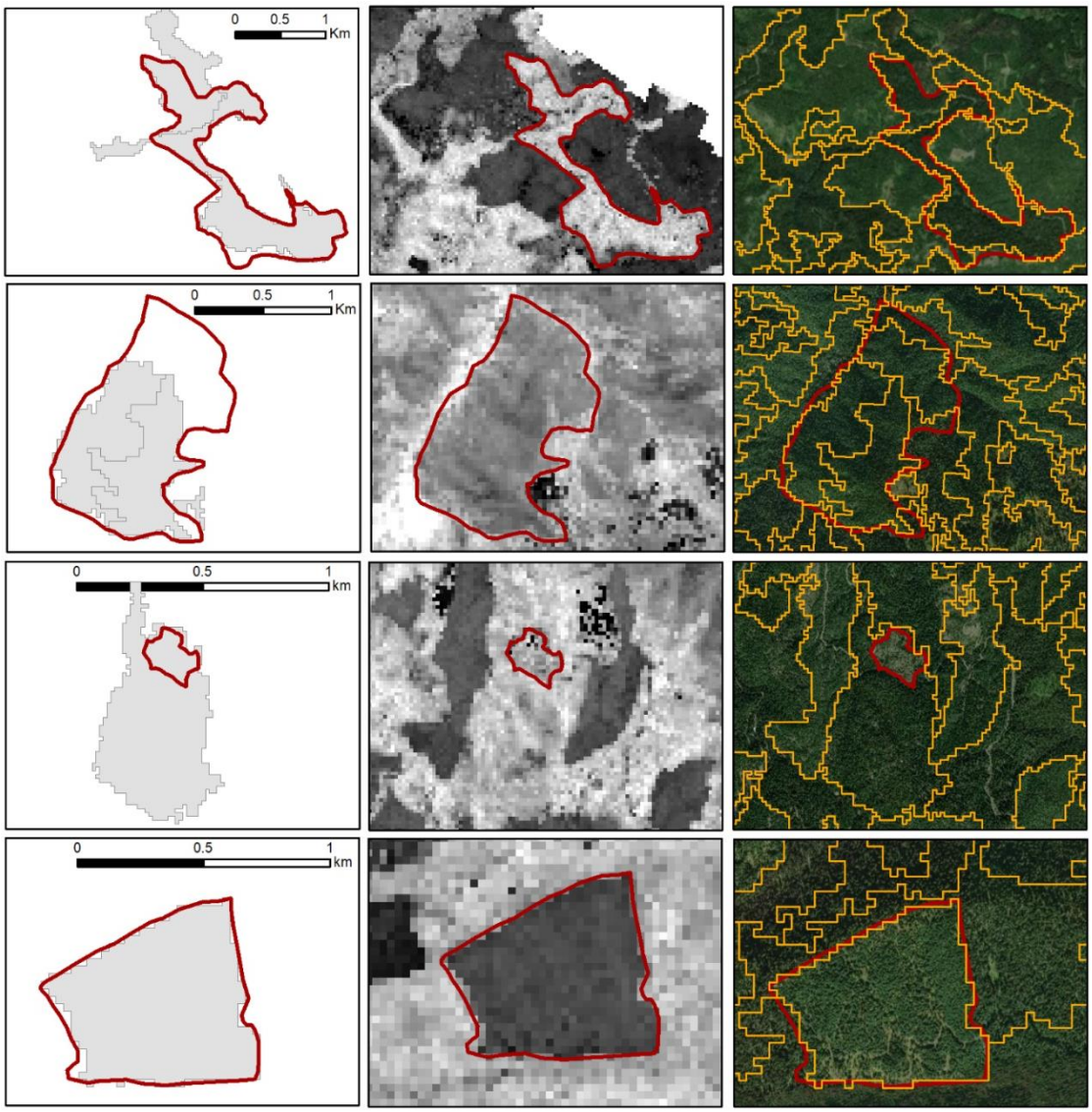

Figure 1.11. Illustrative examples of the spatial relationship between visually interpreted reference objects and corresponding image objects of the optimal segmentation of the 'H95′ LiDAR metric. The two top rows present examples of uneven-aged forest stands (UAF), and the two bottom rows present examples of even-aged forest stands (EAF). Left column: Reference objects (red polygons) and set of the corresponding image objects (gray polygons). Center column: Reference objects overlaid on the 'H95′ LiDAR metric shown in grayscale. Right column: Reference object and all image objects (orange polygons) overlaid on 1 m spatial resolution NAIP imagery used to generate the validation dataset, shown in true color.

Chapter 2: Reconstruction of the disturbance history of a temperate coniferous forest through stand-level analysis of airborne LiDAR data.

Under review in *Forestry An international journal of forest research*

Abstract

Spatially explicit information about stand-level Time Since the last stand-replacing Disturbance (TSD) is fundamental for modelling many forest ecosystem processes, but most of the current satellite remote sensing mapping approaches are based on change detection and time series analysis, and can detect only disturbances that have occurred since the start of the optical satellite data record. The spatial legacy of stand-replacing disturbances can however persist on the landscape for several decades to centuries, in the form of distinct horizontal and vertical stand structure features. We propose a new approach to reconstruct the long-term disturbance history of a forest, estimating TSD through stand-level analysis of LiDAR data, which are highly sensitive to the three-dimensional forest canopy structure. The study area is in the Nez Perce-Clearwater National Forest in north-central Idaho, where airborne LiDAR covering about 52,000 ha and ancillary TSD reference data for a period of more than 140 years were available. The root mean square difference (RSMD) between predicted and reference TSD was 17.5 years with a BIAS of 0.8 years; and on 72.8% of the stands the predicted TSD was less than 10 years apart from the reference TSD (78.2% of the stands when considering only disturbances occurred in the last 100 years). The results demonstrate that airborne LiDAR-derived data have enough explanatory power to reconstruct the long-term, stand-replacing disturbance history of temperate forested areas at regional scales.

Introduction

Stand-replacing disturbances are a key component of forest ecosystem dynamics (Oliver and Larson, 1996) driving forest structure, function, and composition (Franklin et al., 2002; Oliver, 1980). Maps of the long-term disturbance history of a forest would improve estimates of historic, current, and potential carbon sequestration (Bradford et al., 2008; Chapin III et al., 2002; Pan et al., 2011), reduce uncertainties in the carbon budget (Frolking et al., 2009), and contribute to a better understanding of disturbance causes and consequences (Cohen et al., 2002).

A stand-replacing (major) disturbance is a mortality event (e.g., clearcut, fire, insect outbreak) that frees up growing space and leads to complete replacement of the trees of an entire forest stand, so that post-disturbance regeneration is characterized by competition between a cohort of new trees (Oliver, 1980; Oliver and Larson, 1996). Anthropogenic and natural stand-replacing disturbances result therefore in a patchy and heterogeneous landscape of even-aged forest stands, which are structurally distinct from each other based on their successional state. Long-term stand-replacing disturbance

legacies on forested land can persist on the landscape for decades to centuries (Turner, 2010), depending on the forest type. Tree height, canopy density and, more generally, the forest structure are illustrative of these legacies (Spies, 1998), especially in even-aged stands where forest structure is driven by age (Pflugmacher et al., 2012).

Traditional approaches to map forest disturbances at regional scales with remotely sensed data have mostly relied on time series analysis of optical data. While single image analysis has limited applications because the persistence of stand-replacing disturbance spectral signatures is limited depending on vegetation recovery rates (Healey et al., 2005; Lunetta et al., 2004), and the spectral response of vegetation in optical wavelengths saturates in closed canopy forest (Cohen et al., 1995; Spanner et al., 1990; Turner et al., 1999), it is widely established that time series of Earth Observation satellite data can be used to systematically detect forest disturbances at a variety of spatial scales (Cohen and Goward, 2004; Hansen et al., 2013). With particular regard to multispectral, moderate resolution data such as those provided by the Landsat satellite series, the detection and characterization of disturbances involves the detection of spectral changes in a time series of observation to detect discontinuities (to capture abrupt events) and/or trends (to capture slower processes) (Hansen et al., 2008; Hayes and Sader, 2001; Huang et al., 2009; Huo et al., 2019; Kennedy et al., 2010; Lu et al., 2004; Masek et al., 2008; Schroeder et al., 2011). The main limitation of this approach is that it is necessarily limited to mapping disturbances that have occurred within the temporal extent of the available optical satellite record; at the earliest, 1972 when Landsat-1 was launched with the 60 m resolution Multi-Spectral Scanner (MSS). The disturbance history of a forest mapped with these approaches, being limited to at most 50 years, is necessarily incomplete in ecosystems where stands may require up to 100 years to mature (Bonnell et al., 2011; Fu et al., 2017; Liebsch et al., 2008). It should also be noted that, while the Landsat archive is largely complete in the United States, in many other parts of the World it is extremely fragmentary until the availability of Landsat-7 in 1999 (Wulder et al., 2016).

A second limitation of these approaches is that the change detection is generally conducted for each pixel independently, without considering the spatial relationship between neighbouring raster cells of the same forest stand. Pixel based change detection algorithms are prone to generate noisy outputs, i.e. isolated pixels spuriously labelled as change in the middle of non-change area, and vice versa (Radke et al., 2005). Object-based approaches, conversely, use image objects (a discrete region composed by a group of cells internally coherent and different from the surroundings (Blaschke et al., 2008) as the basic spatial unit of analysis. The cell by itself doesn’t represent a true geographical feature (Fisher, 1997), but the image object does represent a geographical feature of interest that is also

internally coherent and different from the surroundings. Forest stands can be detected as image objects: object-based analysis has been used to identify and describe forest disturbances (see Chen et al., 2012; Hussain et al., 2013). While studies to identify forest disturbances are still mostly multi-temporal, the potential to use object-based analysis on single date datasets to characterize TSD at the stand-level has occasionally been shown in the literature. Wulder et al. (2004), for instance, applied object-based analysis to Landsat ETM+ imagery to estimate forest stand age from an approximate time since disturbance to 20 years after harvest. They relied on optical image-derived metrics sensitive to vegetation structure, such as the Tasselled Cap indices, for the predictions, and an object-based analysis to provide a contextual frame of analysis and neglect anomalous cells through different regeneration stages. Their results had an associated estimation error of less than 2.5 years, but the time span of the analysis was relatively small (20 years).

Alternatively, few studies have proposed to use remotely sensed data of the three-dimensional structure of the forest canopy to map forest stand age. Véga and St-Onge (2009), for instance, mapped age and site index of jack pine using known age-height curves and time series of canopy height models derived from aerial photographs. Racine et al. (2014) estimated forest age in a managed boreal forest using predictors derived from Light Detection and Ranging (LiDAR) data in 158 field plot locations. This study showed the strong linkage between LiDAR predictor variables, especially LiDAR-derived height, and plot age. In Zhang et al. (2014), stand age was mapped across different forest types in China (at 1 km spatial resolution) using biomass estimates derived from canopy height maps (Simard et al., 2011). More recently, Vastaranta et al. (2016) used time series of image-based digital surface models (DSM) and canopy height models (CHM) to classify forest stand age. All these studies obtained relatively good results, exploiting the strong relationship between forest age and canopy structure. This relationship is particularly significant in the first decades after a stand replacing disturbance, before the height distribution of trees in a mature stand becomes uneven.

In this study, we characterize the stand age of a forest in terms of time since the last stand-replacing disturbance (TSD). We hypothesize that remotely sensed data capturing the three-dimensional structure of the vegetation (i.e., Light Detection and Ranging (LiDAR)) is suitable for the long-term estimation of TSD, beyond the timeframe of the available optical remote sensing data record, thus complementing the traditional time-series based TSD mapping approaches. We developed a stand-level, object-based approach to estimate TSD from single-image LiDAR metrics, and we compared the results to independent reference data to assess the accuracy of the prediction.

Materials

Study area

The study area is a temperate mixed-conifer forest located within the Nez Perce-Clearwater National Forest in Idaho (USA), covering 52,257 ha in the Clear Creek, Selway River, and Elk Creek watersheds (Figure 2.1). Dominant tree species are Douglas-fir (Pseudotsuga menziesii) and grand fir (Abies grandis), but other species such as western redcedar (Thuja plicata) and ponderosa pine (Pinus ponderosa) are also common.

The combination of anthropogenic and natural stand-replacing disturbances has generated a patchy landscape of even-aged forest stands. Historical records describe large-scale wildfires happening in this area since the decade of 1870 (Morgan et al., 2017; USDA, Forest Service, 2016); of particular relevance are 1919 and 1931 fires that affected respectively ~12,000 and 3,500 ha (i.e., ~23.0% and 6.7% of the study area). Additionally, timber harvest was common since early in the twentieth century. Logging activity peaked during the 1960s and 1970s, with clearcuts and shelterwoods being the most prevalent harvest practices (Cochrell, 1960; Space, 1964; USDA, Forest Service, 2016).

LiDAR Datasets and Data Pre-Processing

Airborne LiDAR data were acquired in 2009 on the Clear Creek watershed and in 2012 on the Selway River and Elk Creek watersheds (Figure 2.1, Table 2.1). Point clouds in a binary format (.las) and a digital terrain model (DTM) interpolated from the ground returns at 1-meter spatial resolution were delivered by the provider. The TerraScan software (TerraSolid Ltd, Helsinki, Finland) was used by the vendors to classify ground returns in the point cloud and to interpolate the terrain model. The average pulse density was at least 4 points/m^2 in both flights, and the point cloud was converted to height above ground using the DTM. The LiDAR point cloud was subsequently rasterized, and gridded summary metrics (i.e., statistics summarizing the LiDAR point cloud for a specific cell size) were calculated using the FUSION software (McGaughey, 2009).

A total of 21 metrics were generated at 30 m resolution (Table 2.2): 15 LiDAR canopy metrics (6 related to vegetation canopy height and complexity, and 9 related to canopy density) and 6 topographic metrics. Echoes below 1.37 m above the terrain were ignored to compute vegetation canopy height metrics, assuming that most of them stemmed from ground or understory. If no echoes were found within the 30 m x 30 m grid cell, then that cell was given a value of zero. Canopy height metrics include the average, 5^{th}, 25^{th}, 75^{th} and 95^{th} percentile the distribution of return height within the cell, and are complemented by the rumple index, which is a measure of canopy complexity. It is defined as the ratio of canopy surface area over the underlying ground surface area (Kane et al., 2010; Parker et al., 2004) and, unlike the rest of metrics, it was retrieved from a 1-m canopy height model (CHM) and the

"GridSurfaceStats" tool within the FUSION software. Canopy density metrics include the percentage of LiDAR returns for different vertical strata of the forest canopy. Additionally, six topographic metrics of elevation, slope, solar radiation index and aspect were derived from the DTM. Aspect in particular is characterized through three transformed metrics: the 'SRAI' (Solar-Radiation Aspect Index) is a linear transformation of the topographic aspect (Roberts and Cooper, 1989); the cosine ('SCA') and the sine ('SSA') aspect transformations account for the interaction between aspect and slope, considered of importance for tree growth (Stage, 1976).

The overlap area between the two datasets covers 1,271 ha (Figure 2.1). Since no significant disturbances occurred in the overlap area between the two LiDAR acquisition dates, the cells of the overlapping area were used to assess the mean growth increment between 2009 and 2012 on the canopy height metrics. Having thus harmonized the height metrics by adding to the 2009 dataset the observed mean growth, both LiDAR datasets were mosaicked together to obtain single raster, with metrics nominally reported to 2012, that was used as the reference year in all subsequent steps of the analysis. We note that the mean difference between the two acquisitions was relatively modest (0.07 m, 0.08 m, 0.10 m, 0.03 m, and 0.21 m for 'H.Ave', 'H05', 'H25', 'H75' and 'H95' respectively) as expected due to the fact that only two complete growing seasons separate the two LiDAR acquisitions (Hopkinson et al., 2008; Hudak et al., 2012).

Forest Stand Map

A map of forest stands was used to provide the spatial units of analysis for TSD estimation. It was generated following the object-based strategy presented in Sanchez-Lopez et al. (2018), and based on the segmentation of the 'H95' metric, identified as the optimal LiDAR metric for the delineation of even-aged forest stands (Sanchez-Lopez et al., 2018).

The 30 m raster of the 'H95' metric was systematically segmented with different sets of parameters of the multiresolution segmentation (MRS) algorithm (Baatz and Schape, 2000) implemented in eCognition software. Measures of spatial autocorrelation (Böck et al., 2017; Espindola et al., 2006; Johnson and Xie, 2011) were used to evaluate the resulting set of segmentations, and the segmentation with the maximum degree of intra-segment homogeneity and inter-segment heterogeneity was selected as the optimal stand map. For a complete description of the workflow refer to Sanchez-Lopez et al. (2018).

The selected segmentation (i.e., the selected forest stand map) was composed of 1470 image objects (hereafter referred as forest stands) with an average size of 35.6 ha, and median size of 29 ha (Figure 2.2).

Ancillary Reference Data and Pre-Processing

The FACTS (Forest ACtivity Tracking System) timber harvest dataset (USDA, Forest Service, 2016) was used to locate stand-replacing harvests since 1956. The FACTS dataset is maintained by the U.S. Forest Service and contains polygon features representing forest management units, generally forest stands or forest patches, with an indication of the year in which timber management activities (e.g., clearcut, shelterwood, thinning) were executed. All the stand and patch clearcut management units in the FACTS harvest data record for the study area were initially considered, corresponding to 6,200 ha logged between 1956 and 2005. No logging was reported in the area from 2005 to the LiDAR acquisition date.

Additionally, a dataset of burned area perimeters of wildfires from 1870 to 2000 (Morgan et al., 2017) was used as a reference dataset for fire disturbance. The burned area perimeters were interpreted by an expert ecologist from fire atlas records and historical aerial photographs when available. The dataset also defines burn severity classes (unburned, low, moderate and high), based on percent of tree mortality of the overstory, visually delineated by the same interpreter within each fire perimeter (Morgan et al., 2017). High and moderate severity burns were considered in our study as stand-replacing disturbance events totaling 22,395 ha, 99.95% of which (i.e., ~22,384 ha) were disturbed between 1870 and 1940, and the remaining 0.05% (i.e. ~11 ha) were disturbed in 1992.

Time since disturbance (TSD) was computed for all reference data using 2012, i.e. the acquisition date of the second LiDAR dataset, as reference year; consequently, the disturbances present in the reference dataset had TSD ranging from 7 (stands disturbed in 2005) to 142 (stands disturbed in 1870).

The ancillary reference dataset assembled from the FACTs harvests and the historical burns was manually refined: post-disturbances (i.e., small areas with evident biomass removal or other post-logging activity, especially within the fire perimeters) and bare ground areas were manually digitized through visual interpretation of the 2011 National Agricultural Imagery Program (NAIP) imagery (1 m spatial resolution) and the LiDAR data, then erased from the compiled disturbance reference dataset. Additionally, three polygons reported as clearcuts in the 1950s were removed from the dataset since no evidence of actual harvest could be observed. Neighboring forest management units harvested in consecutive years showed small differences in their structure due to low growth of vegetation during consecutive cuts and were considered as part of the same forest stand. Thus, following the procedure introduced in Sanchez-Lopez et al. (2018), units sharing borders and harvested within a short time interval (≤5 years) were merged as exemplified in Figure 2.3, top row. The year of harvest assigned to each aggregated forest stand was calculated as the weighted average of the merged management units accounting for the relative area of each of the integrating stands. Figure 2.1 shows the location and TSD

of the stand-replacing disturbances, compiled from the FACTS dataset and the burned area perimeters, and pre-processed as described above.

Further pre-processing was needed to match the ancillary dataset with the forest stand map. As exemplified in Figure 2.3, bottom row, there is a degree of mismatching between the perimeters of the ancillary reference dataset and the forest stand perimeters, due to the different processing methodologies (i.e. photointerpretation for the reference datasets, semiautomatic image segmentation for the stand map) and data sources (historical records and aerial photographs for the reference datasets, LiDAR for the stand map). To reconcile the two datasets, we defined as "Forest stands with known TSD" the segmented forest stands whose area overlapped by at least 50% with the area of the ancillary reference data polygons defined above. The 50% area criterion is commonly used in the GEOBIA literature for matching objects across datasets (Clinton et al., 2010; Drăguţ et al., 2014; Liu et al., 2012; Zhan et al., 2005). The histogram of the overlapping area between the forest stands and the ancillary dataset (Figure 2.4) shows that there is generally a good agreement between the two datasets: only 26% of the forest overlap less than 75% with the reference dataset, and among these, 78% correspond to old fires.

Additionally, 50 undisturbed forest stands, covering a total area of 2,121 ha, were visually identified overlaying the 1-meter spatial resolution NAIP imagery, the rasterized LiDAR metrics (Table 2.2), and the ancillary reference dataset. These forest stands were mainly characterized by high height of the dominant cohort of the forest canopy, for instance, the mean 'H95' was 43.7 m, while the mean 'H95' of the stands disturbed in 1870 and 1880 was 36.3 and 34.1 m respectively. Thus, they were considered non-disturbed since 1870 (i.e., TSD greater than 142 years) and were added to the reference dataset, to ensure that it represented all the stand types within the study area.

Figure 2.4 shows the 781 (731 disturbed and 50 non-disturbed) forest stands (26,644 ha) which, hereafter, are all considered forest stands with known TSD, and Table 2.3 summarizes accordingly the disturbed area by decade of both the ancillary reference dataset and the forest stands with known TSD.

Methods

A disturbance history map was obtained using a Random Forest (RF) classifier (Breiman, 2001) to impute TSD over a period of 142 years. The methodology involved four main steps (Figure 2.5): (1) training stand data selection following a LiDAR-assisted stratification strategy; (2) TSD estimation; first, at the cell-level imputing TSD from RF with LiDAR metrics as predictor variables; and second, at the stand-level using the perimeters of the stands to calculate median TSD from the cell-level

imputations; (3) accuracy assessment using the stands with known TSD as reference (Figure 2.4); and (4) sensitivity analysis of the stratification strategy and the sample size of the training data.

Training Dataset

A training set of stands with known TSD (Figure 2.4) was extracted through stratified random sampling. A stratification based on topography ('SRAI') and canopy height ('H95') was used to ensure the representativeness of the training set. Previous studies have demonstrated that LiDAR-assisted plot stratification of LiDAR-based forest inventories is cost-effective to reduce the number of field plots required for model calibration compared to simple random sampling (Gobakken et al., 2013; Hawbaker et al., 2009).

The transformed solar-radiation aspect index ('SRAI', Table 2.2), was selected as the first metric. 'SRAI' ranges between 0 and 1, where areas with values close to 0 are north-northeast oriented, i.e., cooler and moistier; and areas with values close to 1 are south-shouthwest oriented, i.e., warmer and drier. Considering the strong linkage between canopy height and age (Racine et al., 2014), the choice was made to have one of the height metrics as the second stratification metric. To select the metric among the five canopy height metrics listed in Table 2.2, Pairwise Pearson correlations coefficients (R) were calculated between TSD and mean value of each canopy metric based on all the stands with known TSD (i.e., the stands reported in Figure 2.4). The 'H95' metric resulted in highest correlation (R=0.89) and was selected as the second stratification metric.

A hierarchical, two level stratification approach was used. Two 'SRAI' strata (high 'SRAI' / low 'SRAI') of equal size were defined, using the median of the stand-level SRAI as threshold. Within each 'SRAI' stratum, five 'H95' canopy height strata (based on the mean 'H95' per stand) were defined, using the quintiles of the 'H95' distribution. As a result, ten strata of equal size were identified (Figure 2.6).

The training dataset was selected by extracting randomly five forest stands from each of the 10 strata (50 stands). Additionally, the three forest stands with the lowest and the three forest stands with highest 'H95' (i.e., 6 forest stands) were added to the training dataset to ensure that the full dynamic range of canopy heights was represented, which is particularly relevant for using RF classifiers since decision trees can't effectively extrapolate results out of the range of the training dataset (Zimmerman et al., 2018). The resulting training dataset included 56 stands, as reported in Figure 2.6.

TSD Estimation

A stand-level map of estimated TSD was obtained in two steps. First, TSD for each 30 m raster cell was imputed through the RF; TSD at the stand-level was subsequently obtained as the median value of the cell-level imputations within each forest stand (Figure 2.2).

The raster cells within the 56 training forest stands were used to train the RF classifier; the TSD as determined by the reference dataset was used as the dependent (response) variable, and all the LiDAR metrics as independent (predictor) variables. RF is relatively insensitive to outliers and data noise, but errors in the predictions might increase exponentially if a 20% noise threshold is reached (Rodriguez-Galiano et al., 2012). Consequently, outliers were removed from the training data by removing the individual cells with 'H95' below the 5^{th} or above the 95^{th} percentiles of the distribution of each stand. Outliers in the study area are primarily due to old stands where the uneven-aged distribution of the canopy is reached and the likelihood to encounter gaps with young trees due to tree mortality increases (Runkle, 1982); to stands recently harvested where some old standing trees are left for seedling and are not representative of TSD; and to cells at the edge of the stands in cases where there is a significant border effect.

The 56 training objects identified a total of 17,604 cell observations used to train the RF model. These cells represented ~1,584 ha, i.e., 3.0% of the study area. Disturbances were unequally distributed over time (Table 2.3, Figure 2.1) as reflected in the number of training stands per disturbance decade (Table 2.4).

The yai function implemented on the yaImpute R package (Crookston and Finley, 2008) was used to train the RF classifier. The number of decision trees was set at 500 and the number of LiDAR variables available to split at each tree node at the default value, i.e., as the square root of the number of predictor variables. The Out-of-Bag (OOB) error estimate of the RF was calculated. As defined here, RF randomly sampled two thirds of the available training observations to build each of the 500 decision trees. A predicted error is then obtained using the defined tree on the Out-Of-Bag (i.e., non-included) portion of the training data. The average of the predicted errors of all the trees is the OOB error estimate.

The AsciiGridImpute function on the yaImpute R package was used to impute TSD at the raster cell-level over the whole study area; and TSD at the stand-level was then calculated as the median of all the TSD cell values enclosed within the perimeters of each forest stand.

Accuracy Assessment

The forest stands with known TSD (Figure 2.4) and not used to train the RF were used as reference data to assess the accuracy of the TSD stand predictions. The forest stands visually identified as non-disturbed (i.e., 44 stands since 6 were part of the training set) were similarly excluded from the

validation dataset since the actual age of the last stand-replacing disturbance was unknown. As a result, the accuracy assessment was conducted on a total of 681 stands.

The accuracy of the predictions at the forest stand-level was evaluated using five metrics, defined as follows.

Root Mean Square Difference between predicted and observed TSD (RMSD):

$$RMSD = \sqrt{\frac{\sum_{i=1}^{n}(\hat{Y}_i - Y_i)^2}{n}} \quad (1)$$

where *n* is the number of forest stands, $\hat{Y}_i$ is the predicted TSD for stand *i*, and Y_i is the observed TSD for stand *i*. RMSD has been used in imputation as an accuracy metric similar to the traditional RMSE used for regression model accuracy (Stage and Crookston, 2007).

Relative RMSD ($RMSD_{rel}$):

$$RMSD_{rel} = \frac{RMSD}{\frac{1}{n}\sum_{i=1}^{n} Y_i} x100 \quad (2)$$

where *n* is the number of forest stands, and Y_i is the observed TSD for stand *i*.

The bias (BIAS):

$$BIAS = \frac{1}{n}\sum_{i=1}^{n}(\hat{Y}_i - Y_i) \quad (3)$$

where *n* is the number of forest stands, $\hat{Y}_i$ is the predicted TSD for stand *i*, and Y_i is the observed TSD for stand *i*. The bias shows overall trend in over and underestimations between predicted and observed year of disturbance.

Relative bias ($BIAS_{rel}$):

$$BIAS_{rel} = \frac{\sum_{i=1}^{n}(\hat{Y}_i - Y_i)}{\sum_{i=1}^{n} Y_i} x100 \quad (4)$$

where *n* is the number of forest stands, $\hat{Y}_i$ is the predicted TSD for stand *i*, and Y_i is the observed TSD for stand *i*.

Percentage of forest stands that had less than 10 years of absolute error (Perct.10):

$$Perct.10 = \left(\frac{\sum_{i=1}^{n}\left|\hat{Y}_i - Y_i\right| < 10}{n}\right) x100 \quad (5)$$

where n is the number of forest stands, $\hat{Y}_i$ is the predicted TSD for stand i, and Y_i is the observed TSD for stand i.

Additionally, a confusion matrix of the stand-level predictions aggregated by decade was also computed, using the reference dataset as defined above, with the addition of the 44 undisturbed forest stands not used in the training.

Predictor Variable Importance

Because there is significant correlation among the predictor metrics of each group (i.e. canopy height & complexity, canopy density, topography), the measures of variable importance that are directly generated by RF classifiers can potentially result in spurious rankings that do not reflect the actual importance of the predictors (Nicodemus et al., 2010; Strobl et al., 2008). The relative importance of the predictor variables was therefore assessed though the methods proposed by Roy and Kumar (2017) and Tulbure et al. (2012), specifically designed to deal with correlated predictor variables.

We examined all the possible combinations of predictor metrics selecting one metric at a time from each of the three groups, resulting in a total of a total of 324 combinations. If the predictor metrics of a particular combination were highly correlated (i.e. absolute value |R| of the Pearson coefficient greater than 0.5), then the combination was discarded. For each uncorrelated combination, a RF classifier was trained and the Mean Decrease in the Gini (MDG) index, which is a robust metric of variable importance (Breiman, 2001), was used to rank the three predictors. The percentage of times that each specific metric ranked first, second and third was calculated, and used as overall measure of the relative importance of each predictor and group.

Additionally, partial dependence plots with probability distribution based on scaled margin distances of the most important metrics were generated using the rf.partial.prob function implemented in the R rfUtilities package (Evans and Murphy, 2018).

Sensitivity Analysis

A sensitivity analysis was performed, to determine the sensitivity of the accuracy metrics to the sample size. The number of randomly selected forest stands in each stratum was varied from 1 to 10, and for each size the random selection was repeated 10 times. The three forest stands with the lowest and the highest ‘H95’ (i.e., 6 forest stands) were always included in the training dataset. The entire classification procedure was repeated for each set (100 output classifications in total), and the accuracy

of each classification was assessed by computing the RMSD, BIAS and Perct.10 metrics. Non-parametric statistics (median, 25^{th} and 75^{th} percentiles) of the accuracy metrics were calculated for each sample size.

Results

TSD Estimation

The RF classifier was trained using the 17,604 cells selected as detailed above, and cell-level imputations of TSD were generated for the entire study area (Figure 2.7). The OOB (Out of Bag) error estimate of the RF is considered as a robust indicator of error rate that correlates well with the estimated error of cross-validation and it was relatively low (OOB error= 0.10).

The cell level TSD imputations were subsequently aggregated through the use of the median operator to generated the stand-level disturbance history map, displayed in Figure 2.8. The study area was broadly disturbed by fires in 1919, so this historic disturbance event was well represented in the training data (Table 2.4), in the cell-level imputation (Figure 2.7), and in the disturbance history map (Figure 2.8).

Accuracy Assessment

RMSD was 17.5 years and $RMSD_{rel}$ was 24.2%, while BIAS was 0.8 years and $BIAS_{rel}$ was 1.1%, i.e., the predicted year of the disturbance was slightly before to the observed year. The percentage of stands with less than 10 years of absolute error (Perct.10) was relatively high (72.8%.) considering the large dataset of forest stands included in the accuracy assessment; i.e., 681 stands after excluding the 56 stands selected for training and the 44 non-disturbed stands (Figure 2.4); this percentage increased to 78.4% when only stands disturbed since the decade of 1910 were considered (i.e., forest stand disturbed within the last 100 years).

The confusion matrix of the disturbance history map at decadal steps (Table 2.5) showed a relatively good agreement between reference and predicted TSD values, especially in recently disturbed stands (i.e., forest stands disturbed within the last 60 years) where confusion mainly happened between subsequent decades. On the other hand, forest stands disturbed in the 1930s (specifically in 1931) were sometimes classified as disturbed in the 1910s (specifically in 1919); and forest stands disturbed in the 1880s were often classified as disturbed in the 1910s and vice versa.

Predictor Variable Importance

Table 2.6 presents the results of the variable importance analysis. Out of the 324 possible combinations of predictor metrics from each group (Table 2.2), 210 had low pairwise correlation

between metrics (i.e. $|R| < 0.5$) and were retained in the analysis. Significant correlation between Canopy density and Canopy height & complexity metrics was observed: for example, the 'ST_ab30' and the 'ST_5-10' density metrics had high correlation with all canopy height and complexity metrics—rumple index excepted—and were therefore only included in six combinations. Topography metrics were always uncorrelated with the metrics from the other two groups.

The 'H95' metric had the highest predictive power among all metrics: every time it was in a combination, it ranked first importance based on MDG. It was followed by 'H.Ave', 'H75' and the Rumple index, all ranking first 83% of the times. When the results are aggregated by group (Table 2.7), the Canopy height & complexity group are the most important (ranking first in 82% of the combinations), followed by the topography (13%) and density metrics (5%).

The partial dependence plots of the 'H95', 'H.Ave' and 'H75' metrics (Figure 2.9) all indicate, as expected, a general pattern of monotonic relationship between tree height and TSD. Among the variable, 'H95' shows a better ability to discriminate TSD than the other two height metrics. For instance, considering the 'H95' metric, the mode of the probability distribution for the 10-19 years TSD class corresponds to a height of ~4.5 m, and it increases to ~10.5 m for the 20-29 years TSD class. By contrast, 'H75' and 'H.Ave' are less sensitive to TSD: the mode of the 10-19 year TSD class is ~3 m for 'H75' and ~2 m for 'H.Ave', and the mode of the 20-29 year TSD class is ~4 m for 'H75' and ~3 m for 'H.Ave'. The rumple index, which is a measure of canopy complexity, shows that the complexity of the canopy increases with stand age, albeit without a clear separation, except for the separation between the oldest stands, and those disturbed in the last 140 years.

Sensitivity Analysis

One hundred disturbance history maps were obtained varying the number of forest stands selected per stratum in the stratification (from 1 to 10) (Figure 2.5), and replicating the random selection as well 10 times.

Overall accuracy was influenced by the number of training stands, with the highest accuracy achieved when ten stands are selected, and dropping very significantly especially when fewer than four stands per stratum were selected (Figure 2.10). RMSD ranged from 20.0 to 32.2 years (median: 24.6 years) if only one forest stand was sampled; it ranged from 17.4 to 21.3 years (median: 19.6 years) if five stands were sampled; and from 15.4 to 19.2 years (median: 17.5 years) if ten stands were sampled. Similarly, BIAS ranged from -1.3 to 18.8 years (median: 4.8 years) if only one forest stand was sampled; it ranged from -0.8 to 6.6 years (median: 2.1 years) if five stands were sampled; and from -1.9 and 2.3 years (median: -0.9 years) if ten forest stands were sampled. And finally, Perct.10 ranged

from 41.9 and 65.3% (median: 51.9 %) if one stand was sampled, it ranged from 64.2 to 72.8% (median: 70.8 %) if five forest stands were sampled, and from 70.2 to 80.1% (median: 74.5%) if ten stands were sampled.

Discussion

TSD is generally missing or incomplete for most forested areas and rarely extends to the past longer than the available satellite record. Traditionally, field data collection can expand such record, but this requires time-consuming and expensive field inventory and dendrochronological analyses (Speer, 2010).

This study presents a methodology to predict TSD and map disturbances at the stand-level using RF analysis on single date airborne LiDAR data. This approach is designed to complement the more established optical-data based methodologies used for detecting forest disturbances, which are limited by the temporal coverage of the optical Earth Observation record. Our results indicate that canopy LiDAR metrics are well suited to reconstruct the long term disturbance history of a forest, provided that reference data of the different disturbance times is available for training a RF imputation. Additionally, the introduction of meaningful spatial units of analysis (i.e., even-aged forest stands) introduces contextual information that is advantageous to reduce the time required for analysis (i.e., by reducing the amount of training data required to impute TSD); and to reduce the inherent variability of cell-level analyses. This is particularly relevant when estimating an attribute—such as TSD—that is inherently constant across all cells of a stand. Another methodological advantage, apart from above comments on the stand-level approach, is the use of current, single-date LiDAR data, which reduces the amount of historical time series data required to impute TSD. The disturbance history map obtained by applying the proposed methodology shows good accuracy, as reflected by the overall RMSD (17.5 years) BIAS (0.08 years) and Perct.10 (72.8%). Unsurprisingly, the progressively uneven-aged distribution of the canopy due to natural tree mortality of pioneer species creating gaps that become filled with younger trees (Luyssaert et al., 2008) negatively affects the overall accuracy of the TSD estimation for very old disturbances (>100 years).

The predictor variable importance analysis indicated that canopy height metrics are the strongest TSD predictors, followed by topography and by density. This is not surprising considering the well-known, strong relationship between stand age and growth (Monserud, 1984; Oliver and Larson, 1996; Ryan et al., 2004). The ‘H95’ metric, in particular, had the highest importance, reflecting the fact that it represents the dominant cohort of the forest canopy (Kane et al., 2010) so it was expected to have a stronger predictive power than other percentiles of the return height distribution. Our variable importance ranking is consistent with previously published results: Racine et al. (2014) predicted stand

age on field plots using similar LiDAR predictors as used in the present research, and K-NN imputation, finding 'H95' to be the most important predictor of stand age, and the topographic elevation the most significant out of the topographic metrics included in their research as site index indicators. Out of the density metrics used in our study, the 'ST_20_30' metric was the most important 28% of the times and ranked second 61% of the times, which might be explained because in many stands 20-30 m is the range encompassing the height of the dominant tree cohort, as reflected by the distribution of 'H95' in the stands with known TSD (the mean 'H95' is 24.5 m, the median 'H95' is 26.1 m, see Figure 2.4). The density metrics might therefore capture some residual variability of the structural complexity of the landscape, and consequently contribute to the TSD prediction.

The uncertainties of the TSD prediction, reflected by the accuracy metrics, can be attributed, at least in part, to the uncertainties of the ancillary reference dataset: any errors in the reference data would translate into inaccuracies both in the TSD imputation and in the accuracy assessment. Although theoretically the TSD ancillary dataset covered the study area wall-to-wall, and extended for 140 years of past disturbances, the record is not complete. Harvest reference data prior to the 1950s are missing, and false negatives are likely present in the burn history dataset. The areas located within the perimeters of the 1919 and the 1931 large fires, for instance, were very heterogeneous in vegetation structure parameters, and it is likely that some post-fire logging had occurred before the start of the FACTS data record. In these cases, the site conditions and the actual severity of the fires in each specific stand drives the recovery rates at different phases, making one decade between two disturbance events not enough to substantially distinguish the successional states of some stands (e.g., there are only twelve years of difference between the large fires of 1919 and 1931). Therefore, some confusion in the classification was expected, especially in old stands (Table 2.5). Misclassification in these cases was also accentuated by the scarcity or outrights absence of reference data in some specific decades (e.g., 1900, 1890) and the overrepresentation of other decades (e.g., 1910s).

These limitations notwithstanding, this study showed that it is possible to generate a classification of TSD with high accuracy at the decadal scale by using only 56 forest stands as training dataset, i.e. 3.8% of the total number of stands of the study area. The sensitivity analysis indicates that the accuracy of the methodology has low sensitivity to the size of the training set, with the accuracy of the TSD prediction dropping significantly only when fewer than four stands are selected from each stratum (Figure 2.10). This is a particularly significant result, because it indicates that a limited amount of fieldwork would be sufficient to generate enough training data to apply the proposed methodology to a new area where no reference data are available. Furthermore, the stratification is entirely based on topographic and LiDAR metrics, hence not requiring any prior knowledge of the TSD distribution.

We demonstrated that forest structure as observed by LiDAR is a strong predictor for stand-level TSD in the area considered by this study. Some caution should be used when extrapolating these results to different ecosystems. The good performance of the proposed methodology might be influenced by the particular conditions of the study area, covering a temperate mixed-conifer forest subject to high disturbance pressure, with more than half of the study area having undergone stand-replacing disturbances since 1870 (Table 2.3). While other management activities such as occasional overstory removal, salvage cuts, and biomass removal have been accomplished in the study area (USDA, Forest Service, 2016), even-aged management (including clearcut, shelterwood and seed-tree harvest) was the dominant regeneration method. The landscape is therefore dominated by even-aged forest stands of relatively large size (average of 35.5 ha), which are the result of large wildfires that occurred at the beginning of the 20th century and widespread harvest in the second half of the 20th century. In other areas of the world, the mosaics created by even-aged management might be less evident if the stands are smaller, and uneven-aged and intermediate cutting are predominantly. Similarly, fire disturbance regimes in other ecoregions might determine other landscape structural shapes depending on the predominant severity and extension of the burns. Besides this, stand development and recovery rates after a disturbance also depend on the geographic location (Cole et al., 2014), pre-disturbance situation (Ilisson and Chen, 2009) which can determine atypical stand structures, and post-disturbance management. In the former case, for instance, burnt biomass removal is rare in large forests such as those of the Pacific Northwest, especially in areas hard to reach, while it is a more common practice in European countries with less inaccessible areas. Other management practices, such seedling, accelerate vegetation regeneration rates compare to natural regrowth, which is a slower process since trees might span over several decades (Pregitzer and Euskirchen, 2004). As a result, accurate TSD prediction in different ecoregions and forest types might require a different stratification strategy and a larger training dataset than in the present study.

Conclusions

The disturbance history map obtained in this research largely expands the temporal contextualization of stand-replacing disturbances beyond what can be done with traditional optical remotely sensed data and change detection analysis. Stand-replacing disturbance legacies in the Nez Perce-Clearwater National forest remain distinct in the horizontal and vertical structures of the vegetation for a long period (i.e., ~100 years), and LiDAR canopy and topographic metrics have enough explanatory power to categorize these disturbance patterns through time. The obtained map is unprecedented in the literature considering both the temporal extent (>140 years) and the approach (stand-level based) of the analysis, and its overall accuracy is satisfactory especially within the first 100 years after disturbance occurrence, requiring a relatively low amount of training stands to generate it.

On the other hand, the integration of meaningful spatial units of analysis in the workflow (i.e., forest stand perimeters) provides a contextual frame of analysis that constitutes a methodological advantage to improve TSD estimates, among other reasons, because information of the spatial relationship between cells gets intrinsically incorporated into the analysis.

We expect stand-replacing disturbance legacies in the form of horizontal and vertical canopy structural signatures to be recognizable with LiDAR data for a long period in temperate forests with similar disturbance dynamics (e.g., other forests in the Pacific Northwest). Therefore, LiDAR data can be used to map disturbances that pre-date the beginning of the Landsat data record in 1972 and have potential to model disturbance patterns over the long-term (i.e., ~100 years), implementing a stand-level analysis.

Overall, the combination of different data sources and strategies to reconstruct the disturbance history of forested areas, including this methodology, will increase the amount of reliable ready-to-use maps of TSD, which are required to improve carbon cycle modelling and the understanding of forest ecosystem processes. Further research would involve the replication of the analysis to other study sites, the evaluation of other predictors to impute TSD, such as climatic variables, and the categorization of other disturbance attributes such as typology or severity.

Acknowledgements

We thank Pat Green and Penny Morgan for sharing the portion of the historic fire geodatabase that overlapped the FACTS geodatabase and LiDAR acquisitions to delimit our study area. A field campaign (not related to the present paper) was conducted in the study area in 2016. It greatly contributed to design this research, therefore, we thank to everyone who helped on it, especially to Darko Veljković, Patrick Fekety, Patrick Mahoney and Adrienne Marshall.

The project is supported by NASA's Land-Cover/Land-Use Change (LCLUC) program (award number NHX14AD92G) and the Carbon Monitoring System (CMS) (award number NNH15AZ06I), and by USDA NIFA grant 2011-32100-06016.

References

Baatz, M., Schape, A., 2000. Multiresolution Segmentation–an optimization approach for high quality multi-scale image segmentation. AGIT-Symposium Salzburg 2000, 12–23.

Blaschke, T., Lang, S., Hay, G., 2008. Object-Based Image Analysis: Spatial Concepts for Knowledge-Driven Remote Sensing Applications. Springer Science & Business Media.

Böck, S., Immitzer, M., Atzberger, C., 2017. On the Objectivity of the Objective Function—Problems with Unsupervised Segmentation Evaluation Based on Global Score and a Possible Remedy. Remote Sens. 9, 769. https://doi.org/10.3390/rs9080769

Bonnell, T.R., Reyna-Hurtado, R., Chapman, C.A., 2011. Post-logging recovery time is longer than expected in an East African tropical forest. For. Ecol. Manag. 261, 855–864.

Bradford, J.B., Birdsey, R.A., Joyce, L.A., Ryan, M.G., 2008. Tree age, disturbance history, and carbon stocks and fluxes in subalpine Rocky Mountain forests. Glob. Change Biol. 14, 2882–2897. https://doi.org/10.1111/j.1365-2486.2008.01686.x

Breiman, L., 2001. Random forests. Mach. Learn. 45, 5–32.

Chapin III, F.S., Matson, P.A., Mooney, H.A., 2002. Principles of terrestrial ecosystem ecology–Springer-Verlag. N. Y. USA 298–300.

Chen, G., Hay, G.J., Carvalho, L.M., Wulder, M.A., 2012. Object-based change detection. Int. J. Remote Sens. 33, 4434–4457.

Clinton, N., Holt, A., Scarborough, J., Yan, L.I., Gong, P., others, 2010. Accuracy assessment measures for object-based image segmentation goodness. Photogramm. Eng. Remote Sens. 76, 289–299.

Cochrell, A.N., 1960. The Nezperce Story: A History of the Nezperce National Forest. USDA Forest Service: Missoula, MT, USA.

Cohen, W.B., Goward, S.N., 2004. Landsat's Role in Ecological Applications of Remote Sensing. BioScience 54, 535–545. https://doi.org/10.1641/0006-3568(2004)054[0535:LRIEAO]2.0.CO;2

Cohen, W.B., Spies, T.A., Alig, R.J., Oetter, D.R., Maiersperger, T.K., Fiorella, M., 2002. Characterizing 23 years (1972–95) of stand replacement disturbance in western Oregon forests with Landsat imagery. Ecosystems 5, 122–137.

Cohen, W.B., Spies, T.A., Fiorella, M., 1995. Estimating the age and structure of forests in a multi-ownership landscape of western Oregon, U.S.A. Int. J. Remote Sens. 16, 721–746. https://doi.org/10.1080/01431169508954436

Cole, L.E., Bhagwat, S.A., Willis, K.J., 2014. Recovery and resilience of tropical forests after disturbance. Nat. Commun. 5, 3906.

Crookston, N.L., Finley, A.O., 2008. yaImpute: an R package for kNN imputation.

Drăguţ, L., Csillik, O., Eisank, C., Tiede, D., 2014. Automated parameterisation for multi-scale image segmentation on multiple layers. ISPRS J. Photogramm. Remote Sens. 88, 119–127. https://doi.org/10.1016/j.isprsjprs.2013.11.018

Espindola, G.M., Camara, G., Reis, I.A., Bins, L.S., Monteiro, A.M., 2006. Parameter selection for region-growing image segmentation algorithms using spatial autocorrelation. Int. J. Remote Sens. 27, 3035–3040. https://doi.org/10.1080/01431160600617194

Evans, J.S., Murphy, M.A., 2018. Package 'rfUtilities.'

Fisher, P., 1997. The pixel: A snare and a delusion. Int. J. Remote Sens. 18, 679–685. https://doi.org/10.1080/014311697219015

Franklin, J.F., Spies, T.A., Pelt, R.V., Carey, A.B., Thornburgh, D.A., Berg, D.R., Lindenmayer, D.B., Harmon, M.E., Keeton, W.S., Shaw, D.C., Bible, K., Chen, J., 2002. Disturbances and structural development of natural forest ecosystems with silvicultural implications, using Douglas-fir forests as an example. For. Ecol. Manag., Forest Ecology in the next Millennium : Putting the long view into Practice 155, 399–423. https://doi.org/10.1016/S0378-1127(01)00575-8

Frolking, S., Palace, M.W., Clark, D.B., Chambers, J.Q., Shugart, H.H., Hurtt, G.C., 2009. Forest disturbance and recovery: A general review in the context of spaceborne remote sensing of impacts on aboveground biomass and canopy structure. J. Geophys. Res. Biogeosciences 114, G00E02. https://doi.org/10.1029/2008JG000911

Fu, Z., Li, D., Hararuk, O., Schwalm, C., Luo, Y., Yan, L., Niu, S., 2017. Recovery time and state change of terrestrial carbon cycle after disturbance. Environ. Res. Lett. 12, 104004.

Gobakken, T., Korhonen, L., N\a esset, E., 2013. Laser-assisted selection of field plots for an area-based forest inventory. Silva Fenn. 47, 943.

Hansen, M.C., Potapov, P.V., Moore, R., Hancher, M., Turubanova, S.A., Tyukavina, A., Thau, D., Stehman, S.V., Goetz, S.J., Loveland, T.R., Kommareddy, A., Egorov, A., Chini, L., Justice, C.O., Townshend, J.R.G., 2013. High-Resolution Global Maps of 21st-Century Forest Cover Change. Science 342, 850–853. https://doi.org/10.1126/science.1244693

Hansen, M.C., Stehman, S.V., Potapov, P.V., Loveland, T.R., Townshend, J.R.G., DeFries, R.S., Pittman, K.W., Arunarwati, B., Stolle, F., Steininger, M.K., Carroll, M., DiMiceli, C., 2008. Humid tropical forest clearing from 2000 to 2005 quantified by using multitemporal and

multiresolution remotely sensed data. Proc. Natl. Acad. Sci. 105, 9439–9444. https://doi.org/10.1073/pnas.0804042105

Hawbaker, T.J., Keuler, N.S., Lesak, A.A., Gobakken, T., Contrucci, K., Radeloff, V.C., 2009. Improved estimates of forest vegetation structure and biomass with a LiDAR-optimized sampling design. J. Geophys. Res. Biogeosciences 114.

Hayes, D.J., Sader, S.A., 2001. Comparison of change-detection techniques for monitoring tropical forest clearing and vegetation regrowth in a time series. Photogramm. Eng. Remote Sens. 67, 1067–1075.

Healey, S.P., Cohen, W.B., Zhiqiang, Y., Krankina, O.N., 2005. Comparison of Tasseled Cap-based Landsat data structures for use in forest disturbance detection. Remote Sens. Environ. 97, 301–310. https://doi.org/10.1016/j.rse.2005.05.009

Hopkinson, C., Chasmer, L., Hall, R.J., 2008. The uncertainty in conifer plantation growth prediction from multi-temporal lidar datasets. Remote Sens. Environ. 112, 1168–1180. https://doi.org/10.1016/j.rse.2007.07.020

Huang, C., Goward, S.N., Masek, J.G., Gao, F., Vermote, E.F., Thomas, N., Schleeweis, K., Kennedy, R.E., Zhu, Z., Eidenshink, J.C., Townshend, J.R.G., 2009. Development of time series stacks of Landsat images for reconstructing forest disturbance history. Int. J. Digit. Earth 2, 195–218. https://doi.org/10.1080/17538940902801614

Hudak, A.T., Strand, E.K., Vierling, L.A., Byrne, J.C., Eitel, J.U.H., Martinuzzi, S., Falkowski, M.J., 2012. Quantifying aboveground forest carbon pools and fluxes from repeat LiDAR surveys. Remote Sens. Environ. 123, 25–40. https://doi.org/10.1016/j.rse.2012.02.023

Huo, L.-Z., Boschetti, L., Sparks, A.M., 2019. Object-Based Classification of Forest Disturbance Types in the Conterminous United States. Remote Sens. 11, 477. https://doi.org/10.3390/rs11050477

Hussain, M., Chen, D., Cheng, A., Wei, H., Stanley, D., 2013. Change detection from remotely sensed images: From pixel-based to object-based approaches. ISPRS J. Photogramm. Remote Sens. 80, 91–106. https://doi.org/10.1016/j.isprsjprs.2013.03.006

Ilisson, T., Chen, H.Y., 2009. Response of six boreal tree species to stand replacing fire and clearcutting. Ecosystems 12, 820–829.

Johnson, B., Xie, Z., 2011. Unsupervised image segmentation evaluation and refinement using a multi-scale approach. ISPRS J. Photogramm. Remote Sens. 66, 473–483. https://doi.org/10.1016/j.isprsjprs.2011.02.006

Kane, V.R., McGaughey, R.J., Bakker, J.D., Gersonde, R.F., Lutz, J.A., Franklin, J.F., 2010. Comparisons between field- and LiDAR-based measures of stand structural complexity. Can. J. For. Res. 40, 761–773. https://doi.org/10.1139/X10-024

Kennedy, R.E., Yang, Z., Cohen, W.B., 2010. Detecting trends in forest disturbance and recovery using yearly Landsat time series: 1. LandTrendr — Temporal segmentation algorithms. Remote Sens. Environ. 114, 2897–2910. https://doi.org/10.1016/j.rse.2010.07.008

Liebsch, D., Marques, M.C., Goldenberg, R., 2008. How long does the Atlantic Rain Forest take to recover after a disturbance? Changes in species composition and ecological features during secondary succession. Biol. Conserv. 141, 1717–1725.

Liu, Y., Bian, L., Meng, Y., Wang, H., Zhang, S., Yang, Y., Shao, X., Wang, B., 2012. Discrepancy measures for selecting optimal combination of parameter values in object-based image analysis. ISPRS J. Photogramm. Remote Sens. 68, 144–156. https://doi.org/10.1016/j.isprsjprs.2012.01.007

Lu, D., Mausel, P., Brondízio, E., Moran, E., 2004. Change detection techniques. Int. J. Remote Sens. 25, 2365–2401.

Lunetta, R.S., Johnson, D.M., Lyon, J.G., Crotwell, J., 2004. Impacts of imagery temporal frequency on land-cover change detection monitoring. Remote Sens. Environ. 89, 444–454. https://doi.org/10.1016/j.rse.2003.10.022

Luyssaert, S., Schulze, E.-D., Börner, A., Knohl, A., Hessenmöller, D., Law, B.E., Ciais, P., Grace, J., 2008. Old-growth forests as global carbon sinks. Nature 455, 213–215. https://doi.org/10.1038/nature07276

Masek, J.G., Huang, C., Wolfe, R., Cohen, W., Hall, F., Kutler, J., Nelson, P., 2008. North American forest disturbance mapped from a decadal Landsat record. Remote Sens. Environ. 112, 2914–2926. https://doi.org/10.1016/j.rse.2008.02.010

McGaughey, R.J., 2009. FUSION/LDV: Software for LIDAR data analysis and visualization. US Dep. Agric. For. Serv. Pac. Northwest Res. Stn. Seattle WA USA 123.

Monserud, R.A., 1984. Height Growth and Site Index Curves for Inland Douglas-fir Based on Stem Analysis Data and Forest Habitat Type. For. Sci. 30, 943–965. https://doi.org/10.1093/forestscience/30.4.943

Morgan, P., Hudak, A.T., Wells, A., Parks, S.A., Baggett, L.S., Bright, B.C., Green, P., 2017. Multidecadal trends in area burned with high severity in the Selway-Bitterroot Wilderness Area 1880–2012. Int. J. Wildland Fire 26, 930–943.

Nicodemus, K.K., Malley, J.D., Strobl, C., Ziegler, A., 2010. The behaviour of random forest permutation-based variable importance measures under predictor correlation. BMC Bioinformatics 11, 110. https://doi.org/10.1186/1471-2105-11-110

Oliver, C.D., 1980. Forest development in North America following major disturbances. For. Ecol. Manag. 3, 153–168.

Oliver, C.D., Larson, B.C., 1996. Forest stand dynamics: updated edition. John Wiley and sons.

Pan, Y., Chen, J.M., Birdsey, R., McCullough, K., He, L., Deng, F., 2011. Age structure and disturbance legacy of North American forests. Biogeosciences 8 715-732 8, 715–732. https://doi.org/10.5194/bg-8-715-2011

Parker, G.G., Harmon, M.E., Lefsky, M.A., Chen, J., Van Pelt, R., Weis, S.B., Thomas, S.C., Winner, W.E., Shaw, D.C., Frankling, J.F., 2004. Three-dimensional structure of an old-growth Pseudotsuga-Tsuga canopy and its implications for radiation balance, microclimate, and gas exchange. Ecosystems 7, 440–453.

Pflugmacher, D., Cohen, W.B., E. Kennedy, R., 2012. Using Landsat-derived disturbance history (1972–2010) to predict current forest structure. Remote Sens. Environ., Landsat Legacy Special Issue 122, 146–165. https://doi.org/10.1016/j.rse.2011.09.025

Pregitzer, K.S., Euskirchen, E.S., 2004. Carbon cycling and storage in world forests: biome patterns related to forest age. Glob. Change Biol. 10, 2052–2077. https://doi.org/10.1111/j.1365-2486.2004.00866.x

Racine, E.B., Coops, N.C., St-Onge, B., Bégin, J., 2014. Estimating Forest Stand Age from LiDAR-Derived Predictors and Nearest Neighbor Imputation. For. Sci. 60, 128–136. https://doi.org/10.5849/forsci.12-088

Radke, R.J., Andra, S., Al-Kofahi, O., Roysam, B., 2005. Image change detection algorithms: a systematic survey. IEEE Trans. Image Process. 14, 294–307. https://doi.org/10.1109/TIP.2004.838698

Roberts, D.W.U.S.U., Cooper, S.V., 1989. Concepts and techniques of vegetation mapping. Gen. Tech. Rep. INT - US Dep. Agric. For. Serv. Intermt. Res. Stn. USA.

Rodriguez-Galiano, V.F., Chica-Olmo, M., Abarca-Hernandez, F., Atkinson, P.M., Jeganathan, C., 2012. Random Forest classification of Mediterranean land cover using multi-seasonal imagery and multi-seasonal texture. Remote Sens. Environ. 121, 93–107. https://doi.org/10.1016/j.rse.2011.12.003

Roy, D.P., Kumar, S.S., 2017. Multi-year MODIS active fire type classification over the Brazilian Tropical Moist Forest Biome. Int. J. Digit. Earth 10, 54–84.

Runkle, J.R., 1982. Patterns of Disturbance in Some Old-Growth Mesic Forests of Eastern North America. Ecology 63, 1533–1546. https://doi.org/10.2307/1938878

Ryan, M.G., Binkley, D., Fownes, J.H., Giardina, C.P., Senock, R.S., 2004. An Experimental Test of the Causes of Forest Growth Decline with Stand Age. Ecol. Monogr. 74, 393–414. https://doi.org/10.1890/03-4037

Sanchez-Lopez, N., Boschetti, L., Hudak, A., 2018. Semi-Automated Delineation of Stands in an Even-Age Dominated Forest: A LiDAR-GEOBIA Two-Stage Evaluation Strategy. Remote Sens. 10, 1622. https://doi.org/10.3390/rs10101622

Schroeder, T.A., Wulder, M.A., Healey, S.P., Moisen, G.G., 2011. Mapping wildfire and clearcut harvest disturbances in boreal forests with Landsat time series data. Remote Sens. Environ. 115, 1421–1433. https://doi.org/10.1016/j.rse.2011.01.022

Simard, M., Pinto, N., Fisher, J.B., Baccini, A., 2011. Mapping forest canopy height globally with spaceborne lidar. J. Geophys. Res. Biogeosciences 116.

Space, R.S., 1964. Clearwater story: a history of the Clearwater National Forest.

Spanner, M.A., Pierce, L.L., Peterson, D.L., Running, S.W., 1990. Remote sensing of temperate coniferous forest leaf area index The influence of canopy closure, understory vegetation and background reflectance. Int. J. Remote Sens. 11, 95–111.

Speer, J.H., 2010. Fundamentals of Tree-ring Research. University of Arizona Press.

Spies, T.A., 1998. Forest structure: a key to the ecosystem. Northwest Sci. 72, 34–36.

Stage, A.R., 1976. An Expression for the Effect of Aspect, Slope, and Habitat Type on Tree Growth. For. Sci. 22, 457–460. https://doi.org/10.1093/forestscience/22.4.457

Stage, A.R., Crookston, N.L., 2007. Partitioning error components for accuracy-assessment of near-neighbor methods of imputation. For. Sci. 53, 62–72.

Strobl, C., Boulesteix, A.-L., Kneib, T., Augustin, T., Zeileis, A., 2008. Conditional variable importance for random forests. BMC Bioinformatics 9, 307. https://doi.org/10.1186/1471-2105-9-307

Tulbure, M.G., Wimberly, M.C., Boe, A., Owens, V.N., 2012. Climatic and genetic controls of yields of switchgrass, a model bioenergy species. Agric. Ecosyst. Environ. 146, 121–129. https://doi.org/10.1016/j.agee.2011.10.017

Turner, D.P., Cohen, W.B., Kennedy, R.E., Fassnacht, K.S., Briggs, J.M., 1999. Relationships between Leaf Area Index and Landsat TM Spectral Vegetation Indices across Three Temperate Zone Sites. Remote Sens. Environ. 70, 52–68. https://doi.org/10.1016/S0034-4257(99)00057-7

Turner, M.G., 2010. Disturbance and landscape dynamics in a changing world1. Ecology 91, 2833–2849. https://doi.org/10.1890/10-0097.1

USDA, Forest Service, 2016. Forest Service Activity Tracking System (FACTs) harvest database. URL http://data.fs.usda.gov/geodata/edw/datasets.php

Vastaranta, M., Niemi, M., Wulder, M.A., White, J.C., Nurminen, K., Litkey, P., Honkavaara, E., Holopainen, M., Hyyppä, J., 2016. Forest stand age classification using time series of photogrammetrically derived digital surface models. Scand. J. For. Res. 31, 194–205.

Véga, C., St-Onge, B., 2009. Mapping site index and age by linking a time series of canopy height models with growth curves. For. Ecol. Manag. 257, 951–959. https://doi.org/10.1016/j.foreco.2008.10.029

Wulder, M.A., Skakun, R.S., Kurz, W.A., White, J.C., 2004. Estimating time since forest harvest using segmented Landsat ETM+ imagery. Remote Sens. Environ. 93, 179–187. https://doi.org/10.1016/j.rse.2004.07.009

Wulder, M.A., White, J.C., Loveland, T.R., Woodcock, C.E., Belward, A.S., Cohen, W.B., Fosnight, E.A., Shaw, J., Masek, J.G., Roy, D.P., 2016. The global Landsat archive: Status, consolidation,

and direction. Remote Sens. Environ., Landsat 8 Science Results 185, 271–283. https://doi.org/10.1016/j.rse.2015.11.032

Zhan, Q., Molenaar, M., Tempfli, K., Shi, W., 2005. Quality assessment for geo-spatial objects derived from remotely sensed data. Int. J. Remote Sens. 26, 2953–2974. https://doi.org/10.1080/01431160500057764

Zhang, C., Ju, W., Chen, J.M., Li, D., Wang, X., Fan, W., Li, M., Zan, M., 2014. Mapping forest stand age in China using remotely sensed forest height and observation data. J. Geophys. Res. Biogeosciences 119, 1163–1179. https://doi.org/10.1002/2013JG002515

Zimmerman, N., Presto, A.A., Kumar, S.P., Gu, J., Hauryliuk, A., Robinson, E.S., Robinson, A.L., Subramanian, R., 2018. A machine learning calibration model using random forests to improve sensor performance for lower-cost air quality monitoring. Atmospheric Meas. Tech. 11.

Table 2.1. LiDAR acquisition parameters.

	Clear Creek	**Selway River& Elk Creek**
Date	October 2009	June-July 2012
vendor	Earth Eye LLC, Orlando, FL	Watershed Sciences, Corvallis, OR
LiDAR sensor	Leica ALS60	Leica ALS50/ ALS60 Phase II
Scan angle	±6°	±14°
Pulse rate (Hz)	69,400	88,000
Altitude (m above ground level)	2400-3850	1200-1300
Minimum return density (pts/ m^2)	4	4

Table 2.2. LiDAR-derived summary metrics related to canopy structure (height & complexity, and density) and topography, computed as predictor variables for TSD modelling. All metrics are defined in 30m x 30m raster cells. On the equations, α is the topographic aspect in radians.

Predictor variables

Canopy height & complexity	H.Ave	Mean height value
	H05	5^{th} percentile of height above 1.37 m
	H25	25^{th} percentile of height above 1.37 m
	H75	75^{th} percentile of height above 1.37 m
	H95	95^{th} percentile of height above 1.37 m
	Rumple index	Canopy roughness. Canopy complexity
Canopy density	PRT1Mean	Percentage first returns above mean height over first returns
	PRT1BH	Percentage first returns above 1.37 m height over first returns
	ST_b0.15	Percentage of returns below 0.15 m. Inverse of total canopy density
	ST_0.15-1.37	Percentage of returns between 0.15 and 1.37 m
	ST_1.37-5	Percentage of returns between 1.37 and 5 m
	ST_5-10	Percentage of returns between 5 and 10 m
	ST_10-20	Percentage of returns between10 and 20 m
	ST_20-30	Percentage of returns between 20 and 30 m
	ST_ab30	Percentage of returns above 30 m
Topography	Elevation	Elevation (meters)
	SLP	Slope (percentage)
	SRI	Solar Radiation Index
	SRAI	Topographic solar-radiation aspect index $\text{SRAI} = \frac{1-\cos((\frac{\pi}{180})(\alpha-30))}{2}$ (Roberts and Cooper, 1989)
	SCA	Transformation cos(aspect) *x* Percent slope SCA= SLP x cos(α) (Stage, 1976)
	SSA	Transformation sine(aspect) *x* Percent slope SCA= SLP x sin(α) (Stage, 1976)

Table 2.3. Disturbed area reported on the ancillary reference dataset (Figure 2.1) and on the selected forest stands with known TSD (Figure 2.4) summarized by decade. Area is reported in number of disturbed hectares, and in percentage relative to the extent of the entire study area (52,257 ha). ND: forest stands non-disturbed since 1870.

	Ancillary reference dataset		Forest Stands with known TSD	
Disturbance Decade	**Area (ha)**	**Relative area (%)**	**Area (ha)**	**Relative area (%)**
ND	-	-	2121	4.06
1870	1199	2.29	1031	1.97
1880	5509	10.54	4745	9.08
1890	0	0.00	0	0.00
1900	0	0.00	0	0.00
1910	9928	19.00	9718	18.60
1920	756	1.45	644	1.23
1930	2884	5.52	2845	5.44
1940	278	0.53	322	0.62
1950	102	0.20	75	0.14
1960	2415	4.62	2176	4.16
1970	1799	3.44	1584	3.03
1980	773	1.48	614	1.18
1990	1026	1.96	758	1.45
2000	57	0.11	13	0.02
Total	26725	51.1	26644	51.0

Table 2.4. Number and percentage of stands with known TSD within the study area summarized by decade; and number and percentage of sampled forest stands following the LiDAR-assisted stratification strategy (Figure 2.6). ND: forest stands non-disturbed since 1870.

Decade	# Stands with known TSD	Stand with known TSD (%)	# Sampled stands	Sampled stands (%)
ND	50	6	6	11
1870	23	3	2	4
1880	112	14	7	13
1890	0	0	0	0
1900	0	0	0	0
1910	202	26	12	21
1920	14	2	0	0
1930	72	9	8	14
1940	11	1	1	2
1950	5	1	0	0
1960	57	7	6	11
1970	46	6	1	2
1980	89	11	3	5
1990	96	12	9	16
2000	4	1	1	2

Table 2.5. Confusion matrix of the TSD stand-level estimates of the 725 forest stands with known TSD not used to train the RF (Table 2.4) summarized by decade. ND: forest stands non-disturbed since 1870.

	Reference data														
Predictions	*ND*	*1870*	*1880*	*1890*	*1900*	*1910*	*1920*	*1930*	*1940*	*1950*	*1960*	*1970*	*1980*	*1990*	*2000*
ND	***22***	*0*	*1*	*0*	*0*	*0*	*0*	*0*	*0*	*0*	*0*	*0*	*0*	*0*	*0*
1870	8	**8**	4	0	0	0	0	0	0	0	0	0	0	0	0
1880	12	7	**53**	0	0	31	1	1	1	0	0	0	0	1	0
1890	0	0	0	**0**	0	0	0	0	0	0	0	0	0	0	0
1900	0	0	0	0	**0**	0	0	0	0	0	0	0	0	0	0
1910	2	5	45	0	0	**148**	12	10	6	0	1	3	0	1	0
1920	0	0	0	0	0	0	**0**	0	0	0	0	0	0	0	0
1930	0	1	1	0	0	8	1	**47**	3	1	6	3	3	1	2
1940	0	0	0	0	0	0	0	0	**0**	0	0	0	0	0	0
1950	0	0	0	0	0	0	0	0	0	**0**	0	0	0	0	0
1960	0	0	1	0	0	2	0	5	0	4	**44**	31	11	1	0
1970	0	0	0	0	0	0	0	0	0	0	0	**3**	4	0	0
1980	0	0	0	0	0	0	0	0	0	0	0	5	**39**	11	0
1990	0	0	0	0	0	1	0	1	0	0	0	0	29	**72**	0
2000	*0*	*0*	*0*	*0*	*0*	*0*	*0*	*0*	*0*	*0*	*0*	*0*	*0*	*0*	***1***

Table 2.6. Percentage and number (in brackets) of times that a predictor variable included in uncorrelated variable combinations ranked 1st, 2nd, or 3rd in order of importance based on the Mean Decrease in Gini (MDG) index of the RF. Pearson correlation threshold |R| = 0.5 for uncorrelated variable combination.

Predictor variable		Rank		
		1	2	3
Canopy height & complexity	H.Ave	83% (20)	17% (4)	0% (0)
	H05	69% (25)	28% (10)	3% (1)
	H25	63% (15)	33% (8)	4% (1)
	H75	83% (25)	17% (5)	0% (0)
	H95	**100% (42)**	0% (0)	0% (0)
	Rumple index	83% (45)	17% (9)	0% (0)
Canopy density	PRT1Mean	0% (0)	17% (2)	83% (10)
	PRT1BH	0% (0)	13% (13)	88% (21)
	ST_b0.15	0% (0)	25% (9)	75% (27)
	ST_0.15-1.37	0% (0)	0% (0)	100% (36)
	ST_1.37-5	0% (0)	05 (0)	100% (36)
	ST_5-10	0% (0)	83% (5)	17% (1)
	ST_10-20	0% (0)	445 (8)	56% (10)
	ST_20-30	28% (10)	61% (22)	11% (4)
	ST_ab30	0% (0)	83% (5)	17% (1)
Topography	Elevation	80% (28)	20% (7)	0% (0)
	SLP	0% (0)	71% (25)	29% (10)
	SRI	0% (0)	77% (27)	23% (8)
	SCA	0% (0)	77% (27)	23% (8)
	SSA	0% (0)	60% (21)	40% (14)
	TRSI	0% (0)	37% (13)	63% (22)

Table 2.7. Relative predictor variable importance summarized by group of metrics (Table 2.2), showing the percentage (and number) of uncorrelated variable combinations (out 210) that a variable from a group ranked 1st, 2nd, or 3rd (rank one is the most important) according to the Mean Decrease in Gini (MDG) index of the RF.

	Rank		
Predictor variable group	1	2	3
Canopy height & complexity	**82% (172)**	17% (36)	1% (2)
Canopy density	5% (10)	26% (54)	**69% (146)**
Topography	13% (28)	**57% (120)**	30% (62)

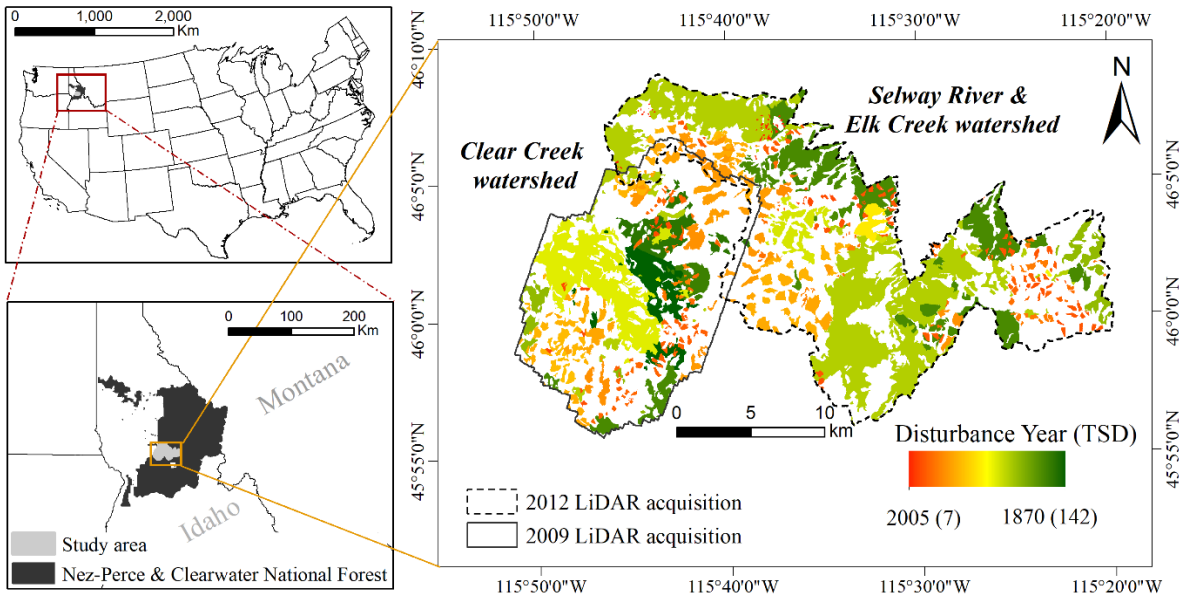

Figure 2.1. Location of the study area in the Nez Perce-Clearwater National Forest (Idaho, USA); boundaries of the 2009 and 2012 LiDAR acquisitions; ancillary reference dataset of stand-replacing disturbances compiled from historic burns digitized from aerial photos (Morgan et al., 2017), and the perimeters of the stand and patch clearcut management units reported in the Forest Service Activity Track System (FACTs) harvest dataset (USDA, Forest Service, 2016). The color scale indicates the disturbance year (ranging between 2005 and 1870) and Time Since Disturbance (TSD, in parentheses), calculated with reference to 2012, i.e. the year of the more recent LiDAR data acquisition.

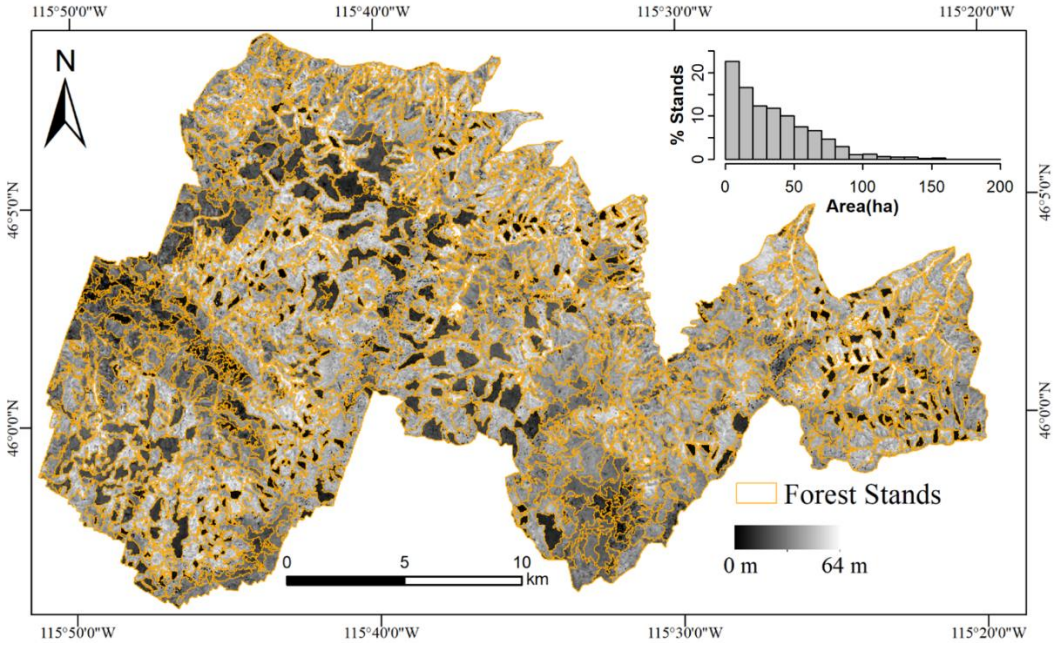

Figure 2.2. Forest stand map (orange vector) overlaid on the 'H95' LiDAR summary metric shown in grayscale. Top-right, histogram showing the percentage distribution of the size of the stands.

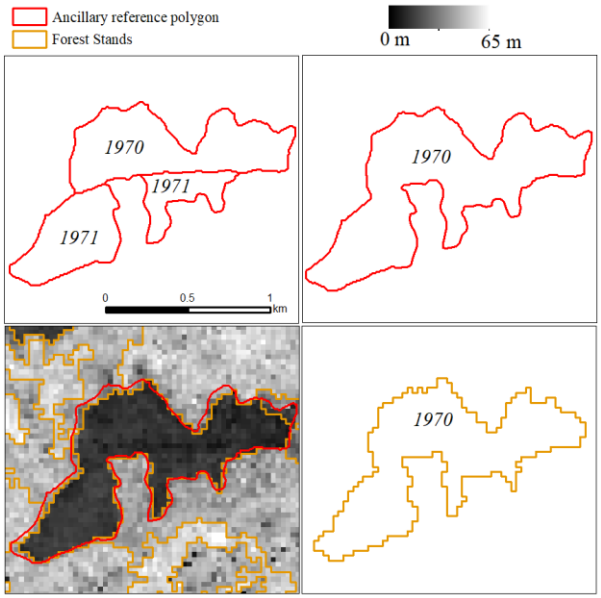

Figure 2.3. Pre-processing of the FACTs harvest management units (top row) and selection of forest stands with known TSD (bottom row). The top row shows an example of adjacent polygons harvested within a time interval ≤5 years (left) that are merged into aggregated polygons (right) that are used as ancillary reference polygons. Bottom row shows the corresponding forest stand with known TSD selected from the forest stand map (Figure 2.2) according to the 50% overlap area criterion. The 'H95' LiDAR summary metric is shown in grayscale in the bottom left figure.

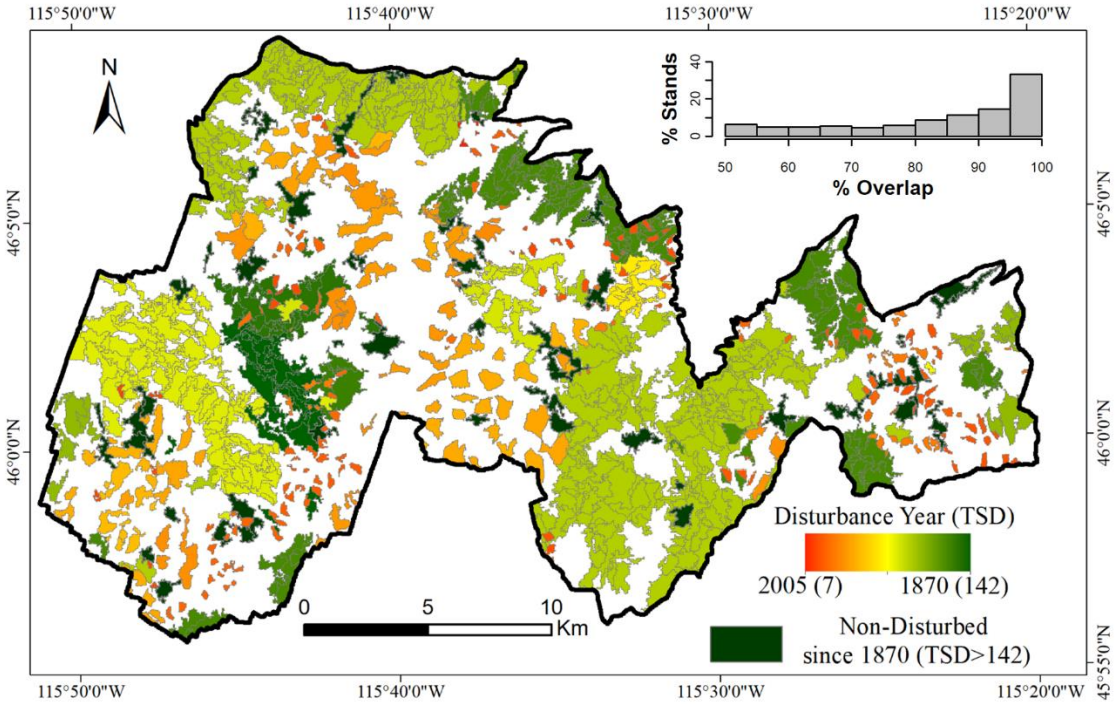

Figure 2.4. Forest stands with known TSD. Colour ramp indicates the disturbance year (ranging between 2005 and 1870) and Time Since Disturbance (TSD). Top-right, histogram showing the percentage distribution of the overlapping area (in %) between the forest stands with known TSD and the ancillary reference dataset (Figure 2.1).

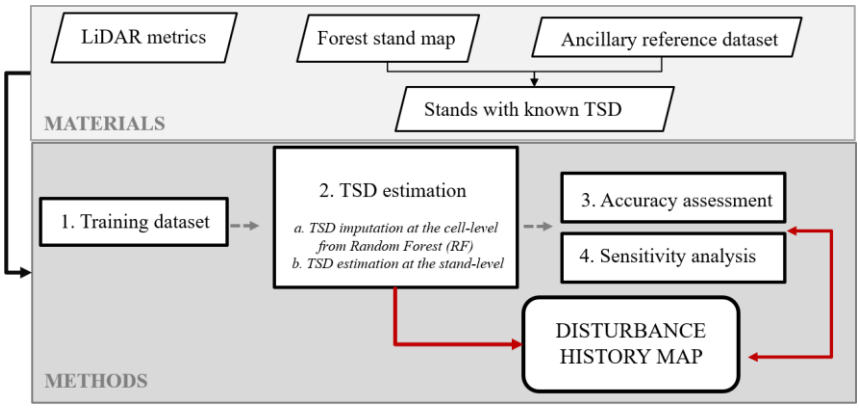

Figure 2.5. Workflow of the proposed methodology to generate a map of estimated Time Since the last stand-replacing Disturbance (TSD) at the forest stand-level.

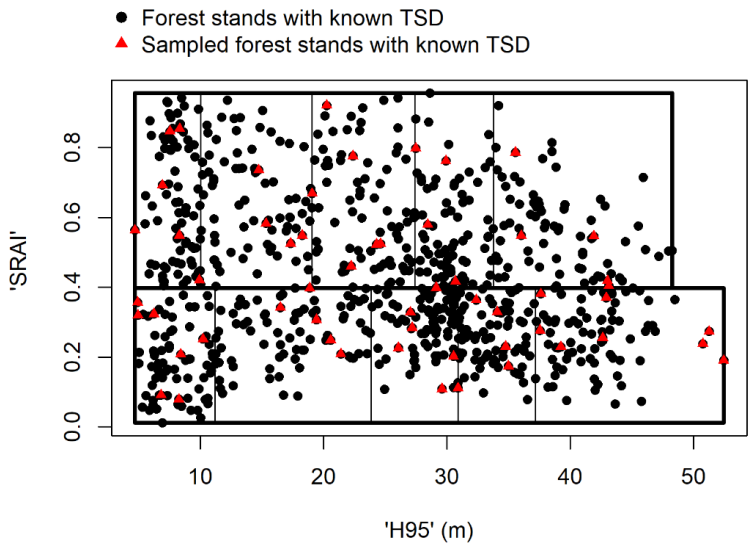

Figure 2.6. Scheme of the LiDAR-assisted stratification of the forest stands with known TSD. The mean topographic solar-radiation aspect index ('SRAI') and the mean 95th percentile of height above 1.37 m ('H95') are used as stratification variables. The 56 stands used as training dataset are reported as red triangles.

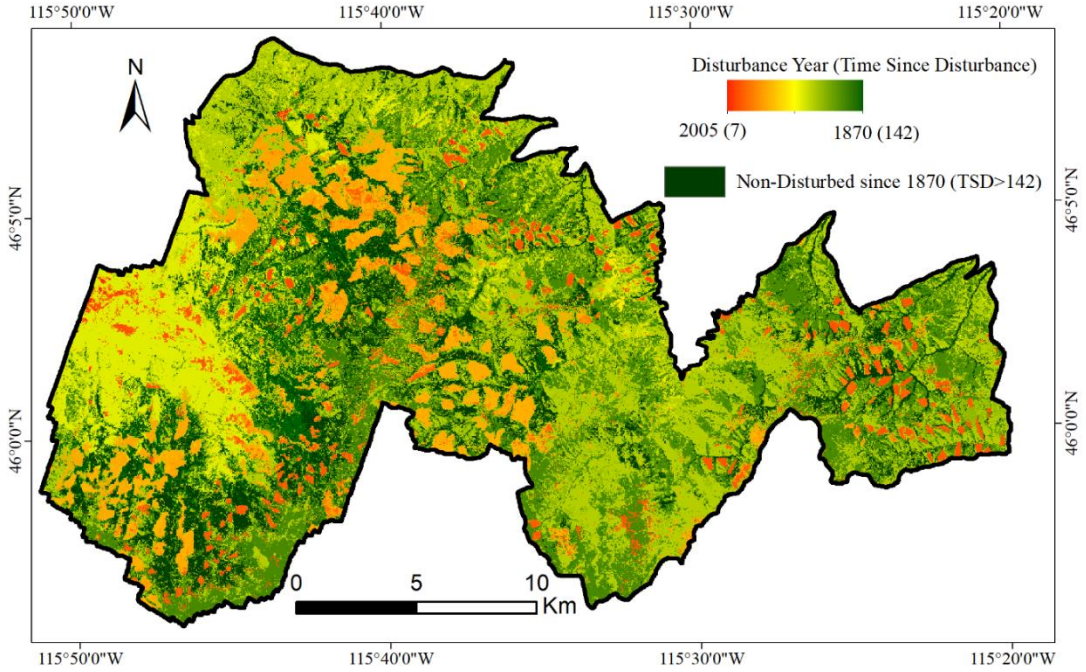

Figure 2.7. TSD imputations at the cell level using RF analysis and 21 LiDAR predictor variables related to canopy structure and topography (Table 2.2).

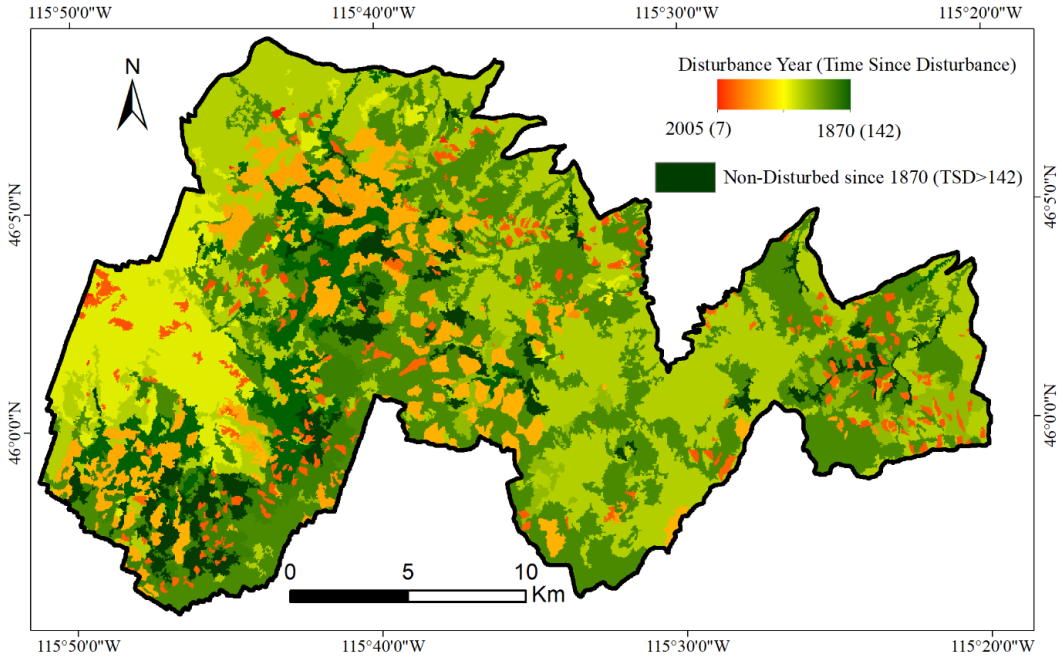

Figure 2.8. Stand-replacing disturbance history map. TSD stand-level calculated as the median value of the imputed TSD (Figure 2.7) cell estimates enclosed within the perimeters of the forest stands (Figure 2.2).

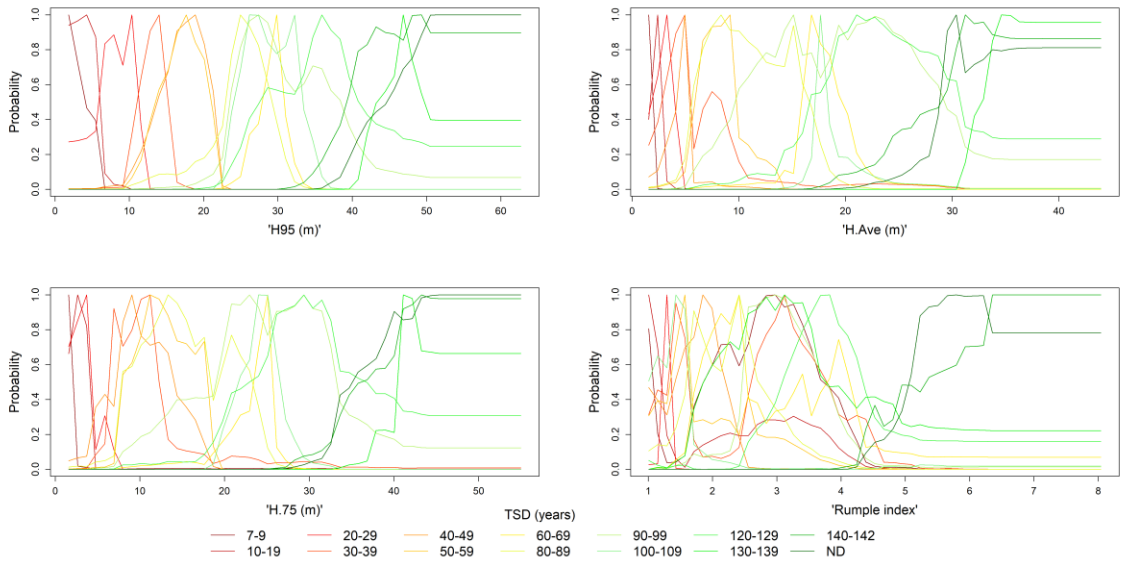

Figure 2.9. Partial dependence plots with probability distribution of TSD for the four variables with the highest importance (Table 2.6). Each curve represents the conditional TSD probability as a function of the LiDAR metrics (TSD is aggregated in 10-year bins).

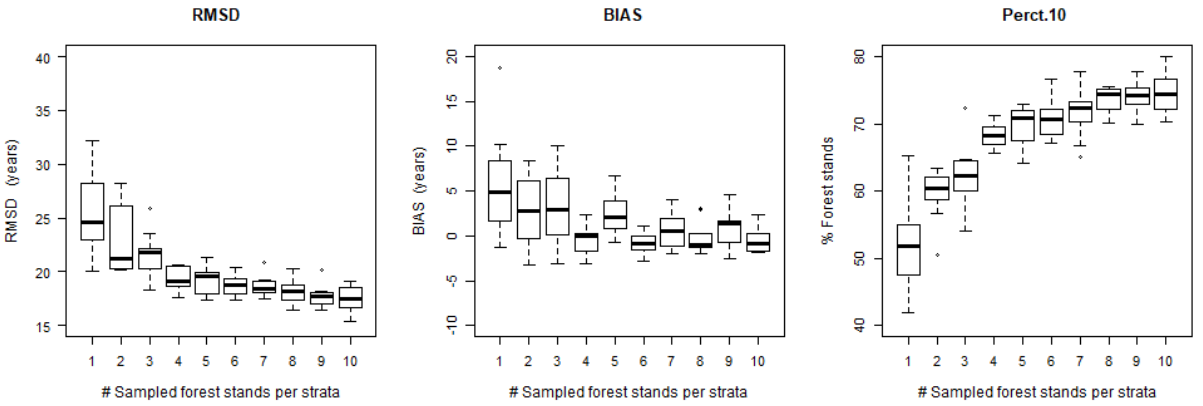

Figure 2.10. Boxplots of RMSD, BIAS, and Perct.10 obtained for TSD predictions when 1 to 10 forest stands were selected per stratum (Figure 2.6). The random selection of forest stands was replicated 10 times. Central line represents the median, edges of the box are the first (i.e., the 25th percentile) and the third (i.e., 75th percentile) quartiles, and the whiskers are 1.5 times the range of the upper and lower quartiles.

Chapter 3: Estimating Time Since the last stand-replacing Disturbance (TSD) from spaceborne GEDI data: a feasibility study.

Abstract

Stand-level maps of past forest disturbances (expressed as Time Since the Last stand-replacing Disturbance, TSD), are needed to model forest ecosystem processes, but the conventional approaches based on time series of optical remotely sensed satellite data can only extend as far back as the first available satellite observations. LiDAR data have proven potential to accurately map long-term TSD (~100 years). NASA's new spaceborne LiDAR Global Ecosystem Dynamics Investigation (GEDI) instrument, successfully launched in December 2018, will soon provide billions of measurements of the forest canopy of tropical and temperate forests around the globe. GEDI is, however, a sampling instrument that has ground footprints separated by ~600 m across track and ~60 m along-track, providing only discrete measurements of the forest canopy. New approaches are therefore needed to generate wall-to-wall maps from the forest structural information collected at the GEDI footprint level. We study the feasibility of a data fusion approach between GEDI and Landsat data for wall-to-wall mapping of TSD, and we test the methodology on a ~52,000 ha study area located in the Nez Perce-Clearwater National Forest (Idaho, USA) where an extensive record of past forest management and fire disturbances is available, starting in 1870. GEDI data are simulated over the two-year programmed mission from airborne LiDAR point clouds. The simulated GEDI data are used for TSD estimation using a Random Forest classifier, trained with a sample of stands with known TSD, that were randomly sampled using a two-level stratification based on topographic and GEDI metrics. Single image Landsat-8 OLI (Operational Land Imager) data are used to segment the study area, obtaining image-objects needed for the spatial extrapolation of TSD from the GEDI footprints to forest stands. Throughout the study, we assess the influence in overall accuracy of the training dataset, the GEDI sampling grid of measurements, and observed TSD. The results show that the proposed GEDI-Landsat data fusion has the potential to reconstruct the long-term disturbance history of a temperate, even-aged forest which is a breakthrough to obtain global maps of the complete disturbance history of forests from remotely sensed data.

Introduction

Global and regional maps of forest stand age are required to improve carbon pools and flux estimates, and understand the impact of forest disturbances on net carbon accumulation (Pan et al., 2011; Pregitzer and Euskirchen, 2004; Pugh et al., 2019).

Available stand age datasets can be obtained from several sources such as field inventory and remotely sensed data. Forest inventories provide accurate ground-based data to assess forest age, but they are limited in tracking disturbances at large spatial scales. Optical satellite sensor data, in particular Landsat data, have so far been the best alternative to generate timely records of stand age (expressed as Time Since Disturbance, TSD) at large spatial scales through change detection and multi-temporal time series analysis (e.g., Hansen et al., 2008; Hayes and Sader, 2001; Huang et al., 2009; Huo et al., 2019; Kennedy et al., 2010; Lu et al., 2004; Masek et al., 2008; Schroeder et al., 2007). While these methods can provide spatially explicit information of disturbances at small time intervals (i.e., yearly based), they can only detect disturbances that have happened since the beginning of the Earth Observation data record which broadly began in the 1970s.

Active remotely sensed data sensitive to the three-dimensional structure of the forest canopy are increasingly used to estimate forest age as there exists a strong linkage between forest structure and growth (Monserud, 1984; Oliver and Larson, 1996; Ryan et al., 2004). In particular, Light Detection and Ranging (LiDAR) sensors record direct measurements of the forest canopy and are one of the most powerful remote sensing systems to describe forest structure (Goetz and Dubayah, 2011). LiDAR data are suitable to model a wide variety of forest structural attributes such as height, basal area, density, leaf area index, biomass and carbon stocks (e.g., Andersen et al., 2005; Boudreau et al., 2008; Hudak et al., 2006; Lefsky et al., 1999; Naesset, 1997; Nelson et al., 1988; Zhao and Popescu, 2009); and these attributes have explanatory power to estimate stand age, forest regrowth, forest succession, and TSD (Falkowski et al., 2009; Poulter et al., 2019; Racine et al., 2014; Sanchez-Lopez et al., 2019, in review; Zhang et al., 2014).

The deployment of LiDAR is dominated by airborne platforms, but largescale coverage of LiDAR is only attainable through satellite systems. The Geoscience Laser Altimeter System (GLAS), onboard the Ice Cloud and Land Elevation Satellite (ICESat), was the first sensor providing global LiDAR measurements from space (Zwally et al., 2002). GLAS collected ~250 million observations over forest regions from 2003 to 2009 (Lefsky, 2010), that were used in a variety of forest-related studies (Baccini et al., 2012; Duncanson et al., 2010; Lefsky, 2010; Montesano et al., 2013; Poulter et al., 2019; Simard et al., 2011). Two recently launched LiDAR spaceborne missions, ICESat-2 and the Global Ecosystem Dynamics Investigations (GEDI), are complementing this pioneer LiDAR spaceborne mission, and are collecting billions of measurements of the forest canopy. In particular, GEDI has been designed to monitor forest ecosystems and improve the understanding of forest carbon dynamics (Dubayah et al., 2014). With a two-year programmed mission, GEDI is recording data from

51.6° N to 51.6° S latitudes as constrained by the orbit of the International Space Station (ISS) where GEDI was mounted in December 2018.

Although spaceborne LiDAR missions, such as the GEDI, record global data of forest ecosystems, they don't provide complete horizontal coverage of measurements due to the sampling configuration of their instruments. The GEDI instrument is a multi-beam large-footprint waveform LiDAR composed of three laser transmitters that generate eight ground tracks; GEDI footprints of about 22 m diameter are spaced on the ground ~600 m across-track, and ~60 m along-track (Hancock et al., 2019). This makes it necessary to develop approaches that extend the forest structural information collected at the sensor footprint level across larger spatial scales. The footprint observations can be clustered, for instance, into cells of constant resolution (e.g., Baccini et al., 2012; Simard et al., 2011). However, the cell doesn't represent by itself a true geographical unit of analysis (Fisher, 1997), and its use might introduce large uncertainties into the analysis depending on cell size and landscape heterogeneity. Alternatively, footprint observations can be scaled up to an image object that represents a forest patch (Lefsky, 2010; Montesano et al., 2013). Geographic Object-Based Image Analysis (GEOBIA) carries out the delineation of the image objects through image segmentation procedures (Blaschke et al., 2008), for which spatially contiguous sensed data are required. Lefsky (2010), for instance, used object-based analysis to delineate forest patches using MODIS data to generate wall-to-wall canopy height maps from spaceborne GLAS data. GEDI will provide coverage of LiDAR data for tropical and temperate forests at a denser sampling than the ICESat missions. Therefore, data fusion object-based strategies between GEDI and data sources of moderate spatial resolution, such as Landsat, are worth exploring. Landsat provides global coverage—ideal for vegetation landscape mapping—and has an adequate spatial resolution (i.e., 30 m) for stand-level analysis at regional scales. Moreover, Landsat data have been used for image segmentation in studies related to the estimation of stand structure attributes such as biomass and TSD (Montesano et al., 2013; Wulder et al., 2004). We hypothesize that the data fusion of GEDI and Landsat can be suitable to map TSD at the stand level. However, the feasibility of the object-based data fusion approach would depend on the combined effect of the GEDI sampling grid, the quality of the delineation, and the size and spatial pattern of the disturbances.

In this study, we evaluate the feasibility of using GEDI data and image objects delineated on Landsat data for synoptic mapping of TSD. Landsat data are used for image segmentation and simulated GEDI data over the two-year programmed mission are used to estimate TSD using Random Forest (RF) analysis. The main goal was to test whether the proposed approach can be successfully used to reduce

the limitations of the GEDI sampling configuration to map stand-level TSD and whether it can provide comparable results to those obtained with airborne LiDAR (Sanchez-Lopez et al., 2019, in review). We investigate the scope of the proposed methodology by assessing the influence on overall accuracy of the (a) training dataset, (b) GEDI sampling grid of measurements, and (c) observed TSD.

Materials

Study area

The study area is in the Nez Perce-Clearwater National Forest in Idaho (USA) (Figure 3.1). It is a temperate mixed-conifer forest covering ~52,000 ha of the Clear Creek, Selway River, and Elk Creek watersheds. The study area is mountainous, with elevation ranging from ~400 m to 2000 m; and steep, with slopes often higher than 30%. Predominant tree species are Douglas-fir (*Pseudotsuga menziesii* (Mirb.) Franco.) and grand fir (*Abies grandis* (Dougl. Ex D. Don) Lindl.), often accompanied by ponderosa pine (*Pinus ponderosa* C. Lawson) and western redcedar (*Thuja plicata* Donn ex D.Don).

The forest landscape is a mosaic of even-aged stands result of systematic wildfires and harvests that have disturbed the study area since the 19th century (Morgan et al., 2017; USDA, Forest Service, 2016).

LiDAR and GEDI simulated data

Small-footprint discrete return airborne LiDAR data were acquired in October 2009 and June-July 2012 on the Clear Creek watershed and the Selway River and Elk Creek watersheds respectively. A Leica ALS60 instrument at 69,400 Hz pulse rate in a multi-pulse mode in the Clear Creek area and at 88,000 Hz in the Selway area was used. The average point density was at least 4 points/m^2 in both datasets.

Large-footprint LiDAR waveforms were simulated from the airborne LiDAR point clouds using the GEDI simulator that has been used for calibration of algorithms and assessment of GEDI mission accuracy (Blair and Hofton, 1999; Hancock et al., 2019). The waveforms were simulated on footprints of ~22 meters and distributed over the study area considering the GEDI sampling configuration and the orbit of the International Space Station (ISS), where GEDI is attached. The simulated grid of footprints contained 28,602 GEDI footprints, separated ~600 m across-track and ~60 m along-track (Hancock et al., 2019). The simulator was only allocated enough power to have it firing 60% of the time over the two-year programmed mission and accounted for data loss due to leaf-off conditions and 50% of cloud cover.

A total of 57 metrics were calculated from the simulated waveforms (Table 3.1).

Additionally, a raster grid at 30 m spatial resolution of the solar radiation aspect index ('SRAI'; Roberts and Cooper, 1989), a linear transformation of the topographic aspect, was obtained (equation 1):

$$\text{SRAI} = \frac{1-\cos\left(\left(\frac{\pi}{180}\right)(\alpha-30)\right)}{2} \quad (1)$$

where α is the topographic aspect in radians that was obtained from the airborne LiDAR point cloud using the FUSION software (McGaughey, 2009).

Landsat data and data processing

A cloud-free Landsat-8 scene (path 42 row 28) close in time (23rd of July 2013) to the airborne LiDAR surveys was acquired from the USGS Earth explorer (https://earthexplorer.usgs.gov). Landsat-8 was preferred over Landsat-5 and 7, both overlapping in time with the LiDAR acquisitions, because of the poor radiometric resolution of the TM instrument of Landsat-5, and the failure in 2003 of the Scan Line Corrector (SLC) of the Landsat-7 ETM+ sensor.

The Landsat multispectral data were pan-sharpened using the panchromatic band and the NNDifusse algorithm implemented in ENVI software (Sun et al., 2014). Tasseled Cap (TC) indices of Brightness (TCB), Greenness (TCG) and Wetness (TCW) were then calculated using the coefficients published in Baig et al. (2014) for the TC transformation based on Landsat-8 at-satellite reflectance data. The three indices were normalized between 0-100 applying a 2% linear stretch.

Ancillary reference data

Records of stand-replacing disturbances that have happened in the study area between 1870 and 2005 were available from two different data sources:

(1) the FACTS (Forest ACtivity Tracking System) timber harvest dataset which is maintained by the U.S. Forest Service and contains spatial and temporal records of planned and accomplished forest management activities, such as clearctus. It consists of polygon features with embedded metadata that include the fiscal year in which the activity was done. The dataset contained records since 1956 for the study area (USDA, Forest Service, 2016);

(2) a dataset of burned area perimeters of historical wildfires that occurred from 1870 to 2000, although 99.95% of them happened between 1870 and 1940. The fires were photo-interpreted using fire atlas data and historical aerial photographs (Morgan et al., 2017).

Both datasets were assembled together and manually refined to amend potential non-reported post-disturbances (e.g., small areas with evident biomass removal and other post-logging activity, especially within the fire perimeters) as described in Sanchez-Lopez et al., (2019, in review). TSD was calculated for each polygon from 2012, considered as the benchmark year based on the acquisition dates of the airborne LiDAR (used to simulate the GEDI data).

Twenty additional non-disturbed forest stands (i.e., disturbed before 1870) were digitized and visually photo-interpreted using NAIP imagery, the airborne LiDAR point clouds, and the ancillary reference datasets. The stands were characterized by dense canopy closure and relatively high height of the dominant cohort of the forest canopy. They were joined to the dataset to represent all the stand typologies of the study area, i.e., disturbed from 1870 and non-disturbed before 1870 (Figure 3.2).

Methods

In this study, TSD is estimated at the image object level using GEDI simulated data and image objects delineated from Landsat data. The overall workflow is divided into four main steps: (1) image segmentation using the Landsat Tasseled Cap (TC) derived indices, seeking an optimal segmentation where the image objects are homogenous in terms of forest structure (and potentially are representing even-aged stands); (2) training data selection through stratified random sampling to extract data of known TSD to train a RF classifier; (3) TSD estimation at the GEDI footprint and image object levels; and (4) accuracy assessment (Figure 3.3).

Throughout the study, we evaluate the sensitivity of the results to the:

(1) sample size of the training dataset. TSD reference data (particularly of mature and old forest stands) are often not available and their collection requires expensive and time-consuming procedures (e.g., dendrochronology analysis);
(2) observed TSD. TSD estimation using forest structural related data becomes progressively more complex as the uneven-aged distribution of the forest canopy is reached. This analysis will provide insight into the temporal scope of the methodology.
(3) GEDI sampling grid. The number of GEDI footprints available to estimate TSD within each image object would depend on the image object size and the distribution of the sample grid.

Landsat segmentation

Landsat image segmentation was performed using the multiresolution segmentation algorithm (Baatz and Schape, 2000) implemented in eCognition 9.1 software. TC indices were the input data for segmentation since they are more correlated to successional stages and recent disturbances (particularly the TCW) compared to other Landsat derived indices (Cohen et al., 1995; Cohen and Spies, 1992; Jin and Sader, 2005); and have been previously used for segmentation of forest patches in studies related to the estimation of forest structural parameters such as biomass or TSD (Montesano et al., 2013; Wulder et al., 2004).

Several segmentations varying the MRS algorithm parameters and the input layers were obtained. A two-stage object-based evaluation strategy was followed to select a segmentation output (Sanchez-Lopez et al., 2018). Object-based segmentation evaluations were implemented in GEOBIA to assess the quality of the segmented outputs. They can be used to objectively select among input data, segmentation algorithms and algorithm parameters (Costa et al., 2018; Georganos et al., 2018; Grybas et al., 2017; Johnson and Xie, 2011; Sanchez-Lopez et al., 2018). The first stage of the evaluation used here is based on an unsupervised evaluation that measures intra-segment homogeneity and inter-segment heterogeneity through spatial autocorrelation statistics (Böck et al., 2017; Espindola et al., 2006; Johnson and Xie, 2011). These measures are calculated from the Landsat TC indices that were used as input for segmentation. This step allowed for calibration of the parameters of the multiresolution segmentation algorithm. The second stage is a supervised evaluation, i.e., it depends on external reference data to evaluate over and undersegmentation. Oversegmentation happens when multiple image objects are corresponding to a single geographic object; undersegmentation happens when an image object corresponds to more than one geographic object. Over and undersegmetnation were calculated by pairwise comparing the image objects of the segmentation outputs to reference objects representing actual even-aged forest stands (Clinton et al., 2010). This stage allowed for properly setting the weights assigned to each of the TC indices for the segmentation. For a more detailed explanation of the two-stage evaluation strategy followed to select a segmentation refer to Sanchez-Lopez et al. (2018).

The image objects of the selected segmentation that were smaller than 2 ha, which is commonly used as a threshold between stand and patch forest management units in areas of the Pacific Northwest (USDA, Forest Service, 2016), were dissolved into larger objects based on the statistics of the TC indices.

Training dataset

A subset of 630 image objects totaling 16,062 ha (Table 3.2) was extracted from the segmentation and used as candidates for training. These image objects met two conditions: (1) they overlapped at least 75% of their area with the ancillary reference dataset (Figure 3.2); and (2) they enclosed at least one GEDI footprint within their perimeters.

The training dataset of image objects of known TSD was extracted from the previous subset through stratified random sampling using the 'SRAI' topographic metric and a canopy-height GEDI metric ('rhInfl98') as stratification variables. 'SRAI' was selected because it is related to solar insolation: 'SRAI' ranges between 0 and 1; lower values represent cooler and moister areas that are north-northeast oriented, and higher values represent warmer and drier areas that are south-southwest oriented. The 'rhInfl98' GEDI derived metric (Table 3.1), a canopy height metric that represents the upper layer of the forest canopy, was selected as a second stratification variable considering the strong linkage between stand height and age (i.e., TSD) (Racine et al., 2014).

For each image object of known TSD, mean values of the 'SRAI' and 'rhInfl98' were calculated from the GEDI footprints that were fully enclosed within their perimeters. 'SRAI' was extracted for each footprint location from the 30 m raster grid (see "LiDAR and GEDI simulated data" section). The 'rhInfl98' was the 98% relative height metric derived from the simulated GEDI waveforms (Table 3.1), a metric representing the dominant cohort of the forest canopy (Lefsky et al., 2005).

Two 'SRAI' strata (xeric/humid) of equal size were defined, using the median 'SRAI' of the image objects of known TSD as a benchmark. Within each 'SRAI' stratum, five 'rhInfl98' strata were defined, using the quintiles of the average 'rhInfl98' distribution. As a result, ten strata of equal size were identified (Figure 3.4).

One thousand datasets were generated to assess the sensitivity of the size of the training data on the TSD estimation (see below). Accordingly, we randomly selected from 1 to 10 image objects per each of the defined strata (Figure 3.4), and we repeated the extraction 100 times for each sampled size.

TSD estimation

The 'yaimpute' package within the R software (Crookston and Finley, 2008) was used to train a RF classifier and predict TSD at the GEDI footprint level. The training data used in the RF consisted the GEDI footprint observations fully enclosed within the perimeters of the sampled image objects (Figure 3.4). The TSD, as observed in the ancillary reference data, was the dependent variable and the 57 GEDI derived metrics of the simulated GEDI waveforms were the predictor variables (Table 3.1). The number of decision trees was set at 500, and the number of predictor variables available to split at

each tree node was 7. Once the RF classifier was trained, TSD was imputed to the grid of GEDI simulated footprints.

TSD at the image object level was calculated as the median value of the TSD predictions of the GEDI footprints fully enclosed within each image object.

Accuracy metrics

Accuracy of the predictions was assessed at the image object level using three accuracy metrics, defined as follows:

The Root Mean Square Difference between predicted and observed TSD (RMSD):

$$RMSD = \sqrt{\frac{\sum_{i=1}^{n}(\hat{Y}_i - Y_i)^2}{n}} \; ; \tag{2}$$

where *n* is the number of image objects; $\hat{Y}_i$ is the predicted TSD value of the image object *i*; and Y_i is the observed TSD value of the image object *i*.

The bias (BIAS):

$$BIAS = \frac{1}{n}\sum_{i=1}^{n}(\hat{Y}_i - Y_i) \tag{3}$$

where *n* is the number of GEDI image objects; $\hat{Y}_i$ is the predicted TSD value of the image object *i*; and Y_i is the observed TSD value of the image object *i*.

And the percentage of forest stands that had less than 10 years of absolute error (Perct.10):

$$Perct.10 = \left(\frac{\sum_{i=1}^{n}\left|\hat{Y}_i - Y_i\right| < 10}{n}\right) x100 \tag{4}$$

where *n* is the number of GEDI image objects; $\hat{Y}_i$ is the predicted TSD value of the image object *i*; and Y_i is the observed TSD value of the image object *i*.

The validation dataset used to compute these metrics comprised the image objects of known TSD that were not used for training (Table 3.2). The image objects overlapping with the visually photo-interpreted non-disturbed forest stands (i.e., non-disturbed after 1870) (Figure 3.2) were also excluded because their age was unknown.

Influence of TSD and GEDI sampling

The sensitivity of the accuracy metrics to TSD, as observed in the ancillary dataset, and to the GEDI sampling configuration was further investigated. For that, the 100 TSD imputations obtained using the random extractions of training data with five sampled image objects were considered (see "Training dataset" section). $RMSD$, $BIAS$, and Perct.10 calculated for the image objects disturbed at the different disturbance decades were evaluated. Accuracy of the TSD predictions was also evaluated for the image objects that enclosed from 1 to 10 GEDI footprints.

Results

Landsat segmentation

The selected segmentation was composed of 2,060 image objects of 25.5 ha average size (Figure 3.5). The segmentation was obtained including the three TC indices in the multiresolution segmentation algorithm in eCognition with double weight assigned to the TCW.

A total of 22,603 GEDI footprints out of the 28,602 originally simulated over the study area (Figure 3.1) were fully enclosed within the perimeters of the image objects of the segmentation (Figure 3.5). The percentage of objects enclosing at least one GEDI footprint was 87.5% (that represent 95.3% of the study area); 61.1% of image objects fully enclosed at least five GEDI footprints (that represent 82.5% of the study area); and 40.7% of images objects fully enclosed at least ten GEDI footprints (that represent 66.2% of the study area) (Figure 3.6).

Training dataset

Out of the 1000 random extractions of training data, the minimum amount of fully enclosed GEDI footprints within the sampled objects was 47 (sampling one image object per stratum) and the maximum was 1427 (sampling ten image objects per stratum).

Overall accuracy at the image object level was slightly influenced by the number of training image objects provided that a minimum was sampled per stratum (Figure 3.7). Perct.10 reflected well that trend suggesting that around four image objects would be necessary to assure that more of the 50% of the image objects are classified within 10 years of absolute error. Conversely, the variation in training data had an influence on the overall accuracy, as reflected especially on the larger range interquartile of the RMSD, BIAS and Pert.10 obtained with the same sample size in the 100 replicated iterations.

TSD estimation

We mapped TSD at the image object level for one of the instances that sampled five image objects per stratum on the stratification. The number of GEDI footprints fully enclosed in the 50 sampled image objects was 621 (Table 3.3). The RMSD was 21.4 years, BIAS was -4.47 years and the percentage of

stands with less than 10 years of absolute error (Perct.10) was 55.6%. When considering the image objects disturbed since the decade of 1910 (TSD <102 years), RMSD was 16.9 years, BIAS was 0.97 years and the Perct.10 was 65.4%.

Figure 3.8 shows an illustrative example of the predictions at the GEDI footprint level and how they overlay on the Landsat segmentation; and Figure 3.9 shows the (almost) wall-to-wall map of TSD of the study area.

The confusion matrix of the TSD predictions at the image object level per decade (Table 3.4) shows that confusion in the predictions happened between decades close in time for the most recent disturbances. For instance, 27 image objects disturbed in the decade of the 1970s were classified as disturbed in the decade of the 1960s, and 21 image objects disturbed in the decade of the 1990s were classified as disturbed in the decade of the 1970s.

The area reported as disturbed in the 1910s (especially after the large fire of 1919) was ~19% of the study area (Table 3.2). Therefore, this decade was largely represented in the training data, and in the predictions. The confusion matrix shows that areas disturbed more than 100 years ago were often classified as disturbed in 1910, as well as areas disturbed in the 1930s.

Influence of TSD and GEDI sampling

The predictions were biased at the beginning of the time series (i.e., 1870 and 1880) and at the end (i.e., 1990 and 2000) (Figure 3.10). Nevertheless, the case of 2000 was expected since only one image object was available for training and validation. The decades with fewer reference data were prone to not be represented in the training dataset, thus, image objects disturbed within these decades were often misclassified, as observed in the Perct.10. Both $RMSD$ and $BIAS$ were relatively stable from 1910 to 1990, with larger interquartile range when the number of image objects in the dataset was small (i.e., 1920, 1940 or 1950) (Figure 3.10).

The number of GEDI footprints per image object slightly influenced the overall accuracy of the predictions (Figure 3.11). The likelihood of accurately classifying an image object within ten years of absolute error (Perct.10) was relatively similar with one to three footprints per object. Moreover, there was not an overall improvement in the predictions when the number of GEDI footprints significantly increased.

Discussion and Conclusions

Spaceborne LiDAR systems provide global structural data of forest ecosystems, but their configuration as sampling instruments makes it necessary to develop approaches that extend the information collected at the footprint level across larger spatial scales, for instance, through data fusion strategies. This research has studied the feasibility of using GEDI data and image objects delineated from Landsat imagery to effectively map TSD. For that, GEDI data simulated from airborne LiDAR point clouds have been used (Hancock et al., 2019).

Upscaling footprint estimates using Landsat derived image objects overcomes the limitations of the GEDI sampling configuration to map TSD at the stand-level. As opposed to the use of cells of constant size while using spaceborne LiDAR data (e.g., 1 km, 500 m) (Baccini et al., 2012, 2008; Simard et al., 2011), the use of image objects is adequate to map forest attributes that are marginally variable over the whole stand, such as TSD. The image object, as defined here, related to a homogenous structural forest patch that ideally is even-aged. Thus, the footprints enclosed within the same object represent canopy structures of similar TSD. GEDI will provide a relatively dense grid of canopy measurements after the two-year programmed mission and, as shown here, its combination with a Landsat segmentation provides a means to map TSD: 87.5% of the image objects (~95% of the study area) would enclose, at least, one GEDI footprint (Figure 3.6). We expect this area to remain under the 5% threshold. The simulation of GEDI data was conservative accounting for data loss due to leaf-off conditions and assuming 50% cloud cover.

This research builds upon the study of Sanchez-Lopez et al. (2019, in review) that combined airborne LiDAR data, object-based, and RF analysis to predict stand-level TSD in the same study area. Overall accuracy obtained in this study—RMSD= 21.4 years, BIAS= -4.47 and Perct.10= 55.6%—is relatively lower compared to the former study—RMSD= 17.5 years, BIAS= 0.8 years and Perct.10= 72.8%. This difference (especially noticeable in BIAS and Perct.10) is explained by the large disparity between the number of GEDI footprints (~22 m in diameter) and the cells (at 30 m resolution) of the rasterized derived airborne LiDAR metrics: the GEDI footprints cover only ~2% of the study area while the airborne LiDAR point clouds provided a complete coverage with return density of at least 4 points/m^2. Yet the difference of image objects that were classified less than 10 years apart of the reference TSD within the last 100 years is only 13% between the two studies (65% versus 78%). This preliminary analysis suggests that comparable accuracies could be achieved predicting TSD in young and mature forests through GEDI-Landsat data fusion. Nevertheless, more research is needed: the

methodology followed in both studies was similar, but the particulars of the GEDI and the Landsat datasets enforce a tailored methodology in the segmentation and training data selection.

Landsat data have an adequate spatial resolution (i.e., 30 m) to detect typical forest management units such as forest stands. Nevertheless, it is well established that the use of Landsat for analyses of forest structure is limited under dense canopies (Cohen et al., 1995; Turner et al., 1999). Besides this, there is an asymptotic relationship between stand age and variables derived from optical data that confounds differentiation of forest stands of different ages (Fiorella and Ripple, 1993). Thus, a degree of mismatch between the perimeters of the image objects and the actual forest stands was expected, especially in stands disturbed long ago (i.e., TSD>100 years). On the other hand, the object-based two-stage evaluation strategy followed to select a segmentation output (Sanchez-Lopez et al., 2018) was expressly designed for even-aged forest stand delineation using single metrics derived from airborne LiDAR data; therefore, more research is needed to adjust it to a Landsat-based workflow.

The accuracy of the TSD predictions is influenced by the training dataset that depends on the random sampling of the stratification (Figure 3.7). Following Sanchez-Lopez et al. (2019, in review), the stratification was based on topographic and canopy height related metrics. Therefore, a priori information on the distribution of TSD over the complete study area was not required, which would facilitate deployment of the approach in other study sites. The training set should represent the fullest range of TSD in a proportional way, but that depends on (1) the amount of sampled image objects, (2) how thoroughly the objects represent even-aged and homogenous structures (dependable on the segmentation), and (3) the amount of available reference data (Table 3.2). In this sense, it would be recommended to adjust the stratification, for instance, by sampling more intensively some specific stratum or using alternative stratification variables.

On the other hand, the GEDI sampling configuration that determines the number of footprints measurements enclosed within the image objects doesn't have a conclusive influence on the accuracy of the predictions. Figure 3.11 shows that the accuracy of the predictions is slightly influenced by the number of GEDI footprints enclosed within each image object, although a minimum of three measurements per image object would be recommended. Other factors such as the structural development of the forest represented by the image object, the actual age of the patches, or the distribution of the footprints might be more important. It would be expected, for instance, that the estimation of TSD in stands that are young and have little canopy variability requires fewer observations compared to the estimation of TSD in older stands that have uneven canopy structures

(Dubayah et al., 2010). Based on that, future research will involve a deeper analysis to understand the interaction between image object size, observed TSD and number of GEDI footprints.

The confusion matrix (Table 3.4) and the accuracy metrics show errors in predicting TSD that are over the decadal level. As an example, areas that have undergone wildfires during the decade of the 1910s (in which fires mainly happened in 1919), or the 1930s (in which fires mainly happened in 1931) displayed heterogeneous structures, which might have resulted from differences on vegetation recovery rates, site conditions, post-disturbance management, or disturbance severities. Consequently, stands disturbed in 1919 sometimes showed similar structural development to stands disturbed in 1931 (and vice versa) and misclassifications among these times were expected. This error pattern was also discussed in Sanchez-Lopez et al. (2019, in review), but it got accentuated using the GEDI discrete grid of measurements to estimate TSD over the whole stand. In short, the estimation of TSD in relatively old stands is more prone to misclassifications. Forests undisturbed for long periods achieve uneven-aged structures as canopy gaps become filled with younger trees (Luyssaert et al., 2008). The distribution of a limited number of GEDI footprints within these stands would result in classification errors if the footprints fall upon the gaps with younger, regenerating trees. In view of these results, Landsat-GEDI data fusion might be appropriate to characterize stand development through forest succession. Successional stages are related to TSD and stand age, but the classification often spans over larger time intervals than a decade; moreover, they describe stand development according to structural complexity, an intrinsic property of the vegetation recovery rates and site conditions.

Datasets of stand level disturbance history of forest ecosystems and forest stand age are required to fully understand global carbon cycle dynamics and assess the role of forests in the mitigation of climate change. Forest vertical structural data provide a means to accurately reconstruct the long-term history of stand-replacing disturbances. Data fusion between GEDI and Landsat, as proposed in this study, can be used to map TSD at the stand level especially in areas disturbed within the last 100 years. However, the delineation of the image objects, the stratification procedure to extract training data, and the disturbance patterns of the study area should be carefully considered as they influence the accuracy of the predictions.

Acknowledgements

I would like to thank to the GEDI science team for the simulation of the GEDI data from airborne LiDAR. The project is supported by NASA's Land-Cover/Land-Use Change (LCLUC) program

(award number NHX14AD92G) and the Carbon Monitoring System (CMS) (award number NNH15AZ06I), and by USDA NIFA grant 2011-32100-06016.

References

Andersen, H.-E., McGaughey, R.J., Reutebuch, S.E., 2005. Estimating forest canopy fuel parameters using LIDAR data. Remote Sens. Environ. 94, 441–449. https://doi.org/10.1016/j.rse.2004.10.013

Baatz, M., Schape, A., 2000. Multiresolution Segmentation–an optimization approach for high quality multi-scale image segmentation. AGIT-Symposium Salzburg 2000, 12–23.

Baccini, A., Goetz, S.J., Walker, W.S., Laporte, N.T., Sun, M., Sulla-Menashe, D., Hackler, J., Beck, P.S.A., Dubayah, R., Friedl, M.A., 2012. Estimated carbon dioxide emissions from tropical deforestation improved by carbon-density maps. Nat. Clim. Change 2, 182.

Baccini, A., Laporte, N., Goetz, S.J., Sun, M., Dong, H., 2008. A first map of tropical Africa's above-ground biomass derived from satellite imagery. Environ. Res. Lett. 3, 045011. https://doi.org/10.1088/1748-9326/3/4/045011

Baig, M.H.A., Zhang, L., Shuai, T., Tong, Q., 2014. Derivation of a tasselled cap transformation based on Landsat 8 at-satellite reflectance. Remote Sens. Lett. 5, 423–431.

Blair, J.B., Hofton, M.A., 1999. Modeling laser altimeter return waveforms over complex vegetation using high-resolution elevation data. Geophys. Res. Lett. 26, 2509–2512. https://doi.org/10.1029/1999GL010484

Blaschke, T., Lang, S., Hay, G., 2008. Object-Based Image Analysis: Spatial Concepts for Knowledge-Driven Remote Sensing Applications. Springer Science & Business Media.

Böck, S., Immitzer, M., Atzberger, C., 2017. On the Objectivity of the Objective Function—Problems with Unsupervised Segmentation Evaluation Based on Global Score and a Possible Remedy. Remote Sens. 9, 769. https://doi.org/10.3390/rs9080769

Boudreau, J., Nelson, R.F., Margolis, H.A., Beaudoin, A., Guindon, L., Kimes, D.S., 2008. Regional aboveground forest biomass using airborne and spaceborne LiDAR in Québec. Remote Sens. Environ. 112, 3876–3890. https://doi.org/10.1016/j.rse.2008.06.003

Clinton, N., Holt, A., Scarborough, J., Yan, L.I., Gong, P., others, 2010. Accuracy assessment measures for object-based image segmentation goodness. Photogramm. Eng. Remote Sens. 76, 289–299.

Cohen, W.B., Spies, T.A., 1992. Estimating structural attributes of Douglas-fir/western hemlock forest stands from Landsat and SPOT imagery. Remote Sens. Environ. 41, 1–17.

Cohen, W.B., Spies, T.A., Fiorella, M., 1995. Estimating the age and structure of forests in a multi-ownership landscape of western Oregon, U.S.A. Int. J. Remote Sens. 16, 721–746. https://doi.org/10.1080/01431169508954436

Costa, H., Foody, G.M., Boyd, D.S., 2018. Supervised methods of image segmentation accuracy assessment in land cover mapping. Remote Sens. Environ. 205, 338–351. https://doi.org/10.1016/j.rse.2017.11.024

Crookston, N.L., Finley, A.O., 2008. yaImpute: an R package for kNN imputation.

Dubayah, R., Goetz, S.J., Blair, J.B., Fatoyinbo, T.E., Hansen, M., Healey, S.P., Hofton, M.A., Hurtt, G.C., Kellner, J., Luthcke, S.B., Swatantran, A., 2014. The Global Ecosystem Dynamics Investigation. AGU Fall Meet. Abstr. 14.

Dubayah, R.O., Sheldon, S.L., Clark, D.B., Hofton, M.A., Blair, J.B., Hurtt, G.C., Chazdon, R.L., 2010. Estimation of tropical forest height and biomass dynamics using lidar remote sensing at La Selva, Costa Rica. J. Geophys. Res. Biogeosciences 115. https://doi.org/10.1029/2009JG000933

Duncanson, L.I., Niemann, K.O., Wulder, M.A., 2010. Estimating forest canopy height and terrain relief from GLAS waveform metrics. Remote Sens. Environ. 114, 138–154. https://doi.org/10.1016/j.rse.2009.08.018

Espindola, G.M., Camara, G., Reis, I.A., Bins, L.S., Monteiro, A.M., 2006. Parameter selection for region-growing image segmentation algorithms using spatial autocorrelation. Int. J. Remote Sens. 27, 3035–3040. https://doi.org/10.1080/01431160600617194

Falkowski, M.J., Evans, J.S., Martinuzzi, S., Gessler, P.E., Hudak, A.T., 2009. Characterizing forest succession with lidar data: An evaluation for the Inland Northwest, USA. Remote Sens. Environ. 113, 946–956. https://doi.org/10.1016/j.rse.2009.01.003

Fiorella, M., Ripple, W.J., 1993. Determining Successional Stage of Temperate Coniferous Forests with Landsat Satellite Data. Photogramm. Eng. Remote Sens. U. S. 59:2.

Fisher, P., 1997. The pixel: A snare and a delusion. Int. J. Remote Sens. 18, 679–685. https://doi.org/10.1080/014311697219015

Georganos, S., Lennert, M., Grippa, T., Vanhuysse, S., Johnson, B., Wolff, E., 2018. Normalization in Unsupervised Segmentation Parameter Optimization: A Solution Based on Local Regression Trend Analysis. Remote Sens. 10, 222. https://doi.org/10.3390/rs10020222

Goetz, S., Dubayah, R., 2011. Advances in remote sensing technology and implications for measuring and monitoring forest carbon stocks and change. Carbon Manag. 2, 231–244. https://doi.org/10.4155/cmt.11.18

Grybas, H., Melendy, L., Congalton, R.G., 2017. A comparison of unsupervised segmentation parameter optimization approaches using moderate-and high-resolution imagery. GIScience Remote Sens. 54, 515–533.

Hancock, S., Armston, J., Hofton, M., Sun, X., Tang, H., Duncanson, L.I., Kellner, J.R., Dubayah, R., 2019. The GEDI simulator: A large-footprint waveform lidar simulator for calibration and validation of spaceborne missions. Earth Space Sci. 0. https://doi.org/10.1029/2018EA000506

Hansen, M.C., Stehman, S.V., Potapov, P.V., Loveland, T.R., Townshend, J.R.G., DeFries, R.S., Pittman, K.W., Arunarwati, B., Stolle, F., Steininger, M.K., Carroll, M., DiMiceli, C., 2008. Humid tropical forest clearing from 2000 to 2005 quantified by using multitemporal and multiresolution remotely sensed data. Proc. Natl. Acad. Sci. 105, 9439–9444. https://doi.org/10.1073/pnas.0804042105

Hayes, D.J., Sader, S.A., 2001. Comparison of change-detection techniques for monitoring tropical forest clearing and vegetation regrowth in a time series. Photogramm. Eng. Remote Sens. 67, 1067–1075.

Huang, C., Goward, S.N., Masek, J.G., Gao, F., Vermote, E.F., Thomas, N., Schleeweis, K., Kennedy, R.E., Zhu, Z., Eidenshink, J.C., Townshend, J.R.G., 2009. Development of time series stacks of Landsat images for reconstructing forest disturbance history. Int. J. Digit. Earth 2, 195–218. https://doi.org/10.1080/17538940902801614

Hudak, A.T., Crookston, N.L., Evans, J.S., Falkowski, M.J., Smith, A.M., Gessler, P.E., Morgan, P., 2006. Regression modeling and mapping of coniferous forest basal area and tree density from discrete-return lidar and multispectral satellite data. Can. J. Remote Sens. 32, 126–138.

Huo, L.-Z., Boschetti, L., Sparks, A.M., 2019. Object-Based Classification of Forest Disturbance Types in the Conterminous United States. Remote Sens. 11, 477. https://doi.org/10.3390/rs11050477

Jin, S., Sader, S.A., 2005. Comparison of time series tasseled cap wetness and the normalized difference moisture index in detecting forest disturbances. Remote Sens. Environ. 94, 364–372. https://doi.org/10.1016/j.rse.2004.10.012

Johnson, B., Xie, Z., 2011. Unsupervised image segmentation evaluation and refinement using a multi-scale approach. ISPRS J. Photogramm. Remote Sens. 66, 473–483. https://doi.org/10.1016/j.isprsjprs.2011.02.006

Kennedy, R.E., Yang, Z., Cohen, W.B., 2010. Detecting trends in forest disturbance and recovery using yearly Landsat time series: 1. LandTrendr — Temporal segmentation algorithms. Remote Sens. Environ. 114, 2897–2910. https://doi.org/10.1016/j.rse.2010.07.008

Lefsky, M.A., 2010. A global forest canopy height map from the Moderate Resolution Imaging Spectroradiometer and the Geoscience Laser Altimeter System. Geophys. Res. Lett. 37. https://doi.org/10.1029/2010GL043622

Lefsky, M.A., Cohen, W.B., Acker, S.A., Parker, G.G., Spies, T.A., Harding, D., 1999. Lidar Remote Sensing of the Canopy Structure and Biophysical Properties of Douglas-Fir Western Hemlock Forests. Remote Sens. Environ. 70, 339–361. https://doi.org/10.1016/S0034-4257(99)00052-8

Lefsky, M.A., Hudak, A.T., Cohen, W.B., Acker, S.A., 2005. Geographic variability in lidar predictions of forest stand structure in the Pacific Northwest. Remote Sens. Environ. 95, 532–548. https://doi.org/10.1016/j.rse.2005.01.010

Lefsky, M.A., Keller, M., Pang, Y., Camargo, P.B. de, Hunter, M.O., 2007. Revised method for forest canopy height estimation from Geoscience Laser Altimeter System waveforms. J. Appl. Remote Sens. 1, 013537. https://doi.org/10.1117/1.2795724

Lu, D., Mausel, P., Brondízio, E., Moran, E., 2004. Change detection techniques. Int. J. Remote Sens. 25, 2365–2401.

Luyssaert, S., Schulze, E.-D., Börner, A., Knohl, A., Hessenmöller, D., Law, B.E., Ciais, P., Grace, J., 2008. Old-growth forests as global carbon sinks. Nature 455, 213–215. https://doi.org/10.1038/nature07276

Masek, J.G., Huang, C., Wolfe, R., Cohen, W., Hall, F., Kutler, J., Nelson, P., 2008. North American forest disturbance mapped from a decadal Landsat record. Remote Sens. Environ. 112, 2914–2926. https://doi.org/10.1016/j.rse.2008.02.010

McGaughey, R.J., 2009. FUSION/LDV: Software for LIDAR data analysis and visualization. US Dep. Agric. For. Serv. Pac. Northwest Res. Stn. Seattle WA USA 123.

Monserud, R.A., 1984. Height Growth and Site Index Curves for Inland Douglas-fir Based on Stem Analysis Data and Forest Habitat Type. For. Sci. 30, 943–965. https://doi.org/10.1093/forestscience/30.4.943

Montesano, P.M., Cook, B.D., Sun, G., Simard, M., Nelson, R.F., Ranson, K.J., Zhang, Z., Luthcke, S., 2013. Achieving accuracy requirements for forest biomass mapping: A spaceborne data fusion method for estimating forest biomass and LiDAR sampling error. Remote Sens. Environ. 130, 153–170. https://doi.org/10.1016/j.rse.2012.11.016

Morgan, P., Hudak, A.T., Wells, A., Parks, S.A., Baggett, L.S., Bright, B.C., Green, P., 2017. Multidecadal trends in area burned with high severity in the Selway-Bitterroot Wilderness Area 1880–2012. Int. J. Wildland Fire 26, 930–943.

Naesset, E., 1997. Determination of mean tree height of forest stands using airborne laser scanner data. ISPRS J. Photogramm. Remote Sens. 52, 49–56.

Nelson, R., Krabill, W., Tonelli, J., 1988. Estimating forest biomass and volume using airborne laser data. Remote Sens. Environ. 24, 247–267. https://doi.org/10.1016/0034-4257(88)90028-4

Oliver, C.D., Larson, B.C., 1996. Forest stand dynamics: updated edition. John Wiley and sons.

Pan, Y., Chen, J.M., Birdsey, R., McCullough, K., He, L., Deng, F., 2011. Age structure and disturbance legacy of North American forests. Biogeosciences 8 715-732 8, 715–732. https://doi.org/10.5194/bg-8-715-2011

Poulter, B., Aragão, L., Andela, N., Bellassen, V., Ciais, P., Kato, T., Lin, X., Nachin, B., Luyssaert, S., Pederson, N., Peylin, P., Piao, S., Pugh, T., Saatchi, S., Schepaschenko, D., Schelhaas, M., Shivdenko, A., 2019. The global forest age dataset and its uncertainties (GFADv1.1). NASA Natl. Aeronaut. Space Adm. https://doi.org/10.1594/PANGAEA.897392

Pregitzer, K.S., Euskirchen, E.S., 2004. Carbon cycling and storage in world forests: biome patterns related to forest age. Glob. Change Biol. 10, 2052–2077. https://doi.org/10.1111/j.1365-2486.2004.00866.x

Pugh, T.A., Lindeskog, M., Smith, B., Poulter, B., Arneth, A., Haverd, V., Calle, L., 2019. Role of forest regrowth in global carbon sink dynamics. Proc. Natl. Acad. Sci. 116, 4382–4387.

Racine, E.B., Coops, N.C., St-Onge, B., Bégin, J., 2014. Estimating Forest Stand Age from LiDAR-Derived Predictors and Nearest Neighbor Imputation. For. Sci. 60, 128–136. https://doi.org/10.5849/forsci.12-088

Roberts, D.W.U.S.U., Cooper, S.V., 1989. Concepts and techniques of vegetation mapping. Gen. Tech. Rep. INT - US Dep. Agric. For. Serv. Intermt. Res. Stn. USA.

Ryan, M.G., Binkley, D., Fownes, J.H., Giardina, C.P., Senock, R.S., 2004. An Experimental Test of the Causes of Forest Growth Decline with Stand Age. Ecol. Monogr. 74, 393–414. https://doi.org/10.1890/03-4037

Sanchez-Lopez, N., Boschetti, L., Hudak, A., 2018. Semi-Automated Delineation of Stands in an Even-Age Dominated Forest: A LiDAR-GEOBIA Two-Stage Evaluation Strategy. Remote Sens. 10, 1622. https://doi.org/10.3390/rs10101622

Sanchez-Lopez, N., Boschetti, L., Hudak, A.T., 2019. Reconstruction of the disturbance history of a temperate coniferous forest through stand-level analysis of airborne LiDAR data. Manuscript submitted for publication.

Schroeder, T.A., Cohen, W.B., Yang, Z., 2007. Patterns of forest regrowth following clearcutting in western Oregon as determined from a Landsat time-series. For. Ecol. Manag. 243, 259–273. https://doi.org/10.1016/j.foreco.2007.03.019

Simard, M., Pinto, N., Fisher, J.B., Baccini, A., 2011. Mapping forest canopy height globally with spaceborne lidar. J. Geophys. Res. Biogeosciences 116.

Sun, W., Chen, B., Messinger, D., 2014. Nearest-neighbor diffusion-based pan-sharpening algorithm for spectral images. Opt. Eng. 53, 013107.

Turner, D.P., Cohen, W.B., Kennedy, R.E., Fassnacht, K.S., Briggs, J.M., 1999. Relationships between Leaf Area Index and Landsat TM Spectral Vegetation Indices across Three Temperate Zone Sites. Remote Sens. Environ. 70, 52–68. https://doi.org/10.1016/S0034-4257(99)00057-7

USDA, Forest Service, 2016. Forest Service Activity Tracking System (FACTs) harvest database. URL http://data.fs.usda.gov/geodata/edw/datasets.php

Wulder, M.A., Skakun, R.S., Kurz, W.A., White, J.C., 2004. Estimating time since forest harvest using segmented Landsat ETM+ imagery. Remote Sens. Environ. 93, 179–187. https://doi.org/10.1016/j.rse.2004.07.009

Zhang, C., Ju, W., Chen, J.M., Li, D., Wang, X., Fan, W., Li, M., Zan, M., 2014. Mapping forest stand age in China using remotely sensed forest height and observation data. J. Geophys. Res. Biogeosciences 119, 1163–1179. https://doi.org/10.1002/2013JG002515

Zhao, K., Popescu, S., 2009. Lidar-based mapping of leaf area index and its use for validating GLOBCARBON satellite LAI product in a temperate forest of the southern USA. Remote Sens. Environ. 113, 1628–1645. https://doi.org/10.1016/j.rse.2009.03.006

Zwally, H.J., Schutz, B., Abdalati, W., Abshire, J., Bentley, C., Brenner, A., Bufton, J., Dezio, J., Hancock, D., Harding, D., 2002. ICESat's laser measurements of polar ice, atmosphere, ocean, and land. J. Geodyn. 34, 405–445.

Table 3.1. Fifty-seven summary metrics calculated from the simulated GEDI waveforms (Hancock et al., 2019).

	Predictor variables
inflGround	Ground elevation (m) from inflection points.
rhInfl 0-100	Relative height (rh) metrics, ranging from 0%-100% and computed at 2% steps, using ground from inflection points (m)
maxHalfCov	Canopy cover (fraction) from double the energy beneath the lowest maximum ground
infHalfCov	Canopy cover (fraction) from double the energy beneath the inflection point ground
Leading edge extent	Leading edge extent (m), related to the slope (Lefksy et al., 2007)
Trailing edge extent	Trailing edge extent (m), related to canopy elevation (Lefksy et al., 2007)
BlairSense	Blair's sensitivity metric. Canopy cover at which this SNR would have 90% chance of detecting ground

Table 3.2. Disturbed area reported on the ancillary reference dataset (Figure 3.2) and on the selected image objects of known TSD summarized by decade. The image objects overlapped 75% of their area with the ancillary reference dataset and enclosed at least one GEDI footprint. The area is reported in number of disturbed hectares, and in percentage relative to the extent of the entire study area. ND: forest stands non-disturbed since 1870.

	Ancillary reference dataset		**Image objects of known TSD**		
Disturbance Decade	**Area (ha)**	**Relative area (%)**	**Area (ha)**	**Relative area (%)**	**# objects**
ND	2429	4.63	1368	2.61	39
1870	1199	2.28	388	0.74	10
1880	5509	10.5	2410	4.59	80
1890	0	0	0	0.00	0
1900	0	0	0	0.00	0
1910	9928	18.92	6539	12.46	218
1920	756	1.44	166	0.32	5
1930	2884	5.49	1917	3.65	77
1940	278	0.53	194	0.37	10
1950	102	0.19	60	0.11	7
1960	2415	4.6	1262	2.40	63
1970	1799	3.43	1041	1.98	44
1980	773	1.47	187	0.36	23
1990	1026	1.96	525	1.00	53
2000	57	0.11	5	0.01	1
Total	29154	56	16062	30.61	630

Table 3.3. Number of image objects sampled following the stratification strategy for one of the instances that extracted five image objects per stratum (Figure 3.4) summarized by decade; and number of GEDI footprints enclosed within their perimeters. ND: forest stands non-disturbed since 1870.

Disturbance Decade	# Image objects	# GEDI footprints
ND	4	57
1870	0	0
1880	2	31
1890	0	0
1900	0	0
1910	19	247
1920	1	5
1930	4	51
1940	1	3
1950	1	10
1960	8	125
1970	6	56
1980	2	15
1990	2	21
2000	0	0

Table 3.4. Confusion matrix of the TSD estimates of the 674 image objects of known TSD not used to train the RF summarized by decade. ND: forest stands non-disturbed since 1870.

	Reference														
Prediction	ND	1870	1880	1890	1900	1910	1920	1930	1940	1950	1960	1970	1980	1990	2000
ND	**3**	0	1	0	0	0	0	0	0	0	0	1	0	0	0
1870	2	**0**	1	0	0	1	0	0	0	0	0	0	0	0	0
1880	3	0	**4**	0	0	4	0	1	0	0	0	0	0	0	0
1890	0	0	0	**0**	0	0	0	0	0	0	0	0	0	0	0
1900	1	0	0	0	**0**	1	0	0	0	0	0	0	0	0	0
1910	26	7	71	0	0	**165**	0	27	5	0	0	1	0	0	0
1920	0	0	0	0	0	2	**1**	4	0	0	0	0	0	0	0
1930	0	2	0	0	0	7	1	**18**	1	0	3	1	0	0	0
1940	0	0	0	0	0	10	0	3	**1**	1	3	2	0	0	0
1950	0	0	0	0	0	1	0	3	0	**0**	0	1	0	2	0
1960	0	0	0	0	0	3	2	10	2	1	**44**	27	8	5	0
1970	0	0	0	0	0	3	0	2	0	4	5	**5**	6	21	1
1980	0	0	1	0	0	1	0	1	0	0	0	0	**7**	9	0
1990	0	1	0	0	0	1	0	4	0	0	0	0	0	**14**	0
2000	0	0	0	0	0	0	0	0	0	0	0	0	0	0	0

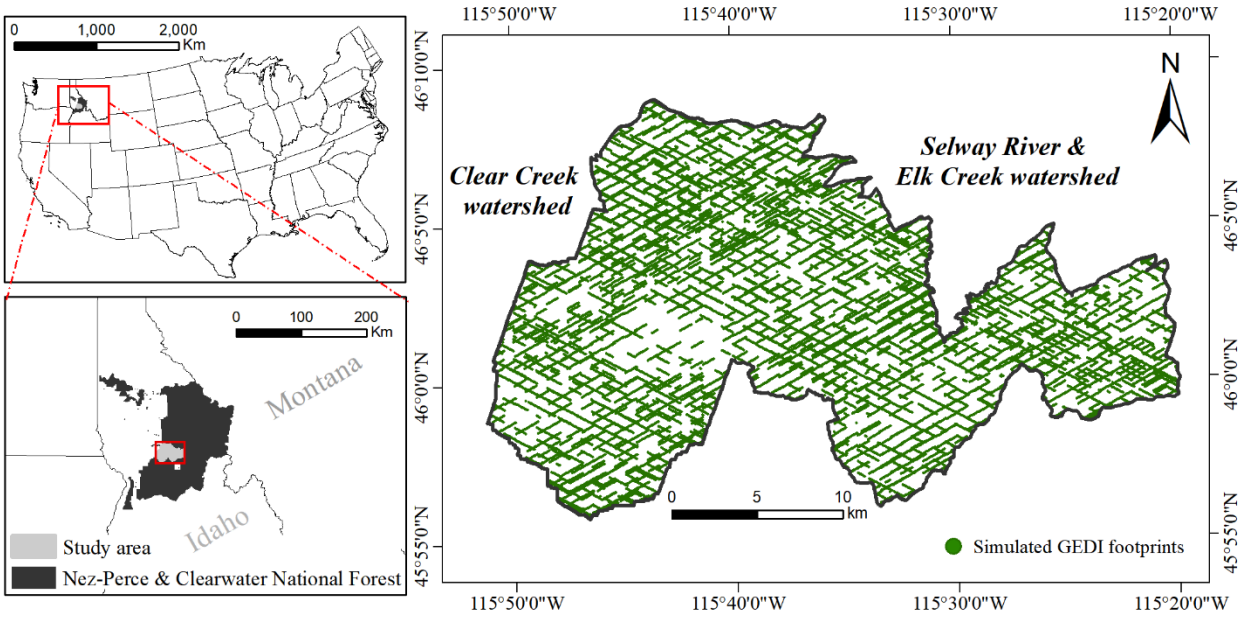

Figure 3.1. Study area in the Nez-Perce & Clearwater National Forest (Idaho-USA), and distribution of the simulated GEDI footprints (not drawn to scale for visualization).

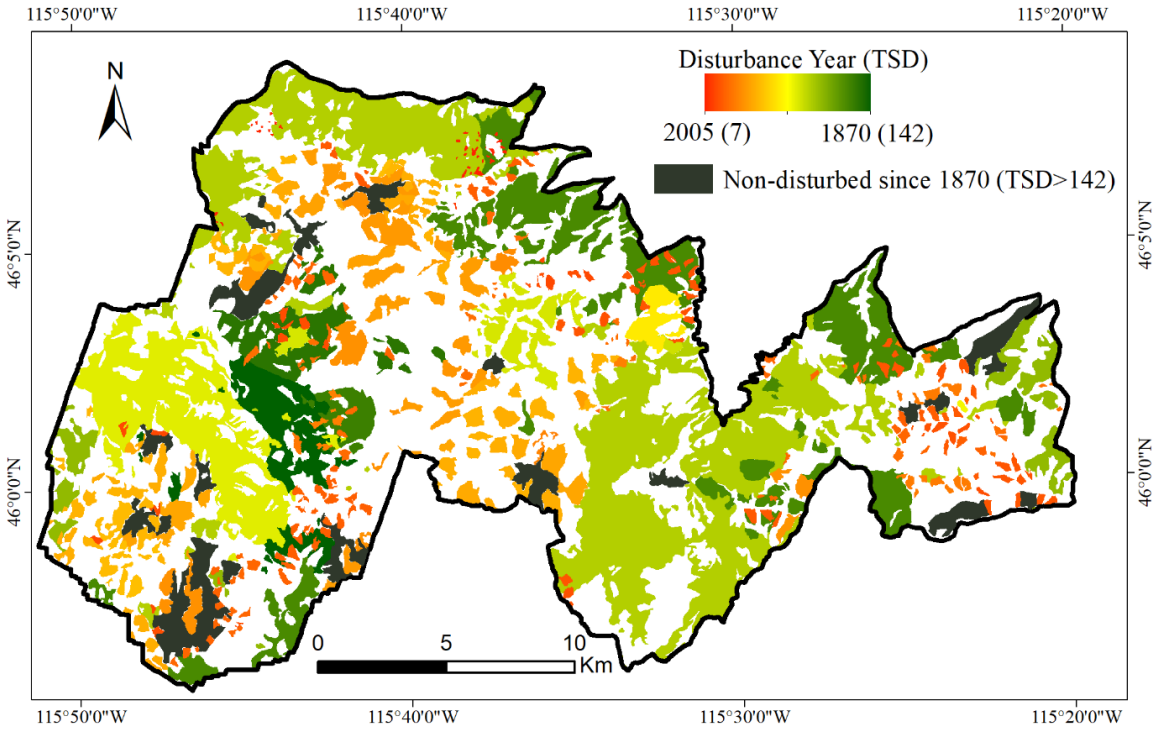

Figure 3.2. Historical stand-replacing disturbances reported in the study area between 1870 and 2005. The dataset was compiled from records of historical burns digitized from aerial photographs (Morgan et al., 2017), and digitized perimeters of clearcut management units reported in the FACTs (Forest Service Activity Track System) harvest dataset (USDA, Forest Service, 2016). Twenty additional forest stands non-disturbed since 1870 were delineated through visual photo-interpretation and added to the dataset.

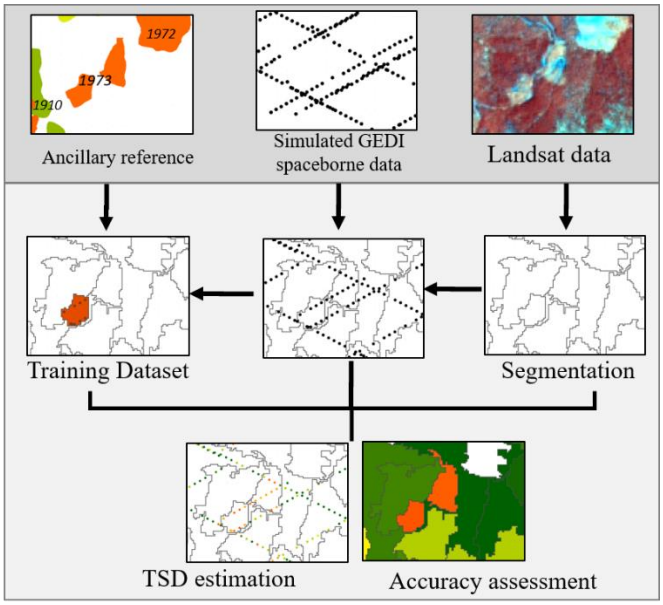

Figure 3.3. Flowchart of the proposed methodology.

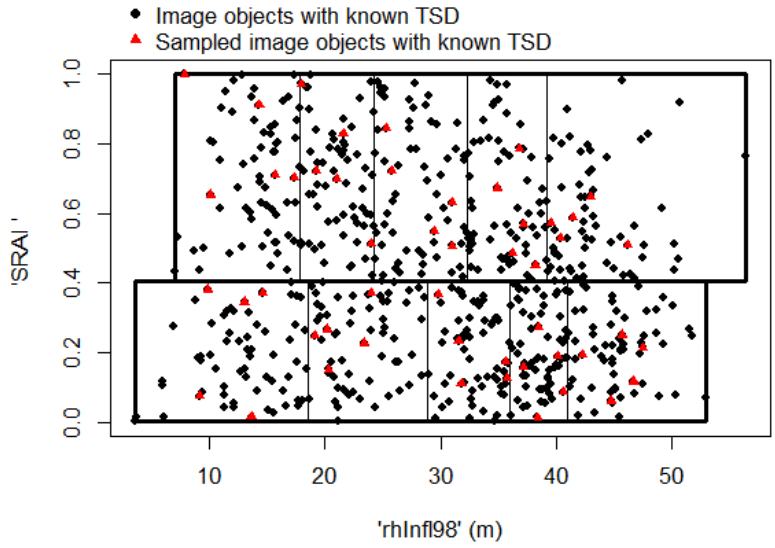

Figure 3.4. Scheme of the stratified random sampling to extract training image objects of known TSD. The mean topographic solar-radiation aspect index ('SRAI') and the mean GEDI 98% relative of height (from inflection points) ('rhInfl98') were used as stratification variables. In this example, 50 image objects (reported as red triangles) are sampled.

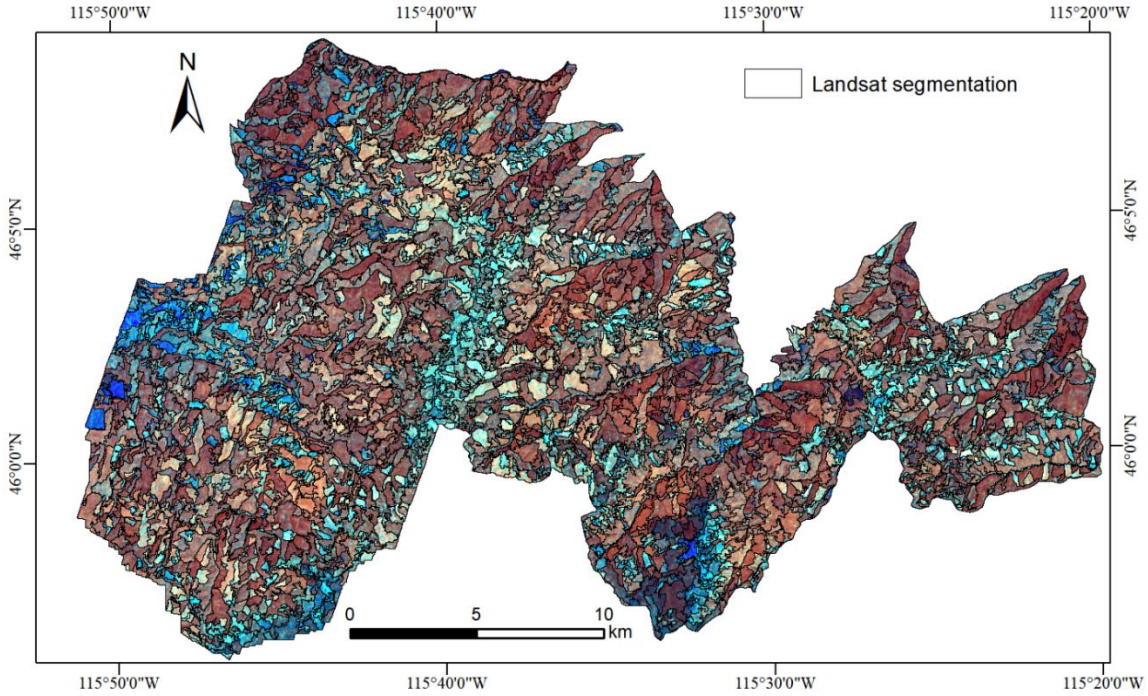

Figure 3.5. Optimal Landsat segmentation (grey vector) of the Tasseled Cap indices of Brightness (TCB), Greenness (TCG) and Wetness (TCW), that are displayed as background in an RGB combination (R= TCW, G= TCG, B= TCB).

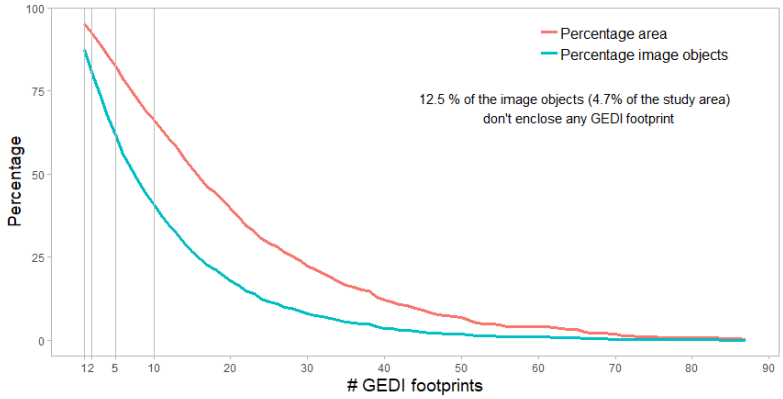

Figure 3.6. Percentage of image objects of the Landsat segmentation (Figure 3.5) that enclosed, at least, the number of GEDI footprints specified on the x axis; and percentage of the study area that they represent.

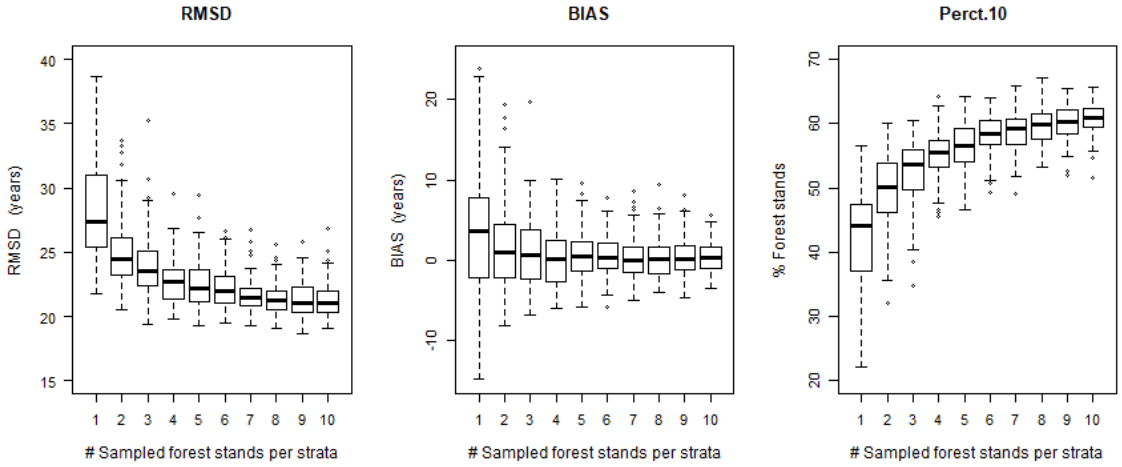

Figure 3.7. Boxplots of RMSD, BIAS, and Perct.10 obtained for TSD predictions when 1 to 10 image objects are selected per stratum (Figure 3.4) to train the RF. The random selection of image objects was replicated 100 times per sample size. Central line represents the median, edges of the box are the first (i.e., the 25th percentile) and the third (i.e., 75th percentile) quartiles, and the whiskers are 1.5 times the range of the upper and lower quartiles.

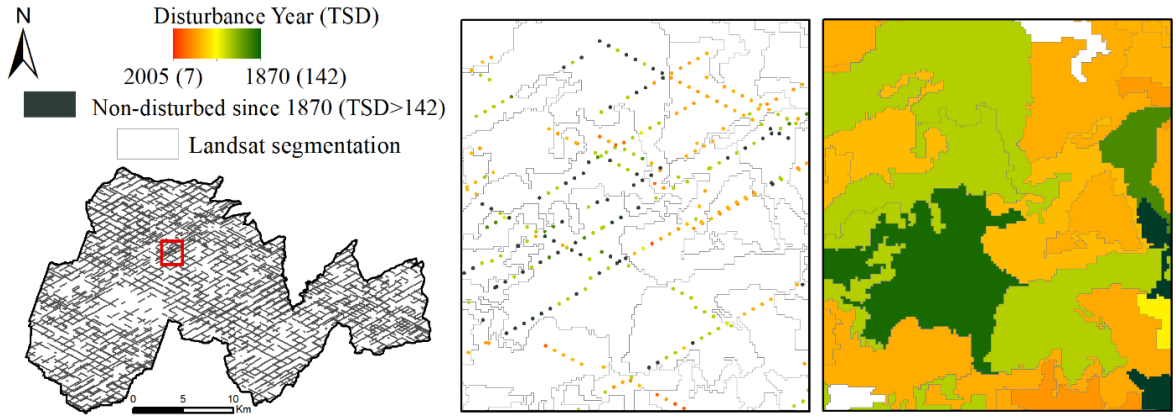

Figure 3.8. Illustrative example of the TSD predictions at the GEDI footprint level (~22 m diameter) and the resulting estimates at the image object level.

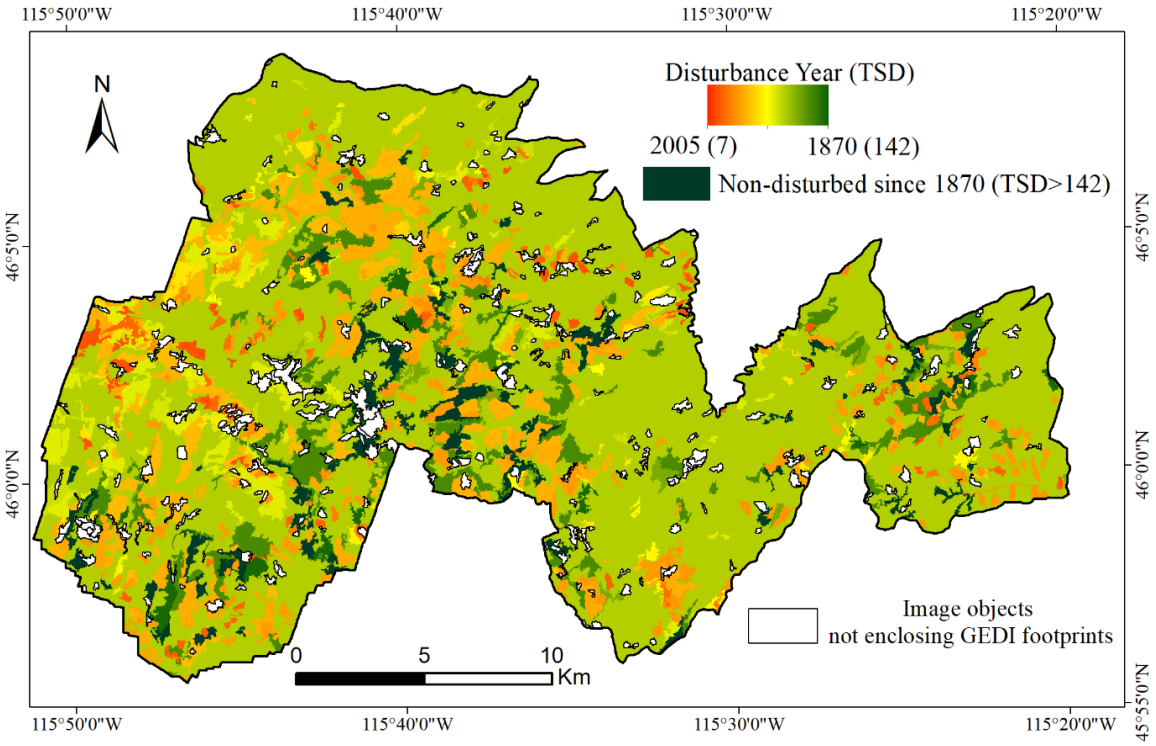

Figure 3.9. TSD predictions at the image object level.

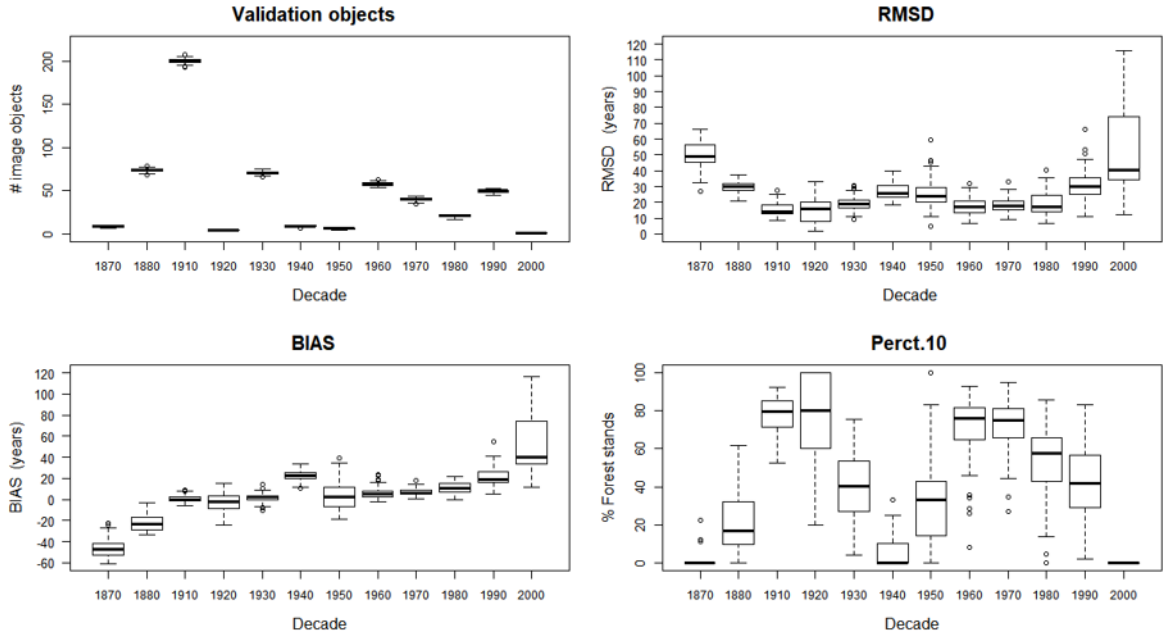

Figure 3.10. Boxplots of the number of validation objects, RMSD, BIAS, and Perct.10 for TSD predictions according to disturbance decade (as observed in the ancillary reference dataset). The boxplots display the results of the 100 imputations obtained by sampling five image objects per stratum to train the RF (Figure 3.4). Central line represents the median, edges of the box are the first (i.e., the 25th percentile) and the third (i.e., 75th percentile) quartiles, and the whiskers are 1.5 times the range of the upper and lower quartiles

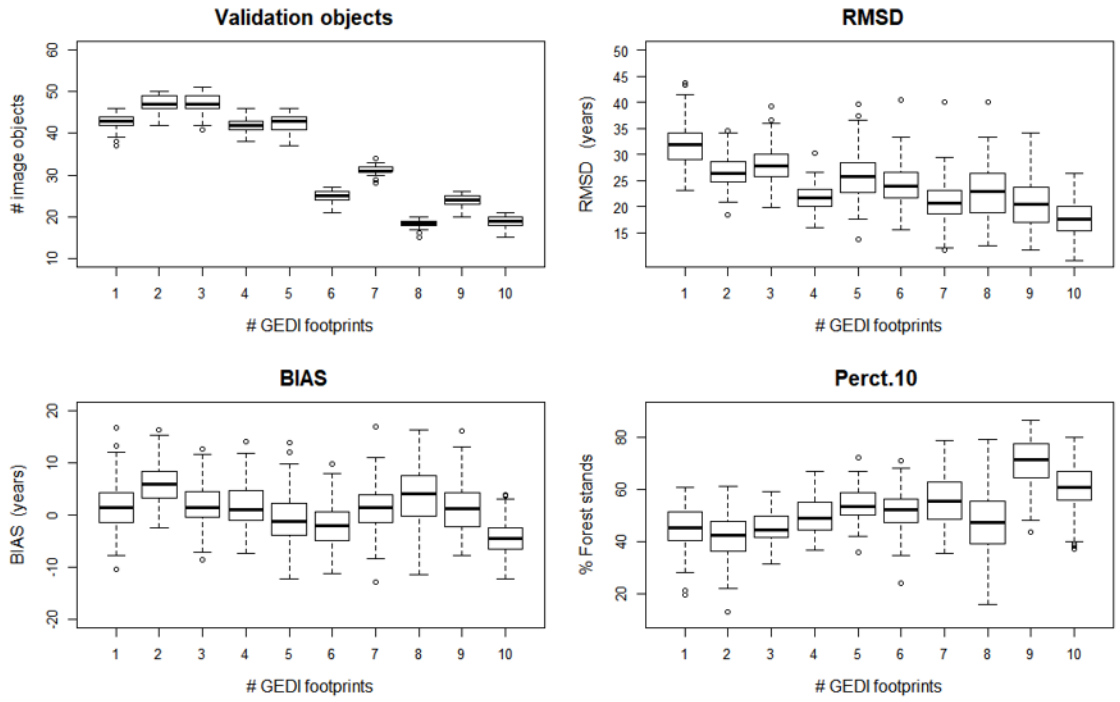

Figure 3.11. Boxplots of number of validation objects, RMSD, BIAS, and Perct.10 obtained for TSD predictions of the validation image objects matching from 1 to 10 GEDI footprints. The boxplots display the results of the 100 imputations obtained by sampling five image objects per stratum to train the RF (Figure 3.4). Central line represents the median, edges of the box are the first (i.e., the 25th percentile) and the third (i.e., 75th percentile) quartiles, and the whiskers are 1.5 times the range of the upper and lower quartiles.

Conclusion

Maps of disturbance history of forests are needed to fully understand global carbon cycle dynamics and assess the role of forests as carbon sink and their climate change mitigation potential, one of the major challenges of our society. This research has demonstrated the feasibility of reconstructing the long term (~100 years) stand-level disturbance history of a forest using LiDAR data and GEOBIA techniques. Our results show that is possible to map historical disturbances that pre-date the beginning of the Earth Observation satellite record, that starts in 1972, and that the accuracy of the resulting disturbance maps is acceptable, at the very least, in estimating the timing of the disturbances (Time Since Disturbance, TSD) in decadal steps. The results thus meet the main overarching goal of the research, i.e. overcoming the spatial and temporal limitations of current, conventionally used disturbance mapping techniques based on time series analysis of optical remotely sensed data. In contrast to these traditional change detection techniques, where time series of imagery acquired close in time to the disturbance event are required to detect abrupt land cover changes, the proposed methodology uses single date, recently acquired LiDAR data as the main input data source. We believe that the methods proposed in this dissertation can complement the established optical data based methodologies, by detecting disturbances that pre-date the systematic availability of moderate resolution Landsat data. It should be noted that while the Landsat data archive is mostly complete in the US since the launch of Landsat-1 in 1972, in many parts of the world it is highly fragmentary until the availability of Landsat-7 in 1999 (Wulder et al., 2016).

The results obtained from airborne (Chapters 1 and 2) and spaceborne simulated data (Chapter 3) demonstrate that both small and large footprint LiDAR-derived data are effective predictors for TSD. The use of LiDAR for TSD estimation leverages the strong relationship between forest structure and forest age, particularly in the early succession stages following a stand-replacing disturbance, before the uneven-aged distribution of the forest canopy is reached.

The importance of adopting the forest stand as a meaningful spatial analysis unit is also one of the main results of this research. We demonstrated that its use introduces contextual information in the LiDAR data analysis that enhances the discrimination of neighboring forest stands, and leads to a more robust estimation of TSD, especially in older, less homogeneous stands. The findings of this research suggest that, in the assessment of forest attributes and ecosystem processes at the stand-level, GEOBIA techniques overcome several of the limitation of pixel-based analysis techniques, commonly adopted in past forest remote sensing studies.

The feasibility study presented in Chapter 3 shows that the recently launched spaceborne LiDAR instruments are suitable for the reconstruction of the disturbance history of forests at regional and global scales. LiDAR missions such as GEDI and ICESAT-2 will provide in the next years global data coverage, potentially transforming the way that forests and their processes are monitored from spaceborne systems (Abdalati et al., 2010; Dubayah et al., 2014). We demonstrated that some of the limitations due to the sampling configuration of these instruments can be overcome through GEOBIA-based data fusion strategies, using contiguously remotely sensed data, such as Landsat or Sentinel-2, as an additional data source.

Drawing from the present study, it is recommended that future research be undertaken to improve the (a) stand delineation through segmentation evaluations designed for specific stand typologies, and (b) TSD classification. For instance, the semi-automatic delineation of the forest stands could be improved developing a multi-scale segmentation approach. This could enhance the delineation of stands regenerating from different forest management activities (e.g., shelterwood, tree seed, etc.), disturbance severities (e.g., low, moderate, high), and disturbance types (e.g., outbreaks, wildfires, harvests). The spatial extent of forest disturbances depends on several factors such as the geographic location, management plans, site conditions, and climate trends. While the technique developed in Chapter 1 is effective in detecting even-aged forest stands, a multi-scale approach could ensure that small disturbed patches—e.g., regenerating from small harvests—or larger but heterogeneous ones—e.g., regenerating from large scale wildfires—are also accurately delineated. The semi-automated delineation and classification of forest stands could be therefore extended from forests whose structure results from stand-replacing disturbances, to forests with more complex stand typologies. The estimation of TSD, on the other hand, could be improved by considering additional predictor variables such as climatic or site index indicators. These variables influence tree growth and stand development, so it is a reasonable expectation that their combination with LiDAR canopy height and density metrics and with topographic variables will increase the accuracy of the TSD classification.

Regarding the GEDI-Landsat data fusion methodology presented in Chapter 3, it is recommended that future research be devoted to the improvement of GEOBIA techniques for the generation of forest stand maps from the segmentation of optical data, such as Landsat or Sentinel-2, potentially exploring their combined use. Furthermore, because of the high sensitivity of the accuracy of the TSD estimation to the number of available GEDI footprints, a natural extension of the present research would be the use of ICESat-2 data as an additional data source. ICESat-2 is also a waveform LiDAR instrument, and while its footprint density is lower than GEDI (Gwenzi et al., 2016; Hancock et al., 2019), their

combined use will provide additional forest structure measurements to be used both for training and for TSD estimation. Finally, future studies should explicitly investigate the influence of image object size, observed TSD and number of footprint observations on the overall accuracy of stand-level TSD estimates.

This thesis demonstrates that GEOBIA techniques on LiDAR data are successful for the specific problem of TSD estimation on forest stands: we believe that future research should investigate the potential of using a similar methodology for estimating additional forest attributes. For example, a similar approach could be used for the explicit assessment of stand-level forest regrowth and successional states. Forest regrowth is one of the major drivers of the forest carbon sink, but large uncertainties are still due to forest demography, mortality, and growth rates which have a large influence on carbon assessment from aboveground biomass (Büntgen et al., 2019; Pugh et al., 2019). The integration of both GEOBIA techniques and LiDAR data could be an asset to improve forest regrowth modelling and to understand the influence of disturbances on stand development and vegetation regeneration, in the same way they that have demonstrated effectiveness to assess TSD. The understanding of past stand regrowth patterns at specific ecosystems is required to model vegetation development and assess the vulnerability of forest ecosystems under different scenarios of climate change and disturbance regimes, which is essential to appraise the role of forests as carbon sinks.

References

Abdalati, W., Zwally, H.J., Bindschadler, R., Csatho, B., Farrell, S.L., Fricker, H.A., Harding, D., Kwok, R., Lefsky, M., Markus, T., Marshak, A., Neumann, T., Palm, S., Schutz, B., Smith, B., Spinhirne, J., Webb, C., 2010. The ICESat-2 Laser Altimetry Mission. Proc. IEEE 98, 735–751. https://doi.org/10.1109/JPROC.2009.2034765

Büntgen, U., Krusic, P.J., Piermattei, A., Coomes, D.A., Esper, J., Myglan, V.S., Kirdyanov, A.V., Camarero, J.J., Crivellaro, A., Körner, C., 2019. Limited capacity of tree growth to mitigate the global greenhouse effect under predicted warming. Nat. Commun. 10, 2171. https://doi.org/10.1038/s41467-019-10174-4

Dubayah, R., Goetz, S.J., Blair, J.B., Fatoyinbo, T.E., Hansen, M., Healey, S.P., Hofton, M.A., Hurtt, G.C., Kellner, J., Luthcke, S.B., Swatantran, A., 2014. The Global Ecosystem Dynamics Investigation. AGU Fall Meet. Abstr. 14.

Gwenzi, D., Lefsky, M.A., Suchdeo, V.P., Harding, D.J., 2016. Prospects of the ICESat-2 laser altimetry mission for savanna ecosystem structural studies based on airborne simulation data.

ISPRS J. Photogramm. Remote Sens. 118, 68–82. https://doi.org/10.1016/j.isprsjprs.2016.04.009

Hancock, S., Armston, J., Hofton, M., Sun, X., Tang, H., Duncanson, L.I., Kellner, J.R., Dubayah, R., 2019. The GEDI simulator: A large-footprint waveform lidar simulator for calibration and validation of spaceborne missions. Earth Space Sci. 0. https://doi.org/10.1029/2018EA000506

Pugh, T.A., Lindeskog, M., Smith, B., Poulter, B., Arneth, A., Haverd, V., Calle, L., 2019. Role of forest regrowth in global carbon sink dynamics. Proc. Natl. Acad. Sci. 116, 4382–4387.

Wulder, M.A., White, J.C., Loveland, T.R., Woodcock, C.E., Belward, A.S., Cohen, W.B., Fosnight, E.A., Shaw, J., Masek, J.G., Roy, D.P., 2016. The global Landsat archive: Status, consolidation, and direction. Remote Sens. Environ., Landsat 8 Science Results 185, 271–283. https://doi.org/10.1016/j.rse.2015.11.032